

# Photoionized Herbig-Haro objects in the Orion Nebula I: HH 529 II and III

J. E. Méndez-Delgado<sup>1,2</sup> , C. Esteban<sup>1,2</sup>, J. García-Rojas<sup>1,2</sup>, W. J. Henney<sup>3</sup>  
and K. Z. Arellano-Córdova<sup>1</sup> and collaborators

<sup>1</sup> Instituto de Astrofísica de Canarias (IAC), E-38205 La Laguna, Spain

<sup>2</sup> Departamento de Astrofísica, Universidad de La Laguna, E-38206 La Laguna, Spain

<sup>3</sup> Instituto de Radioastronomía y Astrofísica, Universidad Nacional Autónoma de México, Apartado Postal 3-72, 58090 Morelia, Michoacán, México

Accepted XXX. Received YYY; in original form ZZZ

## ABSTRACT

This is the abstract.

**Key words:** ISM:Abundances – ISM: Herbig–Haro objects – ISM: individual: Orion Nebula – ISM: individual: HH 529III.

## 1 INTRODUCTION

This is an introduction.

## 2 OBSERVATIONS AND DATA REDUCTION

The observations were made during the November 28 and 29, 2013 nights using the Ultraviolet Visual Echelle Spectrograph (UVES) (D’Odorico et al. 2000) in the UT2 (Kueyen) of the Very Large Telescope (VLT) in Cerro Paranal, Chile. The slit position was centred at the coordinates RA(J2000)=05<sup>h</sup>35<sup>m</sup>16<sup>s</sup>.80, DEC(J2000)=−05°24′00″, having a length of 10 arcsec in the blue arm and 12 arcsec in the red arm looking for an adequate interorder separation. Table 1 shows the observational features of the night. The slit width was set to 1 arcsec, which is equivalent to an effective spectral resolution  $\lambda/\Delta\lambda \approx 40000$  (6.5 km s<sup>−1</sup>). To perform the flux calibration of the data, three exposures of 150s of the standard star GD71 (Moehler et al. 2014a,b) were taken under similar conditions of seeing and airmass than the science observations during the same night. The spatial coverage of the slit is shown in Fig. 1.

Our observations cover the spectral range between 3100–10420 Å, using standard features for two dichroic settings in UVES. Dichroic#1 setting split the light in two wavelengths ranges: from 3100 to 3885 Å in the blue arm and from 4785 to 6805 Å in the red one, while the dichroic#2 setting covers from 3750 to 4995 Å in the blue arm and from 6700 to 10420 Å in the red one. However, in our high resolution and wide spectral range observations, there are some observational gaps. The red arm use two CCDs, and due to their physical separation, spectral ranges 5773–5833 Å and 8540–8650 Å could not be observed. Additionally there are some narrow gaps that could not be observed in the redmost part of the red arm in the dichroic#2 setting because the spectral orders could not

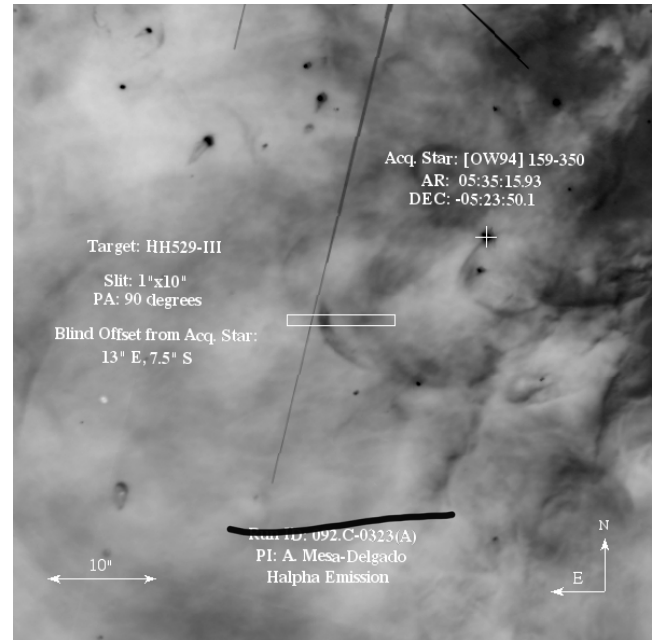


**Figure 1.** H $\alpha$  Hubble Space Telescope (HST) image of the central part of the Orion Nebula just to the south of  $\theta^1$ Ori C. Our slit position is indicated.

fit entirely within the CCD. These range are ~8911–8913 Å, 9042–9046 Å, 9178–9182 Å, 9317–9323 Å, 9460–9469 Å, 9608–9619 Å, 9760–9774 Å, 9918–9935 Å, 10080–10100 Å and 10248–10271 Å.

We reduced the spectra using a combination of tasks from the public ESO UVES pipeline (Ballester et al. 2000) under the GASGANO graphic user interface, and tasks built by ourselves based

\* E-mail: jemd@iac.es

**Table 1.** Observational features.

Date	$\Delta\lambda$ (Å)	Exp. time (s)	Seeing (arcsec)	Airmass
2013-11-29	3100-3885	5, 3×180	0.79	1.20
2013-11-29	3750-4995	5, 3×600	0.65	1.14
2013-11-29	4785-6805	5, 3×180	0.79	1.20
2013-11-29	6700-10420	5, 3×600	0.65	1.14

on IRAF<sup>1</sup> (Tody 1993) and several python packages. Firstly, we used IRAF tasks FIXPIX and IMCOMBINE to mask known bad pixels in our images and to combine all the images with the same exposure time. Then, we used the ESO UVES pipeline for bias subtraction, background subtraction, aperture extraction, flat-fielding and wavelength calibration. As a product, we obtained a 2D spectrum of science for each arm in each dichroic setting without flux calibration. We followed the same procedure for GD 71 but extracting both a 2D and a 1D spectrum. The 2D spectrum of the calibration star helps us to perceive the presence of faint sky lines which are also present in the science spectra.

One crucial step of the data reduction is to perform adequate cuts in the spatial direction on the slit to extract 1D spectra. We chose these spatial cuts in order to study in detail each observed velocity component and trying to maximise the shock/nebular emission ratio. We relied on the [Fe III]  $\lambda 4658$  line, which is relatively bright in the shock components to delimit the cuts. Our seeing conditions permit to separate the two high-velocity components that can be distinguish in our spectra (see Figure 2). One of them have a "ball shape" while the other presents an elongated distribution along the spectral axis. This is related with the morphology of the outflow system of HH529 (firstly identified by Bally et al. 2000). It shows three notorious bright arcs, identified by the numbers I, II and III, being numbered by their position from west to east (O'Dell & Henney 2008). The length in the spatial direction covered by each cut is 1.23 arcsec, 4.43 arcsec, 2.46 arcsec and 1.23 arcsec for cuts 1, 2, 3 and 4, respectively. This numbering has been defined from west to east in the spatial position (see Fig. 1). Cut 1 is at the bottom and cut 4 at the top of Fig. 2. In the context of the nomenclature given by O'Dell & Henney (2008), the high-velocity component of the cut 3 corresponds to HH529III, while that of cut 2 should be related to HH529II. We have also defined an additional 1D spectrum, labelled as "combined cuts". This was created by adding the flux of the lines measured in all the components of all cuts. The lines included in this spectrum were those detected and identified in the nebular component of all cuts. The spectrum of the combined cuts is useful to analyze the effect that a non-resolved shock component would have in the properties of a low-resolution spectrum. We used the Python-based Astropy package (Astropy Collaboration et al. 2013; Price-Whelan et al. 2018) to obtain 1D spectra for each cut, doing the conversion between the different pixel scale of the CCDs in the blue and the red arm. Each spatial cut covers an area larger than the seeing size during the observations, as it is shown in Table 1. We used the IRAF tasks STANDARD, SENSFUNC and CALIBRATE to perform the flux calibration of each 1D spectra of all cuts. The radial velocity correction was made using Astropy.

<sup>1</sup> IRAF is distributed by National Optical Astronomy Observatory, which is operated by Association of Universities for Research in Astronomy, under cooperative agreement with the National Science Foundation

**Table 2.** Reddening coefficients for each component of each cut.

	c(H $\beta$ )	
	Shock	Nebula
Cut 1	-	$0.82 \pm 0.02$
Cut 2	$0.90 \pm 0.03$	$0.83 \pm 0.02$
Cut 3	$0.89 \pm 0.05$	$0.84 \pm 0.03$
Cut 4	-	$0.83 \pm 0.02$
Combined cuts	-	$0.85 \pm 0.02$

### 3 LINE INTENSITIES AND REDDENING

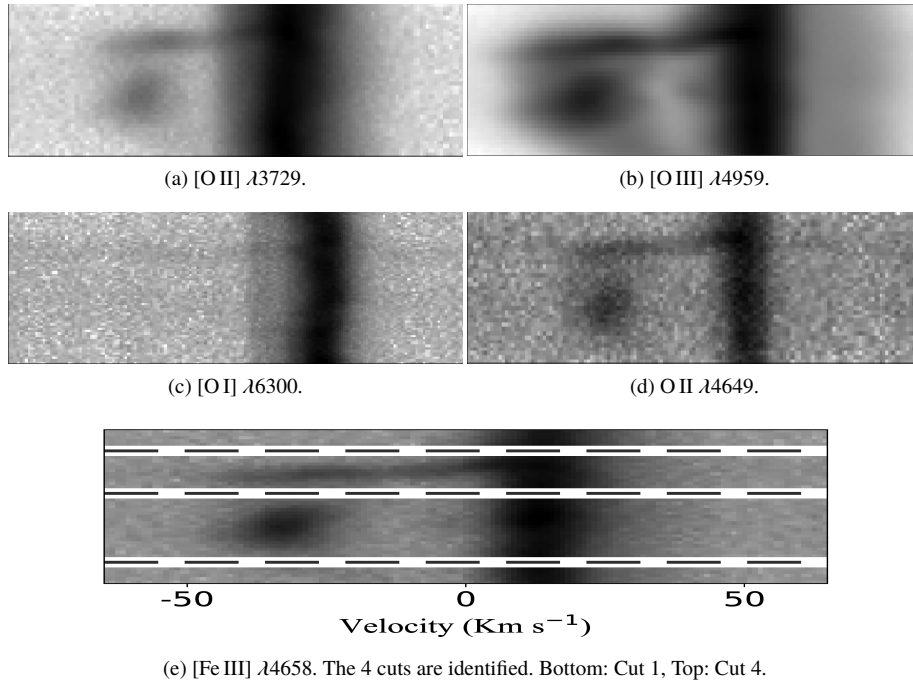
We used the SPLOT task from IRAF to measure line intensities and estimate their uncertainties. We applied a double Gaussian profile fit for the nebular and shock component, delimiting the continuum by eye. For each measured line, we estimate the value of the continuum and its *rms* on each side to propagate uncertainties associated to the flux measurement. In case of evident line blending, we applied as many Gaussians as necessary to properly reproduce the line profile. As it was mentioned in § 2, the observed wavelength range (3100-10420 Å) was covered in 4 sections (two dichroic settings splitting the light into two spectrograph arms). Between each section, there is an overlapping zone from where we used the most intense lines to normalize the entire spectrum with respect to H $\beta$ . The measured flux of H I  $\lambda 3835$ , [O III]  $\lambda 4959$  and [S II]  $\lambda 6731$  lines were used to normalize the spectra from the blue arm of dichroic#1, the red arm of dichroic#1 and the red arm of dichroic#2 settings respectively (H $\beta$  is in the blue arm of dichroic#2 setting). This normalization eliminates the differences in flux between each part of the spectrum due to the different pixel scale between the blue and the red arms.

The emission lines were corrected for reddening using Eq. (1), where  $f(\lambda)$  is the adopted extinction curve from Blagrade et al. (2007), normalized to H $\beta$ . We calculate the reddening coefficient, c(H $\beta$ ), by using the ratios of H $\epsilon$ , H $\delta$ , H $\gamma$  and H $\alpha$  Balmer lines and the P12, P11, P10, P9 Paschen lines with respect to H $\beta$  and the emissivity coefficients of Storey & Hummer (1995). The final adopted c(H $\beta$ ) value is the weighted average value obtained from the aforementioned Balmer and Paschen lines and is shown in Table 2 for both the shock and nebular components. The selected HI lines are free of line-blending or telluric absorptions that may affect the determination of c(H $\beta$ ). Despite there are more isolated and bright Balmer and Paschen lines available in the spectra, we did not use them since their emission depart from the case B values. This behaviour was reported previously in the Orion Nebula (Mesa-Delgado et al. 2009), the Magellanic Clouds (Domínguez-Guzmán et al. 2019) and in several Planetary Nebulae (PNe Rodríguez 2020).

$$\frac{I(\lambda)}{I(H\beta)} = \frac{F(\lambda)}{F(H\beta)} \times 10^{c(H\beta)f(\lambda)}. \quad (1)$$

Blagrade et al. (2006) observed the zone of the Orion Nebula that includes HH529III using the 4m Blanco telescope at the Cerro Tololo Inter-American Observatory, covering a more limited spectral region (3500-7500 Å). A comparison between the reddening corrected intensity of lines between their nebular component and the nebular component of cut 2 from this work is shown in Fig. 3. From Blagrade et al. (2006) spectra, we have excluded lines with notes of "Avg, blend or small FWHM" for our comparison, due to their usual inconsistent fluxes. For example, [Ne III]  $\lambda 3967.46$  line, marked with an "Avg", is inconsistent with the measured intensity of [Ne III]  $\lambda 3868.75$ , since their observed ratio is 2.02, quite far from the theoretical one of 3.29. A least squares linear fit yields the rela-

**Figure 2.** Sample of emission lines in the 2D spectrum. All images are centred at  $\lambda_0$ . The different cuts are shown in the bottom image.



tionship  $y = 1.00 (\pm 0.01) x + 0.05 (\pm 0.02)$ , indicating that the spectrum of Blaggrave et al. (2006), shows systematically slightly larger intensity line ratios than ours. This is quite noticeable in the spectral region of the high-level Balmer lines (3660–3720 Å), where this difference can reach up to 50%. This large difference may be due to the relative weakness of these lines, coupled with the abrupt change in the continuum due to the closeness of the Balmer discontinuity. For other lines, the slight discrepant tendency disappears considering an increase of about 10% in the intensity of  $I(H\beta)$ . This possible underestimation of  $I(H\beta)$  in the Blaggrave et al. (2006) spectrum for the nebular component is the most likely explanation considering that the intensity ratios between other bright H I lines are consistent with the theoretical ones and not those with respect to  $H\beta$ . We did not compare their shock component with ours, because the seeing of 2–2.5 arcsec of the observations of Blaggrave et al. (2006) are worse than ours and they probably observed a combination of our shock components of cuts 2 and 3.

Fig. 4 shows  $H\beta$  in the different components of the different cuts. As it can be seen, the reddest component (corresponding to the nebular component) has practically the same profile in all cuts except in cut 3, where there is some contamination of gas at somewhat blueshifted velocity contributing to broaden  $H\beta$ . This is quite evident from Fig. 2, where the shock component of cut 3 is clearly seen as an elongated arm.

Line identifications were consistently made by adopting the theoretical wavelengths of Peter Van Hoof's latest Atomic Line List v2.05b21<sup>2</sup> (Van Hoof 2018) for all ions except for Cl III, Cl IV and Ne III due to some inconsistencies found (see §9 for a detailed discussion). All the wavelengths in this list are obtained from the theoretical difference of energy of the levels involved in the emission, with the exception of hydrogenic lines, where all the fine structure components are averaged. Our spectra are very extensive

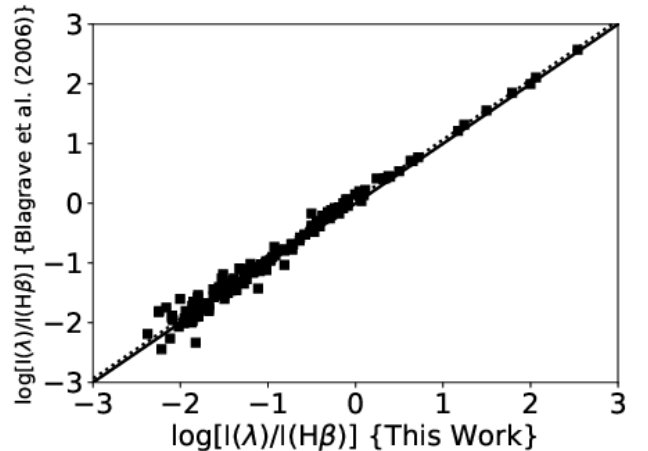


**Figure 3.** Comparison between the intensity of the lines corrected of reddening in the nebular component of cut 2 and the nebular component of Blaggrave et al. (2006). The dotted line represents the linear fit  $y = 1.00x + 0.05$ , while the solid line represents  $y = x$ .

and are attached in the online annexes to this article. In the nebular components, 514, 633, 579 and 522 lines were measured for cuts 1, 2, 3 and 4, respectively. For HH529II, 376 lines were detected, while for HH529III they were 245. In the case of a multi-line blend, this was counted as one detection.

## 4 PHYSICAL CONDITIONS

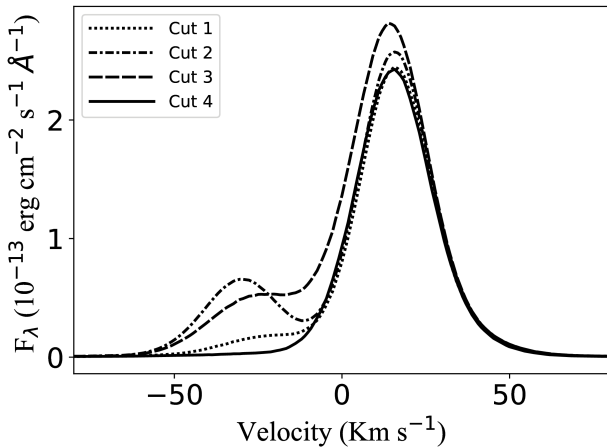
### 4.1 Physical conditions based on Collisionally Excited Lines

We use PyNeb (version 1.1.10) (Luridiana et al. 2015) and the updated atomic dataset listed in Table 3 to calculate physical conditions

<sup>2</sup> <http://www.pa.uky.edu/peter/newpage/>

**Table 3.** Atomic data set used for collisionally excited lines.

Ion	Transition Probabilities	Collision Strengths
O <sup>+</sup>	Froese Fischer & Tachiev (2004)	Kisielius et al. (2009)
O <sup>2+</sup>	Wiese et al. (1996), Storey & Zeippen (2000)	Storey et al. (2014)
N <sup>+</sup>	Froese Fischer & Tachiev (2004)	Tayal (2011)
Ne <sup>2+</sup>	McLaughlin et al. (2011)	McLaughlin et al. (2011)
S <sup>+</sup>	Podobedova et al. (2009)	Tayal & Zatsarinsky (2010)
S <sup>2+</sup>	Podobedova et al. (2009)	Grieve et al. (2014)
Cl <sup>+</sup>	Mendoza & Zeippen (1983)	Tayal (2004)
Cl <sup>2+</sup>	Fritzsche et al. (1999)	Butler & Zeippen (1989)
Cl <sup>3+</sup>	Kaufman & Sugar (1986), Mendoza & Zeippen (1982b), Ellis & Martinson (1984)	Galavis et al. (1995)
Ar <sup>2+</sup>	Mendoza (1983), Kaufman & Sugar (1986)	Galavis, Mendoza & Zeippen (1995)
Ar <sup>3+</sup>	Mendoza & Zeippen (1982a)	Ramsbottom & Bell (1997)
Fe <sup>2+</sup>	Quinet (1996), Johansson et al. (2000)	Zhang, Hong Lin (1996)
Fe <sup>3+</sup>	Froese Fischer et al. (2008)	Zhang & Pradhan (1997)
Ni <sup>2+</sup>	Bautista (2001)	Bautista (2001)

**Figure 4.** Line profile of H $\beta$  in the spectra of the different extracted cuts.**Table 4.** Effective recombination coefficients used for recombination lines.

Ion	Reference
H <sup>+</sup>	Storey & Hummer (1995)
He <sup>+</sup>	Porter et al. (2012, 2013)
O <sup>+</sup>	Pequignot et al. (1991)
O <sup>2+</sup>	Storey et al. (2017)
C <sup>2+</sup>	Davey et al. (2000)
Ne <sup>2+</sup>	Kisielius et al. (1998)

based on the intensity ratios of collisionally excited lines (CELs) from different ions.

The first step was to test all the intensity ratios of CELs that can serve as a temperature or density diagnostic using the PyNeb's task `getCrossTemDen`. This task uses two line ratios at the same time: one as density diagnostic and the other one for temperature, giving their convergence to a pair  $n_e, T_e$  as a result. We tried all possible permutations for all the available diagnostics in all components from all cuts. We only discarded the use of lines strongly affected by blends, telluric emissions and/or absorptions or reflections in

the optical system of the spectrograph. We did not consider the  $n_e$  diagnostic based on the [N I]  $\lambda\lambda 5198/5200$  doublet owing to their unphysical meaning in the Orion Nebula (Ferland et al. 2012).

Diagnostics based on [Ni III]  $\lambda_1/\lambda_2$ , where  $\lambda_1, \lambda_2 \in [6000, 6534, 6682, 6797, 6946, 7890]$  and  $\lambda_1 \neq \lambda_2$  do not give any useful physical information since they either did not converge or showed convergences at values highly discordant with the other diagnostics. This will be commented in greater detail in § 5.1.2. Another interesting case is on the diagnostics based on [Fe III]  $\lambda_1/\lambda_2$ , where  $\lambda_1, \lambda_2 \in [4658, 4702, 4734, 4881, 5011, 4925, 4987, 5271]$  and  $\lambda_1 \neq \lambda_2$ . With the exception of [Fe III] 4658/4702, all the diagnostics converge in a fairly wide range of physical conditions. This is due to the ambivalence and/or high dependence of these ratios on both density and temperature. This will be discussed in § 4.2.

After the initial scan, we define the ratios we consider are good indicators of electron density and temperature. Then we use Monte Carlo simulations with 1000 points to estimate uncertainties in the physical conditions given by the PyNeb's `getCrossTemDen` task. For example, with [O III] $\lambda 4363/\lambda 4959+5007$  as a temperature indicator and [Cl III] $\lambda 5538/\lambda 5518$ , [Fe III] $\lambda 4658/\lambda 4702$ , [O II] $\lambda 3726/\lambda 3729$ , [S II] $\lambda 6731/\lambda 6716$ , [Ar IV] $\lambda 4740/\lambda 4711$  as density diagnostics, we estimate the convergence in  $T_e$  and  $n_e$  and their uncertainties in every case. The central value of  $T_e$  or  $n_e$  corresponds to the median of the Monte Carlo distribution and the errors are represented by the deviations to 84th and 16th percentiles. After this procedure, all diagnostics (either  $T_e$  or  $n_e$ ), will have a result for each cross-comparison. Then, for all components on each cut, we define the representative  $n_e$  as the weighted mean<sup>3</sup> in each cross-comparison with all the the temperature indicators. Finally, using the adopted representative  $n_e$ , we calculate  $T_e$  with the available diagnostics using the PyNeb's `getTemDen` task. Within the scheme of two ionization zones, we define  $T_{e(\text{high})}$  as the weighted mean  $T_e$  obtained from [Ar III] $\lambda 5192/\lambda 7136+7751$ , [O III] $\lambda 4363/\lambda 4959+5007$  and [S III] $\lambda 6312/\lambda 9069+9531$  line ratios. Similarly, we define  $T_{e(\text{low})}$  based on the resulting  $T_e$  ob-

<sup>3</sup> The weights were defined as the inverse of the square of the error associated to each density diagnostic.

**Table 5.** Physical conditions determined from several diagnostics.

Diagnostic	Cut 1 Nebula	Cut 2 Shock	Cut 2 Nebula	Cut 3 Shock	Cut 3 Low Velocity Shock+Nebula	Cut 4 Nebula	Combined Cuts
$n_e$ (cm $^{-3}$ )							
[O II] $\lambda\lambda 3726/\lambda 3729$	5460 $^{+1000}_{-750}$	10570 $^{+3680}_{-2420}$	5220 $^{+960}_{-720}$	18020 $^{+17170}_{-6930}$	5530 $^{+1000}_{-800}$	5070 $^{+880}_{-710}$	5530 $^{+990}_{-810}$
[S II] $\lambda\lambda 6731/\lambda 6716$	4230 $^{+1000}_{-980}$	9390 $^{+1000}_{-3950}$	4160 $^{+1570}_{-1610}$	13130 $^{+15820}_{-6570}$	4130 $^{+2020}_{-1790}$	4160 $^{+960}_{-960}$	4510 $^{+2270}_{-1170}$
[Cl III] $\lambda\lambda 5538/\lambda 5518$	7020 $^{+960}_{-900}$	8170 $^{+1810}_{-1810}$	6670 $^{+920}_{-860}$	15040 $^{+4490}_{-4490}$	7370 $^{+1120}_{-1120}$	7000 $^{+900}_{-900}$	7420 $^{+1100}_{-1100}$
[Fe III] $\lambda\lambda 4658/\lambda 4702$	9260 $^{+3700}_{-2890}$	12390 $^{+5010}_{-3460}$	8990 $^{+2840}_{-2350}$	33800 $^{+33820}_{-10530}$	10490 $^{+4240}_{-3090}$	8340 $^{+3620}_{-2530}$	9510 $^{+3790}_{-2750}$
[Ar IV] $\lambda\lambda 4740/\lambda 4711$	4480 $^{+1700}_{-1640}$	6410 $^{+1900}_{-1880}$	5920 $^{+980}_{-940}$	15050 $^{+13300}_{-9240}$	6400 $^{+1690}_{-1660}$	5460 $^{+1000}_{-1050}$	6580 $^{+2000}_{-1870}$
O II*	4710 $\pm$ 710	3490 $\pm$ 340	4390 $\pm$ 400	3600 $\pm$ 850	4920 $\pm$ 550	4350 $\pm$ 610	5420 $\pm$ 690
[Fe III]*	8530 $\pm$ 1050	11880 $\pm$ 1860	9430 $\pm$ 1010	44090 $\pm$ 7580	8530 $\pm$ 1160	9020 $\pm$ 1170	10360 $\pm$ 1410
<b>Adopted</b>	<b>5830 <math>\pm</math> 1210</b>	<b>7980 <math>\pm</math> 1680</b>	<b>5870 <math>\pm</math> 970</b>	<b>15810 <math>\pm</math> 1950</b>	<b>6180 <math>\pm</math> 1220</b>	<b>5650 <math>\pm</math> 1030</b>	<b>6290 <math>\pm</math> 1130</b>
$T_e$ (K)							
T(H I) Balmer	-	-	-	-	-	-	7520 $\pm$ 790
T(H I) Paschen	-	-	-	-	-	-	< 16290
T(He I)	8280 $^{+520}_{-570}$	7310 $^{+600}_{-610}$	8060 $^{+540}_{-510}$	7740 $^{+420}_{-480}$	8090 $\pm$ 530	7390 $^{+470}_{-580}$	7690 $^{+500}_{-510}$
[N II] $\lambda\lambda 5755/\lambda 6584$	9910 $\pm$ 250	10560 $\pm$ 560	9850 $\pm$ 240	12210 $^{+820}_{-810}$	10060 $^{+260}_{-280}$	9860 $^{+250}_{-270}$	9990 $^{+250}_{-270}$
[O II] $\lambda\lambda 3726+29/\lambda\lambda 7319+20+30+31$	10340 $^{+1330}_{-940}$	-	-	-	-	11230 $^{+1330}_{-1330}$	10910 $^{+1320}_{-1320}$
[S II] $\lambda\lambda 4069+76/\lambda\lambda 6716+31$	11430 $^{+3290}_{-1870}$	-	11070 $^{+2420}_{-1450}$	-	10550 $^{+2450}_{-1570}$	10790 $^{+1440}_{-1470}$	11000 $^{+2510}_{-1600}$
[O III] $\lambda\lambda 4363/\lambda\lambda 4959+5007$	8430 $\pm$ 90	8270 $^{+80}_{-70}$	8410 $^{+80}_{-90}$	8740 $\pm$ 100	8510 $\pm$ 90	8320 $\pm$ 90	8450 $^{+80}_{-90}$
[S III] $\lambda\lambda 6312/\lambda\lambda 49069+9531$	9220 $^{+290}_{-330}$	8670 $\pm$ 310	8990 $^{+290}_{-330}$	9260 $^{+430}_{-410}$	8920 $^{+330}_{-300}$	8850 $^{+290}_{-320}$	8970 $^{+280}_{-290}$
[Ar III] $\lambda\lambda 5192/\lambda\lambda 7136+7751$	8280 $^{+280}_{-310}$	8690 $^{+480}_{-550}$	8390 $^{+280}_{-280}$	-	8250 $^{+260}_{-290}$	8280 $^{+380}_{-420}$	8270 $^{+280}_{-320}$
O II*	-	-	9350 $\pm$ 1090	-	-	-	-
[Fe III]*	7800 $\pm$ 800	8500 $\pm$ 1050	8450 $\pm$ 730	8440 $\pm$ 2260	7600 $\pm$ 710	7350 $\pm$ 590	8440 $\pm$ 710
<b><math>T_e</math> (low) Adopted</b>	<b>9930 <math>\pm</math> 140</b>	<b>10560 <math>\pm</math> 560</b>	<b>9860 <math>\pm</math> 240</b>	<b>12210 <math>\pm</math> 820</b>	<b>10070 <math>\pm</math> 270</b>	<b>9920 <math>\pm</math> 280</b>	<b>10040 <math>\pm</math> 210</b>
<b><math>T_e</math> (high) Adopted</b>	<b>8470 <math>\pm</math> 200</b>	<b>8300 <math>\pm</math> 110</b>	<b>8440 <math>\pm</math> 140</b>	<b>8770 <math>\pm</math> 110</b>	<b>8510 <math>\pm</math> 120</b>	<b>8360 <math>\pm</math> 140</b>	<b>8480 <math>\pm</math> 150</b>

\* indicates that a maximum likelihood method was used.

tained from [S II]  $\lambda\lambda 4069+76/\lambda\lambda 6716+31$ , [N II]  $\lambda\lambda 5755/\lambda 6584$  and [O II]  $\lambda\lambda 3726+29/\lambda\lambda 7319+20+30+31$  line ratios.

It is remarkable that in the nebular component of all cuts the observed [S III]  $\lambda\lambda 9531/\lambda 9069$  line intensity ratio does not agree with the theoretical value. This is owing to strong telluric absorptions that affect the [S III]  $\lambda 9069$  line. These telluric absorptions do not affect the blueshifted lines of the high velocity components. After an inspection in the 2D spectra of the calibration star and in the science object, we concluded that [S III]  $\lambda 9531$  is not affected by telluric absorptions or emissions at the heliocentric motion at which the observations were taken. In the nebular component of all cuts, we used the theoretical ratio  $I([S \text{ III}] 9531)/I([S \text{ III}] 9069) = 2.47$  obtained from the atomic data given in Table 3 to estimate  $T(\text{[S III]})$ .

Plasma diagnostic plots shown in Fig. A1, indicate that the resulting values of each diagnostic are consistent with each other. The numerical values in each case are presented in Table 5.

## 4.2 Physical conditions based on [Fe III] lines.

As it was mentioned in § 4, density diagnostics based on different line intensity ratios of [Fe III] apparently give discordant results. This is mainly due to the ambivalence in the density dependence of some observed intensity ratios and/or due to high dependence on  $T_e$  as well as on  $n_e$ . These two scenarios are exemplified in Fig. 5 for [Fe III]  $\lambda\lambda 4881/\lambda 4658$  and  $\lambda\lambda 5271/\lambda 4658$  line ratios. For the expected densities in the different components observed in this work ( $n_e$  between  $\sim 10^3$  cm $^{-3}$  and  $\sim 10^5$  cm $^{-3}$ ), these diagnostics are not very enlightening on their own. On the other hand, [Fe III]  $\lambda 4658/\lambda 4702$  is the most reliable diagnostic in our case. However, although there is no ambivalence at the expected densities, the predicted value for the [Fe III]  $\lambda 4658/\lambda 4702$  intensity ratio varies little in a relatively wide range of densities. As a consequence, the deduced density from [Fe III]  $\lambda 4658/\lambda 4702$  inherently will have large uncertainties, even with relatively low errors in the line fluxes.

We consider that the best way to determine the physical condi-

tions based on the observed intensity ratios of [Fe III] lines is with a maximum-likelihood process. This method is based on a  $\chi^2$  minimization by testing a wide range of parameters.  $\chi^2$  is defined in Eq. (2), as the sum of the quadratic differences between the abundance of ion  $X^i$  (in this case Fe $^{2+}$ ) determined with each emission line included in the procedure and the weighted average defined in Eq. (3).

$$\chi^2 = \sum_{\lambda} \frac{\left( n \left( \frac{X^i}{H^+} \right)_{\lambda} - \overline{n \left( \frac{X^i}{H^+} \right)} \right)^2}{\Delta n \left( \frac{X^i}{H^+} \right)_{\lambda}}, \quad (2)$$

$$\overline{n \left( \frac{X^i}{H^+} \right)} = \frac{\sum_{\lambda} \left( n \left( \frac{X^i}{H^+} \right)_{\lambda} / \Delta n \left( \frac{X^i}{H^+} \right)_{\lambda} \right)^2}{\sum_{\lambda} \left( 1 / \Delta n \left( \frac{X^i}{H^+} \right)_{\lambda} \right)}. \quad (3)$$

As solution, this self-consistent procedure gives the physical parameters that minimize  $\chi^2$  with an associated uncertainty based on the resulting values within  $\chi^2 - \chi^2_{\min} \leq 1$ . This method requires a strict control on the variables that affect the line fluxes, otherwise a spurious contribution appears, and can change the resulting parameters that minimize  $\chi^2$ . For example, undetected blends in the studied lines can result in an incorrect density and/or temperature determination.

We have considered several aspects to choose the set of [Fe III] lines that should be included in the maximum-likelihood process. First, we discard lines with evident line blending or contamination by telluric emission or ghosts. To test unnoticed line blends or inaccuracies in flux estimations, we use ratios of observed lines that should depend only on transition probabilities and not on physical conditions. The results are shown in Table 6. As it can be seen, there is a good agreement between the theoretical and observed values in the cases of [Fe III]  $\lambda 4778/\lambda 4734$ ,  $\lambda 4702/\lambda 4770$  and  $\lambda 4658/\lambda 4755$  line ratios. Deviations between the theoretical

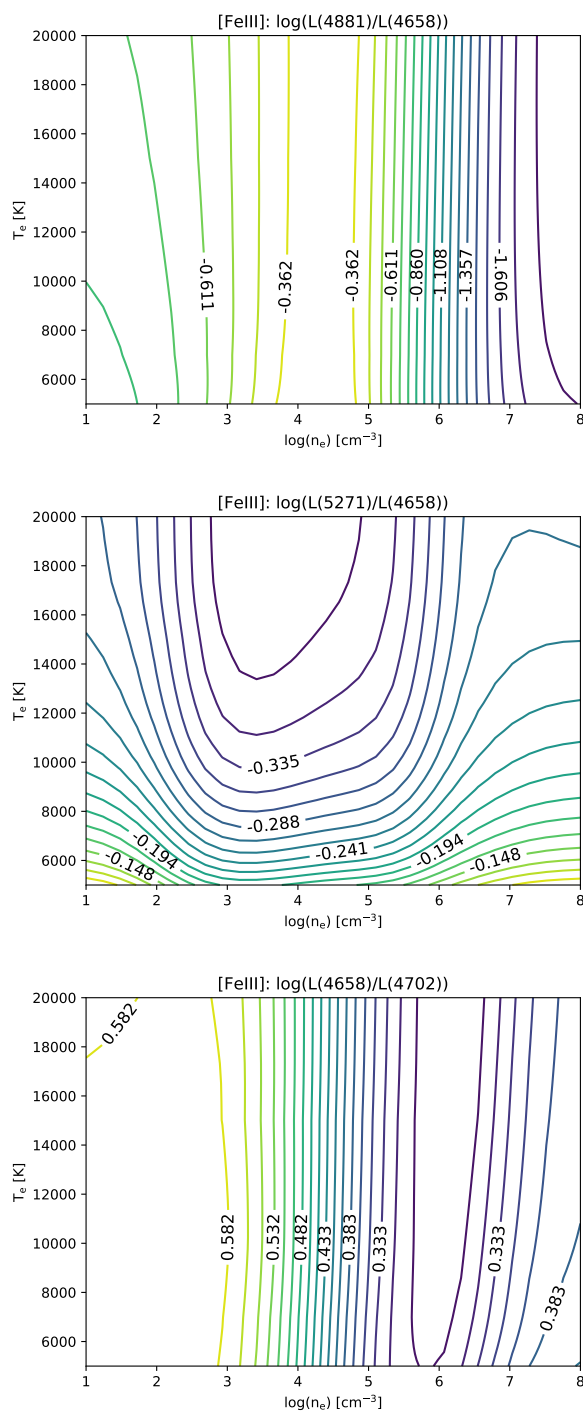


**Figure 5.** Predicted dependence of the [Fe III]  $\lambda 4881/\lambda 4658$ ,  $\lambda 5271/\lambda 4658$  and  $\lambda 4658/\lambda 4702$  line intensity ratios with physical conditions using the data of Table 3.

and the observed values in the cases of [Fe III]  $\lambda 4667/\lambda 4734$ ,  $\lambda 4778/\lambda 4667$ ,  $\lambda 4607/\lambda 4702$  and  $\lambda 4607/\lambda 4770$  line ratios are explained by the contamination of [Fe III]  $\lambda 4667$  by a ghost and by the blend of [Fe III]  $\lambda 4607$  with N II  $\lambda 4607.15$ . The line ratio with the largest deviation is [Fe III]  $\lambda 5011/\lambda 4085$ . This could be mainly due to the low signal-to-noise ratio of the [Fe III]  $\lambda 4085$  line. However, [Fe III]  $\lambda 5011$  is located close to [O III]  $\lambda 5007$  that present broad

wings in its line profile that affects the shape of the continuum close to [Fe III]  $\lambda 5011$  and perhaps the measurement of its line flux.

We select the following [Fe III] lines for the maximum-likelihood process:  $\lambda 14658.17$ ,  $4701.64$ ,  $4734.00$ ,  $4881.07$ ,  $5270.57$  and  $5412.06$ . This selection includes the brightest [Fe III] lines that are free of blends or telluric emissions and/or absorptions. We exclude fainter lines coming from the same upper level since they should have the same dependence on physical conditions and their incorporation would only increase the noise level of the results. This selection includes lines in a relatively small spectral range and hence, uncertainties in the reddening correction would have a negligible effect. This allows us to restrict the parameter space to electron density and temperature to test  $\chi^2$ . Studies on the primordial helium abundance have used similar maximum-likelihood procedures to calculate the  $\text{He}^+$  abundance, noting that this procedure can lead to degeneracies in the fitted parameters and  $\chi^2$  (see Olive & Skillman 2004; Aver et al. 2011, and references therein). Because of this, it is important to have an overview of the behaviour of  $\chi^2$  in the complete parameter space.

In Fig. 6 we present the convergence of  $\chi^2$  in the  $n_e - T_e$  space for both high-velocity and nebular components of cut 2. As it can be seen,  $\chi^2$  falls into a single minimum in each case, corresponding to  $T_e = 8500 \pm 1050$  K and  $n_e = 11880 \pm 1860$  cm $^{-3}$  in the high-velocity component and  $T_e = 8460 \pm 730$  K and  $n_e = 9430 \pm 1010$  cm $^{-3}$  in the nebular one. The  $T_e$  and  $n_e$  values obtained for the rest of cuts using this approach are presented in Table 5. The convergence to the resulting  $n_e$  is consistent with the diagnostic based on [Fe III]  $\lambda 4658/\lambda 4702$  ratio but with a smaller uncertainty due to the application of the  $\chi^2$  maximum-likelihood procedure. It is remarkable that in all cases, [Fe III] lines give  $n_e$  values higher than the diagnostics based on CELs of other ions as [S II] or [Cl III]. The largest difference is found in the high-velocity components, reaching almost a factor 3 in the high-velocity component of cut 3. The combination of the geometry of HH529 flow and dust destruction (see §10) can explain that difference. O'Dell et al. (2015) estimate a flow angle of 83° with respect to the sky plane for HH529, indicating that it is heading towards the observer. Therefore, the volume of gas integrated in the high-velocity components should include not only the denser gas of the head of the shock but also the jet beam gas behind. As we will see in §10, Fe abundance is higher at the shock components because of dust destruction (Mesa-Delgado et al. 2009; Espíritu et al. 2017), increasing the flux of [Fe III] lines relative to that of other CELs that are not so affected by this process. Therefore, the  $n_e$  determinations based on [Fe III] lines will be biased to the higher values of the density at the head of the shock.

In Table 5 we can see that the difference between  $T_e(\text{low})$  and  $T_e(\text{high})$  is larger for the shock components. As we can see from the plasma diagnostics shown in Fig. A1, the main contributor to  $T_e(\text{low})$ ,  $T([\text{N II}])$ , decreases as the  $n_e$  increases. We find that  $T([\text{N II}])$  almost reaches  $T([\text{O III}])$  when the densities obtained from [Fe III] lines are used to determine  $T([\text{N II}])$ . In fact this is the situation we would expect when the compressed area behind the shock front is a matter-bounded narrow slab, where we do not resolve stratification of the ionic species. This result reinforces that the high  $n_e$  values obtained from the [Fe III] should be the most appropriate ones for the compressed area behind the shock. Estimates of  $\text{Fe}^{2+}$  abundances based on  $T_e(\text{low})$  and  $T_e(\text{high})$  will be discussed separately in § 8.1.

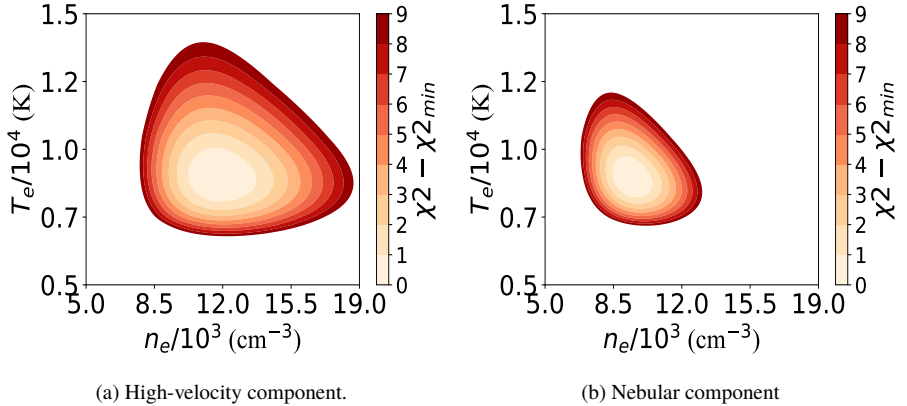
**Table 6.** Comparison of the observed [Fe III] intensity ratios and theoretical ones from Quintet (1996).

Ratio	Cut 1		Cut 2		Cut 3		Cut 4		Quinet (1996)
	Nebula	Shock	Nebula	Shock	Nebula	Nebula	Combined cuts		
4667/4734*	-	$0.52 \pm 0.04$	$0.42 \pm 0.02$	-	$0.45 \pm 0.03$	$0.43 \pm 0.03$	-	0.28	
4778/4734	$0.51 \pm 0.04$	$0.70 \pm 0.06$	$0.51 \pm 0.03$	$0.34 \pm 0.08$	$0.49 \pm 0.03$	$0.43 \pm 0.04$	$0.51 \pm 0.04$	0.48	
4778/4667*	-	$1.35 \pm 0.14$	$1.22 \pm 0.06$	-	$1.09 \pm 0.07$	$1.00 \pm 0.09$	-	1.74	
4607/4702**	$0.24 \pm 0.01$	$0.22 \pm 0.02$	$0.24 \pm 0.01$	$0.24 \pm 0.05$	$0.23 \pm 0.02$	$0.24 \pm 0.02$	$0.23 \pm 0.02$	0.17	
4607/4770**	$0.72 \pm 0.05$	$0.60 \pm 0.06$	$0.64 \pm 0.03$	$0.52 \pm 0.11$	$0.64 \pm 0.06$	$0.68 \pm 0.05$	$0.64 \pm 0.05$	0.51	
4702/4770	$2.96 \pm 0.15$	$2.68 \pm 0.16$	$2.73 \pm 0.10$	$2.22 \pm 0.27$	$2.74 \pm 0.19$	$2.87 \pm 0.14$	$2.72 \pm 0.14$	2.93	
4658/4755	$5.50 \pm 0.20$	$5.28 \pm 0.24$	$5.26 \pm 0.15$	$4.70 \pm 0.51$	$5.32 \pm 0.24$	$5.30 \pm 0.19$	$5.31 \pm 0.19$	5.49	
5011/5085	$3.19 \pm 0.72$	$2.51 \pm 0.93$	$5.00 \pm 1.00$	$2.96 \pm 1.22$	$3.61 \pm 0.46$	$3.84 \pm 0.94$	$3.66 \pm 0.96$	5.94	

\* λ4667 affected by ghost.

\*\* [Fe III]  $\lambda$ 4607.12 blended with N II  $\lambda$ 4607.15.

**Figure 6.** Distribution of  $\chi^2$  in the space of physical conditions derived from [Fe III] lines in the high-velocity component (left) and the nebular one (right) of cut 2.



#### 4.3 Physical conditions determined from recombination lines

#### 4.3.1 Physical conditions based on O II recombination lines

To estimate physical conditions based on O II recombination lines, we use the effective recombination coefficients from [Storey et al. \(2017\)](#). These coefficients fully account the dependence on electron density and temperature of the distribution population among the ground levels of O II. We follow a similar maximum-likelihood procedure as described in §4.2. In this case, we chose the observed lines from multiplet 1 and  $\lambda\lambda 4089.29, 4275.55$  from 3d-4f transitions, due to several reasons: (1) Lines from multiplet 1 are the brightest recombination lines of O II and are comparatively less affected by line blending or instrumental reflections as it is illustrated in Fig. 7. (2) The density dependence of intensity ratios of multiplet 1 lines relies on variations in the density population of  ${}^3P_J$  levels and formally reach the equilibrium with the statistical weight of the levels until  $n_{\text{crit}} \approx 10^5 \text{ cm}^{-3}$  ([Storey et al. 2017](#)). (3) O II  $\lambda\lambda 4089.29, 4275.55$  lines corresponding to 3d-4f transitions depend strongly on  $T_e$ . Nevertheless, these lines are relatively weak and we expect comparatively larger uncertainties in  $T_e$  determinations than using diagnostics based on CELs.

Fig. 8 shows  $\chi^2$ -maps in the space of  $T_e$  and  $n_e$  for the both components of cut 2. As it can be seen, the high velocity component has a temperature degeneracy within the 6000-23000 K range. This is not surprising, due to the fact that multiplet 1 is rather independent of  $T_e$  but highly dependent on  $n_e$  and the weak line  $\lambda 4275.55$  is the

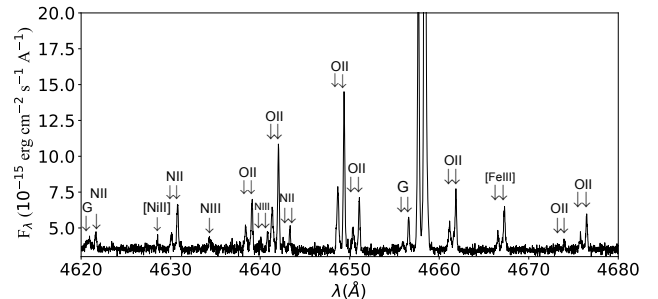


**Figure 7.** Section of the spectrum of cut 2 around the O II lines of multiplet 1.

only one that can break the degeneracy in this component since O II  $\lambda$ 4089.29 is blended with a ghost feature (see § 4.3.2). However, it is clear that the density dependence is well limited within a range of  $3000\text{--}3700 \text{ cm}^{-3}$ . Fixing the temperature to the adopted one for the high ionization zone using CELs, we obtain  $n_e = 3490 \pm 340 \text{ cm}^{-3}$  for the high velocity component. On the other hand, since we were able to use the O II  $\lambda$ 4089.29 together with  $\lambda$ 4275.55 in the nebular component, we have a convergence within a more limited area, although the error ranges remain wide. The physical conditions that minimizes  $\chi^2$  in this case are  $n_e = 4390 \pm 400 \text{ cm}^{-3}$  and  $T_e = 9350 \pm 1090 \text{ K}$ .

In Table 5, we can see that the density values obtained from

O II lines are similar to those obtained from other diagnostics in the nebular components but somewhat lower in the high velocity ones. This may be due to the weak dependence on density of O II lines from multiplet 1 from values  $\sim 10^4 \text{ cm}^{-3}$ , as it is shown in Fig. 4 from [Storey et al. \(2017\)](#). Therefore, the values obtained by this diagnostic may not be representative of the shock front.

#### 4.3.2 The alleged observation of Si IV $\lambda 4088.86$ line

Several authors used the  $I(\text{O II } \lambda 4649.13)/I(\text{O II } \lambda 4089.29)$  ratio to derive  $T_e$  based on its theoretical high dependence on  $T_e$  and low dependence on  $n_e$  (see e. g. [García-Rojas & Esteban 2007](#); [Fang & Liu 2013](#); [McNabb et al. 2013](#); [Wesson et al. 2018](#)). The low dependence of this ratio on  $n_e$  is because both lines come from the highest  $J$  of  ${}^3P_J$  levels, depending both on the population of the  ${}^3P_2$  ground level ([Storey et al. 2017](#)). Nevertheless, [Peimbert & Peimbert \(2013\)](#) discourages its use, due (among other reasons) to the possible contamination of O II  $\lambda 4089.29$  by the Si IV  $\lambda 4088.86$  line, granting lower  $T_e$  values. The authors consider that Si IV  $\lambda 4088.86$  has been detected in 2 H II regions observed with UVES echelle spectrograph at VLT telescope: the Orion Nebula ([Esteban et al. 2004](#)) and 30 Doradus ([Peimbert 2003](#)). Although it is a real possibility that a line like Si IV  $\lambda 4088.86$  may be detected in an H II region, much of the flux attributed to this line is actually due to an observational artifact of UVES spectrum.

[Fig. A2](#) shows the echelle orders extracted in an UVES blue arm spectrum using dichroic 2 ( $\Delta\lambda = 3750 - 4995$ ). Optical reflections produced by the dichroic 2 in the blue arm can be noted as vertical lines crossing the echelle orders. These artifacts are negligible with the exception of those produced by the most intense lines: [O III] $\lambda 4959$ , H $\beta$  and [O III] $\lambda 5007$  that, despite it does not enter in any complete echelle order in this arm, it is partially observed at the edge of the CCD, as well as its associated high-velocity component. As consequence 4 main sources of "ghost lines" can be immediately noticed, the third of them (from left to right), affects exactly the  $\lambda 4089.07$  position in the echelle order number 11 (bottom up) in our observations. Approximately at this wavelength we expect to have the high velocity component of O II  $\lambda 4089.29$  in cuts 2 and 3, but it must be free of emission from HH529III in cut 4. [Fig. 9](#) shows the emission around  $\lambda 4089.29$  in the spectra of cut 4, a pretty similar image than the [Fig. 2](#) from [Peimbert & Peimbert \(2013\)](#).

In our spectra, the Si IV  $\lambda 4088.86$  line, due to its high ionization potential, should be observed at  $\lambda 4089.08$ , considering the kinematical structure of the nebular component (see § 9.1). This means that in case of being detected, the Si IV  $\lambda 4088.86$  line would be indistinguishable from the ghost line at  $\lambda 4089.07$ . We have measured the intensity of ghost lines coming from the same source than  $\lambda 4089.07$  along the echelle orders but excluding those ones which are blended with other nebular lines. [Fig. A3](#) shows the decreasing trend of the intensity of ghost emission with respect to its source from higher to lower orders, as well as a least squares fit to predict ghost emission in order 11, where the emission feature at  $\lambda 4089.07$  lies. The predicted ghost emission in  $\lambda 4089.07$  is  $\frac{F(\lambda)}{F(\text{H}\beta)} = 0.007$  while the rms of the noise associated with the continuum in cut 4 around  $\lambda 4089.07$  represents a possible contribution of  $\frac{F(\text{rms})}{F(\text{H}\beta)} = 0.004$ . On the other hand, the measured flux of  $\lambda 4089.07$  is  $\frac{F(\lambda)}{F(\text{H}\beta)} = 0.012$ . Thus, the emission observed at  $\lambda 4089.07$  is consistent with purely ghost emission. This ghost emission affects in a similar way the spectra of the Orion Nebula and 30 Dor analyzed by [Esteban et al. \(2004\)](#) and [Peimbert \(2003\)](#), respectively.

The main drawback of the  $T_e$  diagnostic based on the  $I(\text{O II } \lambda 4649.13)/I(\text{O II } \lambda 4089.29)$  ratio in H II regions is that  $\lambda 4089.29$  is rather weak, providing uncertain  $T_e$  values. Therefore, this diagnostic will only be useful when the O II lines are well measured, or when the object shows significant difference between the  $T_e$  of the zone where the O II lines are formed and the rest of the nebula ([Wesson et al. 2018](#)). Finally, although Si IV lines are expected to be rather faint in normal H II regions, this may not be the case in high-ionization planetary nebulae (PNe) as NGC 3918 ([García-Rojas et al. 2015](#)).

#### 4.3.3 Electron temperature from He I recombination line ratios

Following the procedure used by [Zhang et al. \(2005\)](#) for PNe, we have used the  $I(\text{He I } \lambda 7281)/I(\text{He I } \lambda 6678)$  ratio for deriving  $T_e$  (He I) in our spectra. The use of those particular lines have several advantages. First,  $\lambda 7281$  and  $\lambda 6678$  are among the brightest He I RLs and their use minimizes observational errors. Second, they are produced in transitions between singlet levels, ensuring that they are free of significant self-absorption effects. We have explored the temperature dependence of other intensity ratios of He I  $\lambda 7281/\lambda$  with respect to other relevant singlet lines apart of  $\lambda 6678$  as  $\lambda 4388, 4922, 4438, 3614, 3965$  and  $5016$  using the recombination coefficients of [Porter et al. \(2012, 2013\)](#). The highest dependence on  $T_e$  for the studied ratios is reached with those transitions coming from  ${}^5\text{D}, {}^4\text{D}, {}^3\text{D}$  levels to  ${}^2\text{P}$  (see [Fig. A4](#)), the same down level of the transition that produces the He I  $\lambda 7281$  line, which comes from the  ${}^3\text{S}$  level. On the other hand, comparatively, the  $I(\text{He I } \lambda 7281)/I(\text{He I } \lambda 6678)$  ratio has the smallest  $n_e$  dependence, agreeing with the conclusion by [Zhang et al. \(2005\)](#), despite using different recombination coefficients.

[Fig. A5](#) shows that the  $T_e$  dependence of  $I(\text{He I } \lambda 7281)/I(\text{He I } \lambda 6678)$  ratio is practically linear in the interval  $5000 \text{ K} \leq T_e(\text{K}) \leq 10000 \text{ K}$ . The deviation between the determination of  $T_e(\text{He I})$  using a linear fit (as in Eq. (4)) and a more complex interpolation of the recombination coefficients of [Porter et al. \(2012, 2013\)](#) is always smaller than 35 K. At  $T_e > 10000 \text{ K}$ , any linear fit will fail for almost all  $n_e$  values except for the lowest ones ( $n_e \leq 100 \text{ cm}^{-3}$ ). In these cases, a more complex treatment is necessary to estimate  $T_e(\text{He I})$ . The linear fit (slope and intercept) varies significantly in the lower density ranges, and tends to remain almost constant for densities  $n_e \geq 10000 \text{ cm}^{-3}$ .

$$T_e(\text{He I})(\text{K}) = \alpha \left[ \frac{I(\lambda 7281)}{I(\lambda 6678)} \right] + \beta. \quad (4)$$

In Table A1, we present the slope and intercept values given by Eq. (4) for a density range representative for H II regions and some PNe. In this table we also include average  $T_e(\text{He I})$  values obtained with  $I(\lambda 7281)/I(\lambda 6678)$ ,  $I(\lambda 7281)/I(\lambda 4922)$  and  $I(\lambda 7281)/I(\lambda 4388)$  ratios, all consistent with each other, for all components of all spectra.

#### 4.4 Electron temperature determinations from nebular continuum.

Thanks to the high signal-to-noise ratio of our spectra, we can obtain a reasonable determination of the Balmer and Paschen discontinuities of the nebular continuum in the spectrum resulting from adding all the cuts (see [Fig. 10](#)). We have determined the  $T_e$  for the nebular continuum using both discontinuities. We used Eq. (5), taken from [Liu et al. \(2001\)](#) for  $\text{He}^{2+}/\text{H}^+ = 0$  to estimate  $T_e(\text{H I})_{\text{Balmer}}$ . This

**Figure 8.** Distribution of  $\chi^2$  in the space of physical conditions derived from O II lines in the high-velocity component (left) and the nebular one (right) of cut 2.

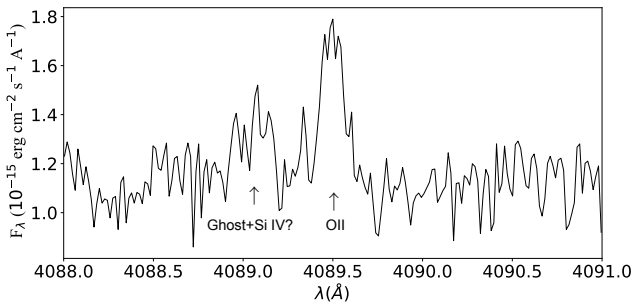
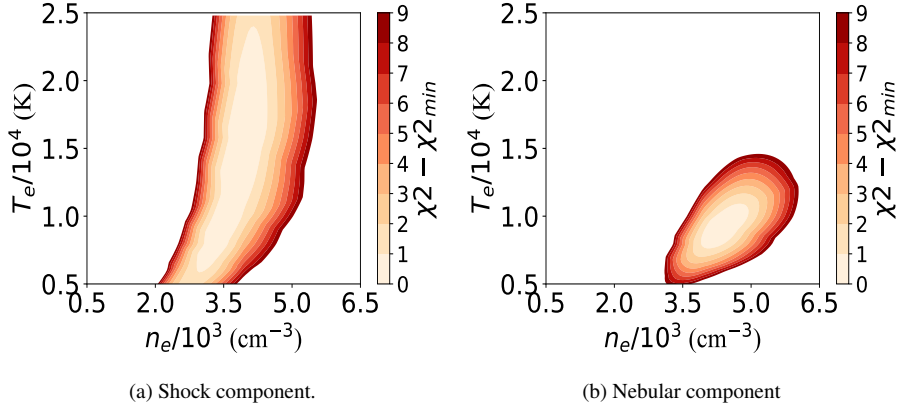


**Figure 9.** Emission spectrum of cut 4 around  $\lambda 4089.29$ . This cut does not contain high velocity components.

formula is based on theoretical continuum emission of HI, He I and He II calculated by Brown & Mathews (1970) and the theoretical line emission of HI  $\lambda 3770.63$  (H11) from Storey & Hummer (1995). Analogously, we used Eq. (6), taken from Fang & Liu (2011) to estimate  $T_e(\text{HI})_{\text{Paschen}}$  using the measured Paschen discontinuity and the intensity of H I  $\lambda 8862.78$  (P11) line.

$$T_e(\text{HI})_{\text{Balmer}}(\text{K}) = 368 \times \left( 1 + 0.259 \frac{\text{He}^+}{\text{H}^+} + 3.409 \frac{\text{He}^{2+}}{\text{H}^+} \right) \left( \frac{\text{BJ}}{\text{H11}} \right)^{-3/2}. \quad (5)$$

$$T_e(\text{HI})_{\text{Paschen}}(\text{K}) = 8.72 \times \left( 1 + 0.52 \frac{\text{He}^+}{\text{H}^+} + 4.40 \frac{\text{He}^{2+}}{\text{H}^+} \right) \left( \frac{\text{PJ}}{\text{P11}} \right)^{-1.77}. \quad (6)$$

In both cases, the estimation of the temperature requires a precise fit to the continuum emission at both sides of  $3646 \text{ \AA}$  and  $8204 \text{ \AA}$ , the approximate wavelengths of the Balmer and Paschen discontinuities, respectively. In all individual cuts, the noise level of the continuum results into large uncertainties in the estimation of the temperature. For this reason, the best estimate is obtained by using the spectrum resulting from adding all the cuts. However, this has the drawback of mixing the emission contributions of the nebular and the shock components in the continuum. As Bohigas (2015) remarks, the total  $T_e(\text{HI})$  would be the weighted average of the individual values of the mixed nebular components, in this case,

the high velocity and nebular components, where the weights would be the  $\text{H}^+$  mass of each component.

Fig. 10 shows the discontinuities and the fitted Balmer and Paschen continua. It must be remarked that the continuum redder to the Paschen discontinuity is very affected by telluric emissions and absorptions, so the estimation of the discontinuity is rather uncertain. Determining the exact position of the continuum redward  $8204 \text{ \AA}$  is very difficult and, consequently, the  $T_e(\text{HI})_{\text{Paschen}}$  determination shows a large error. In fact, depending on the adopted zones for the fitting of the red continuum at the Paschen discontinuity, we can get a  $T_e(\text{HI})_{\text{Paschen}}$  ranging from 6320 to 16290 K. For this reason, we want to keep us conservative and just give an upper limit as it is shown in Table 5.

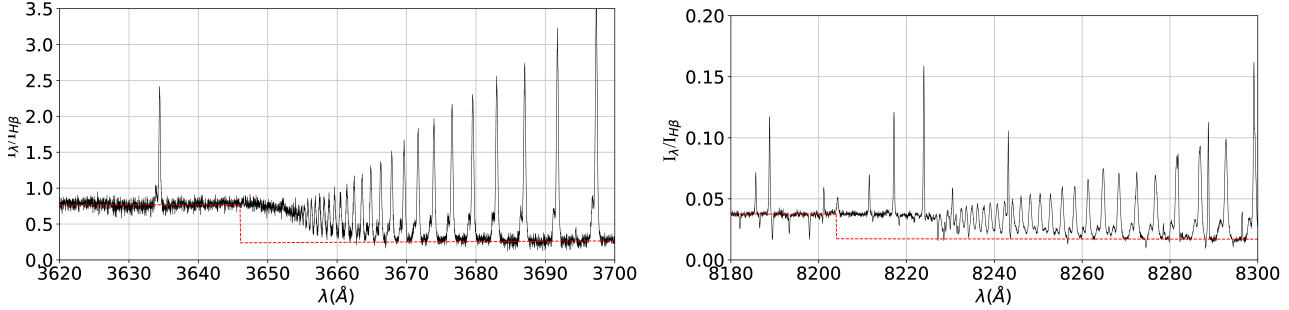
## 5 CHEMICAL ABUNDANCES

### 5.1 Ionic abundances from CELs

Using the transition probabilities and collisional strengths from Table 3, we estimate the ionic abundances based on the observed CELs using the PyNeb routines. Abundances for  $\text{O}^+$ ,  $\text{N}^+$ ,  $\text{S}^+$ ,  $\text{Ni}^{2+}$  and  $\text{Cl}^+$  were derived using the  $n_e$  and  $T_e(\text{low})$  adopted for each component of each cut, while abundances for  $\text{O}^{2+}$ ,  $\text{Ne}^{2+}$ ,  $\text{Cl}^{3+}$ ,  $\text{Fe}^{3+}$ ,  $\text{Ar}^{2+}$  and  $\text{Ar}^{3+}$  rely on the adopted  $T_e(\text{high})$ .  $\text{S}^{2+}$  and  $\text{Cl}^{2+}$  abundances were derived using  $T_e(\text{[S III]})$ . In the case of  $\text{Fe}^{2+}$ , estimations of its abundance are presented using both  $T_e(\text{high})$  and  $T_e(\text{low})$  (see Table A2 and Table A3), considering that in § 4.2 it was shown that the lines of [Fe III] converged at a temperature close to  $T_e(\text{high})$ . This will be analyzed in § 8, showing that considering any of both temperatures, there is an increase in the total abundance of Fe in the high-velocity components with respect to the nebular gas. General results are presented in Table 9.

#### 5.1.1 $\text{Cl}^{2+}$ and $\text{Cl}$ abundances

Domínguez-Guzmán et al. (2019) have proposed the use of  $T_e([\text{N II}])$  to determine the  $\text{Cl}^{2+}$  abundance in a sample of 37 Galactic and extragalactic H II regions, including the Orion Nebula (they use the data by Esteban et al. 2004). They argue in favour of the use of such  $T_e$  indicator because it reduces the dispersion of the Cl/O ratio of their sample and remove trends in the Cl/O versus O/H relation. However, in a detailed study of each specific object, the optimal

**Figure 10.** Balmer and Paschen discontinuities of the resulting spectrum after adding all cuts.

temperature to adopt can differ from what statistically would be the best choice. Assuming a two ionization zones approximation with two different  $T_e$  depending on the IP of the ions, it is not obvious which  $T_e$  is the most appropriate for an ion as  $\text{Cl}^{2+}$  whose threshold of existence (23.81–39.61 eV) is rather in between the  $\text{N}^+$  (14.53–29.6 eV) and  $\text{O}^{2+}$  (35.12–54.94 eV), whose representative  $T_e$  are normally assumed as the ones of the low and high ionization zone, respectively. In this sense, we expect that a  $T_e$  representative of an intermediate ionization zone as  $T_e(\text{[S III]})$  should be more appropriate for  $\text{Cl}^{2+}$ . However, in general, the measurement of  $T_e(\text{[S III]})$  has the inconvenient that  $\text{[S III]} \lambda\lambda 9069, 9531$  lines fall in a spectral region that is commonly affected by telluric absorption bands (Noll et al. 2012). In §4 we commented that the  $\text{[S III]} \lambda 9069$  line is affected by telluric absorption while  $\text{[S III]} \lambda 9531$  is not. Berg et al. (2020), using observations of H II regions in four spiral galaxies, explore  $T_e$  relationships finding that the linear correlation between  $T_e(\text{[N II]})$  and  $T_e(\text{[S III]})$  shows a larger dispersion as ionization degree increases. For objects with the higher ionization degree, a linear correlation between  $T_e(\text{[O III]})$  and  $T_e(\text{[S III]})$  seems to be more appropriate. In this work, we are able to calculate the total Cl abundance from our spectra because we measure CELs of all the ionization species of Cl that can be present in the Orion Nebula. We test the resulting Cl abundance taken three different temperatures:  $T_e(\text{low})$ ,  $T_e(\text{[S III]})$  and  $T_e(\text{high})$ . As it was said in §4.1,  $T_e(\text{low})$  and  $T_e(\text{high})$  were defined as the weighted average of the  $T_e$  values given by different diagnostics, but their values are actually very similar to  $T_e(\text{[O III]})$  and  $T_e(\text{[N II]})$ , respectively. In Table A4, we present the  $\text{Cl}^{2+}$  and Cl abundances as well as their corresponding Cl/O ratios using the three aforementioned temperatures. Using  $T_e(\text{low})$  in all cuts and components, we would have a Cl/H ratio about 0.2 dex lower in the shock component of cut 3, which is difficult to explain apart from the use of an inappropriate  $T_e$ . Abundance variations might be due to different depletion fractions onto dust grains in both components. However, the fraction of Cl depleted into dust grains in the ISM and in H II regions in particular is actually unknown. The Cl abundance in diffuse and dense interstellar clouds is quite uncertain and its observed trend is rather irregular (Jenkins 2009). In any case, if the Cl/H differences between the components are due to dust depletion effects, this would indicate that the fraction of Cl in dust is larger in the high-velocity component, which is certainly a quite unlikely scenario. Another possibility is that a substantial part of Cl is in ionization species unobservable in the optical spectrum, as  $\text{Cl}^{4+}$ . However, the ionization conditions of the Orion Nebula rules out this possibility. As we can see in Table A4, this inconsistency disappears if we adopt  $T_e(\text{[S III]})$  or  $T_e(\text{high})$  to estimate the  $\text{Cl}^{2+}$  abundance. On the other hand, we obtain a mean Cl/O ratio of  $-3.64 \pm 0.06$ ,  $-3.42 \pm 0.02$  or  $-3.50 \pm 0.02$  when adopting  $T_e(\text{low})$ ,  $T_e(\text{high})$  or  $T_e(\text{[S III]})$  to calculate the  $\text{Cl}^{2+}$  abundance.

The Cl/O ratio obtained using  $T_e(\text{[S III]})$  is the one closest to the solar value of  $-3.50 \pm 0.09$  recommended by Lodders (2019). However, all determinations are consistent with the solar values within the errors.

### 5.1.2 $\text{Ni}^{2+}$ abundance

The first estimation of the Ni abundance in an H II region was made by Osterbrock et al. (1992) for the Orion Nebula. They used estimates of the atomic data of Ni ions, considering  $[\text{Ni II}]$  and  $[\text{Ni III}]$  lines. Since then, the number of Ni abundance determinations in ionized nebulae is still very limited, both for PNe (Zhang & Liu 2006; García-Rojas et al. 2013; Delgado-Inglada et al. 2016) and H II regions (Mesa-Delgado et al. 2009; Delgado-Inglada et al. 2016). There is a considerable amount of  $[\text{Ni II}]$  and  $[\text{Ni III}]$  lines in our spectra. However,  $[\text{Ni II}]$  lines are affected by fluorescence (Lucy 1995) and their use to calculate the abundance of  $\text{Ni}^+$  is restricted to some particular cases as low-excitation nebulae (Zhang & Liu 2006). On the other hand,  $[\text{Ni III}]$  lines are, in principle, not affected by fluorescence effects and can be used to derive  $\text{Ni}^{2+}$  abundances. From all the detected  $[\text{Ni III}]$  lines, we chose  $[\text{Ni III}] \lambda\lambda 6000, 6534, 6682, 6797, 6946$  and 7890 because they are not either affected by blends or telluric absorption.

As we commented in §4, all tested diagnostics based on  $[\text{Ni III}]$  lines do not provide reliable values of physical conditions, indicating inaccuracies between the observed lines and the theoretical predictions. Delgado-Inglada et al. (2016) studied the Fe/Ni ratio in eight PNe and three H II regions, including the Orion Nebula. They used different datasets for these last objects, including the high resolution ones from Esteban et al. (2004) and Mesa-Delgado et al. (2009) (which includes HH202), and some of their own observations covering approximately the same area as the Position 1 of Esteban et al. (1998) and the brightest part of the Orion Bar. We have compared our data with some observed flux ratios compiled by Delgado-Inglada et al. (2016) looking for possible undetected line blends or observational inaccuracies. For convenience, we have compared the predicted and observed flux ratios of  $[\text{Ni III}] \lambda\lambda 6000, 6534$  and 6946 lines that arise from the same atomic level and their intensity ratios should be constant. In Table 7, we compare the observed flux ratios and the predicted ones using the atomic data of  $\text{Ni}^{2+}$  by Bautista (2001).

As Table 7 shows, the  $[\text{Ni III}] \lambda 6534/\lambda 6000$  and  $\lambda 6946/\lambda 6000$  intensity ratios are rather inconsistent with the predicted ones. This seems to be due to an inconsistency between predicted and measured flux in  $[\text{Ni III}] \lambda 6000$  line. However, we discard the presence of observational features or sky emission affecting this line. In addition, there are no candidates of unusual lines in the literature or in

**Table 7.** Comparison of the observed [Ni III] intensity ratios and theoretical ones from [Bautista \(2001\)](#).

Ratio	<a href="#">Esteban et al. (2004)</a>	<a href="#">Mesa-Delgado et al. (2009)</a> Shock HH202	<a href="#">Delgado-Inglada et al. (2016)</a> Orion Bar	This work Nebular	This work High velocity Cut 2	Predicted
6534/6000	$2.09 \pm 0.94$	$1.58 \pm 0.38$	$1.46 \pm 0.40$	$1.54 \pm 0.39$	$3.35 \pm 1.40$	2.19
6946/6000	-	$0.28 \pm 0.09$	-	$0.31 \pm 0.11$	$0.82 \pm 0.52$	0.39

**Table 8.** Heliocentric velocities of [Ni III] lines (in km s<sup>-1</sup>) for each component and cut. Typical error is between 1–2 km s<sup>-1</sup>

$\lambda$ (Å)	Cut 1		Cut 2		Cut 3		Cut 4
	Nebula	High-Velocity	Nebula	High-Velocity	Nebula	Nebula	
6000	21.39	-26.08	19.39	-	20.39	18.89	
6534	8.77	-32.52	7.86	-26.10	6.94	6.48	
6682	3.36	-	6.50	-	3.81	-	
6797	4.75	-42.00	2.55	-	1.22	1.66	
6946	6.97	-37.49	6.10	-32.31	4.38	6.10	
7890	20.32	-24.52	20.32	-19.20	19.18	19.56	

the Atomic Line List v2.05b21 with a wavelength difference below to 0.15 Å (a conservative limit for an appropriate deblending of Gaussian profiles at our spectral resolution) that may be blended with [Ni III]  $\lambda 6000$  line.

An apparently discordant behaviour is also noticeable in the kinematic structure of [Ni III] lines. As we can see in Table 8, there is a considerably difference between the observed heliocentric velocity in each line contrary to what we would expect for lines that are emitted in the same volume or component of the nebula (see § 9.1). These differences are larger than the expected ones considering the uncertainties of the theoretical wavelengths given by the Atomic Line List v2.05b21:  $\lambda\lambda 6000.16 \pm 0.05$ ,  $6533.76 \pm 0.06$ ,  $6682.16 \pm 0.06$ ,  $6797.05 \pm 0.07$ ,  $6946.39 \pm 0.07$  and  $7889.93 \pm 0.09$ , which are taken from the work of [Sugar & Corliss \(1985\)](#).

The problems discussed above translate in an inconsistent pattern of Ni<sup>2+</sup> abundances in all cuts and components. Table A5 shows that Ni<sup>2+</sup>/H<sup>+</sup> ratios vary significantly from one line to another, with differences up to 0.8 dex. This problem would also affect the results obtained by [Esteban et al. \(2004\)](#), [Mesa-Delgado et al. \(2009\)](#) or [Delgado-Inglada et al. \(2016\)](#). We consider that the nowadays available energy levels and atomic data of Ni<sup>2+</sup> are not accurate enough to derive confident values of its ionic abundances. Therefore, our Ni<sup>2+</sup> abundances must be taken with care, since they include unknown uncertainties.

## 5.2 Ionic abundances from RLs

### 5.2.1 He<sup>+</sup> abundance

To estimate the He<sup>+</sup> abundance, we use the flux of some of the most intense He I lines:  $\lambda\lambda 3188$ , 3614, 3889, 3965, 4026, 4388, 4438, 4471, 4713, 4922, 5016, 5876, 6678, 7065, 7281. He I  $\lambda\lambda 4121$ , 5048 lines were discarded because they are contaminated by ghost lines (see § 4.3.2). The 15 selected lines correspond to both singlet and triplet configurations, as it is shown in Fig. A4. The fluxes of triplet lines are affected by the meta-stability of the 2<sup>3</sup>S level. The comparatively much longer lifetime of 2<sup>3</sup>S, promotes re-excitations of bounded electrons by self-absorption of line photons, altering the flux ratios predicted by recombination theory for some He I lines. For example, self-absorption of He I  $\lambda 3188$  photons can increase the flux of He I  $\lambda\lambda 3889$ , 5876 and 7065 lines at the expense of He I  $\lambda 3188$ , which flux decreases accordingly. On the other hand,

self-absorption of the He I  $\lambda 3889$  line is also important and increase of the flux of He I  $\lambda 7065$  at the expense of He I  $\lambda 3889$ . The effects of self-absorption are stronger as optical depth of the triplet lines related to the 2<sup>3</sup>S level increases. However, the sum of the fluxes of He I  $\lambda\lambda 3188$ , 3889, 4713, 5876, and 7065 lines should remain independent of the optical depth (parameterized by  $\tau_{3889}$  or  $\tau_{3188}$ , [Porter et al. 2007](#)).

In Table 10, we show the He<sup>+</sup> abundances determined using the fluxes of He I  $\lambda\lambda 3188$ , 3889, 4713, 5876, and 7065 lines and the values of  $n_e$  and  $T_e(\text{He I})$  corresponding to each component of each cut. In the same table, we also include the He<sup>+</sup> abundance obtained from the sum of the fluxes of all the individual lines of the table and re-distributing it assuming  $\tau_{3188} = \tau_{3889} = 0$ . In Table 11 we show the He<sup>+</sup> abundances determined from singlet lines and those triplet ones that are expected to be less affected by self-absorption (see Table 2 from [Benjamin et al. 2002](#)). Tables 10 and 11 show a good agreement between the average values of He<sup>+</sup>/H<sup>+</sup> ratios included in Table 11 (the last row) and those obtained summing the fluxes of lines included in Table 10. This last table also shows that the self-absorption effects are less important in the high velocity gas than in the nebular one. This is noticeable in the larger dispersion of the abundances obtained with each individual line without considering the effects of self-absorption and that obtained redistributing the fluxes as expected at  $\tau = 0$  in the nebular components. As it is discussed in [Osterbrock & Ferland \(2006](#), see their figure 4.5) if the nebula has ionized zones with different velocities, the self-absorption effects can be reduced due to the Doppler shift between the emitting and absorbing zones. For example, the effect of the self-absorption in the intense He I  $\lambda 5876$  line is remarkable in the nebular component, giving He<sup>+</sup> abundances about 0.05 dex higher than the sum value. In this sense, the common procedure of using a flux-weighted average of He I  $\lambda 5876$  and other bright optical He I lines (as  $\lambda\lambda 4471$  and 6678) for obtaining the mean He<sup>+</sup> abundance would provide rather an upper limit of it.

Another interesting fact that can be noted in Table 11 is that the He<sup>+</sup> abundance determined from the He I  $\lambda 5016$  line is lower than that obtained from other lines in the high velocity components. An abnormally low flux of this line was noted by [Esteban et al. \(2004\)](#), and this was attributed to self-absorption effects in the singlet configuration of He I. [Porter et al. \(2007\)](#) discussed this, proposing that the most likely explanation is a deviation from case B of the He I  $\lambda\lambda 537.0$  and 522.0 lines, that go to the ground level, partially escaping before being reabsorbed. This is probably the case in the high velocity components where any kind of self-absorption of photons from the "static" nebular gas should be reduced.

### 5.2.2 O<sup>2+</sup> abundance

We calculate the O<sup>2+</sup> abundance using the RLs presented in Table 12 and the  $n_e$  determined from O II lines (as is described in § 4.3.1) and the  $T_e(\text{high})$  adopted for each component of each cut. The abundance calculation (as well as the  $n_e$  estimation) is based on the recombination coefficients calculated by [Storey et al. \(2017\)](#).

**Table 9.** Chemical abundances based on CEL's without considering the temperature fluctuations scenario ( $t^2 = 0$ ).

Ion	Cut 1		Cut 2		Cut 3		Cut 4	Combined cuts
	Nebula	Shock	Nebula	Shock	Nebula	Nebula	Nebula	
O <sup>+</sup>	7.88 ± 0.04	7.20 <sup>+0.12</sup> <sub>-0.09</sub>	7.83±0.06	7.14 <sup>+0.14</sup> <sub>-0.09</sub>	7.76 <sup>+0.07</sup> <sub>-0.06</sub>	7.81 <sup>+0.07</sup> <sub>-0.06</sub>	7.75 ± 0.05	
O <sup>2+</sup>	8.32 ± 0.03	8.54 ± 0.02	8.35 ± 0.03	8.44 ± 0.02	8.35 <sup>+0.03</sup> <sub>-0.02</sub>	8.36 ± 0.03	8.37 ± 0.03	
N <sup>+</sup>	7.00 ± 0.02	6.12 <sup>+0.07</sup> <sub>-0.06</sub>	6.99 ± 0.03	6.29 <sup>+0.08</sup> <sub>-0.06</sub>	6.91 <sup>+0.04</sup> <sub>-0.03</sub>	6.98 <sup>+0.04</sup> <sub>-0.03</sub>	6.89 ± 0.03	
Ne <sup>2+</sup>	7.67 ± 0.04	7.90 ± 0.03	7.70 <sup>+0.04</sup> <sub>-0.03</sub>	7.77 ± 0.03	7.73 ± 0.03	7.75 <sup>+0.04</sup> <sub>-0.03</sub>	7.73 <sup>+0.04</sup> <sub>-0.03</sub>	
S <sup>+</sup>	5.58 ± 0.05	4.73 <sup>+0.08</sup> <sub>-0.07</sub>	5.57 <sup>+0.05</sup> <sub>-0.04</sub>	4.85 <sup>+0.09</sup> <sub>-0.07</sub>	5.53 <sup>+0.06</sup> <sub>-0.05</sub>	5.59 ± 0.05	5.49 ± 0.05	
S <sup>2+</sup>	6.79 ± 0.04	6.92 <sup>+0.05</sup> <sub>-0.04</sub>	6.85 <sup>+0.09</sup> <sub>-0.07</sub>	6.86 <sup>+0.06</sup> <sub>-0.05</sub>	6.86 <sup>+0.05</sup> <sub>-0.04</sub>	6.82 <sup>+0.05</sup> <sub>-0.04</sub>	6.85 ± 0.04	
Cl <sup>+</sup>	3.72 ± 0.04	2.92 <sup>+0.14</sup> <sub>-0.13</sub>	3.71 ± 0.04	<3.02	3.68 ± 0.04	3.75 ± 0.04	3.63 ± 0.04	
Cl <sup>2+</sup>	4.88 <sup>+0.06</sup> <sub>-0.05</sub>	5.01 <sup>+0.06</sup> <sub>-0.05</sub>	4.93±0.06	4.95 <sup>+0.08</sup> <sub>-0.06</sub>	4.96 <sup>+0.06</sup> <sub>-0.05</sub>	4.95 <sup>+0.06</sup> <sub>-0.05</sub>	4.94 <sup>+0.05</sup> <sub>-0.04</sub>	
Cl <sup>3+</sup>	3.28 ± 0.06	3.59 ± 0.05	3.28 <sup>+0.04</sup> <sub>-0.03</sub>	3.39 ± 0.10	3.33 ± 0.04	3.45 ± 0.04	3.38 ± 0.05	
Ar <sup>2+</sup>	6.31 ± 0.03	6.39 ± 0.02	6.31 ± 0.03	6.34 ± 0.03	6.33 ± 0.02	6.29 ± 0.03	6.32 ± 0.03	
Ar <sup>3+</sup>	4.39 <sup>+0.06</sup> <sub>-0.05</sub>	4.69 ± 0.04	4.47 <sup>+0.04</sup> <sub>-0.03</sub>	4.50 ± 0.07	4.50 ± 0.04	4.61 <sup>+0.04</sup> <sub>-0.03</sub>	4.52 <sup>+0.05</sup> <sub>-0.04</sub>	
*Fe <sup>2+</sup>	5.77 ± 0.02	5.93 ± 0.05	5.82 ± 0.02	5.73 ± 0.05	5.78 ± 0.02	5.76 ± 0.03	5.80 ± 0.02	
**Fe <sup>2+</sup>	5.52 ± 0.03	5.56 ± 0.08	5.57 ± 0.02	5.28 ± 0.06	5.52 ± 0.04	5.48 ± 0.03	5.53 ± 0.04	
Fe <sup>3+</sup>	5.68 <sup>+0.13</sup> <sub>-0.11</sub>	6.23 <sup>+0.10</sup> <sub>-0.09</sub>	5.70 <sup>+0.09</sup> <sub>-0.08</sub>	<6.47	5.73 <sup>+0.11</sup> <sub>-0.10</sub>	5.73 <sup>+0.13</sup> <sub>-0.12</sub>	5.75 <sup>+0.11</sup> <sub>-0.10</sub>	
Ni <sup>2+</sup>	4.37 ± 0.14	4.47 ± 0.11	4.33 ± 0.17	4.18 ± 0.12	4.32 ± 0.16	4.36 ± 0.12	4.38 ± 0.10	

\* indicates that  $T_e$  (high) was used.\*\* indicates that  $T_e$  (low) was used.**Table 10.** He<sup>+</sup> abundances for He I triplet lines most affected by self-absorption.

$\lambda_0$ (Å)	Cut 1		Cut 2		Cut 3		Cut 4	Combined Cuts
	Nebula	Shock	Nebula	Shock	Low Velocity	Shock + Nebula	Nebula	
3188	10.67 ± 0.02	10.92 ± 0.02	10.63 ± 0.02	10.96 ± 0.04	10.62 ± 0.02	10.68 ± 0.02	10.71 ± 0.02	
3889	10.60 ± 0.02	10.94 ± 0.02	10.52 ± 0.02	10.75 ± 0.02	10.42 ± 0.02	10.55 ± 0.02	10.61 ± 0.02	
4713	11.01 ± 0.03	11.11 ± 0.03	11.04 ± 0.03	11.01 ± 0.03	11.07 ± 0.02	11.11 ± 0.02	11.07 ± 0.02	
5876	10.96 ± 0.01	10.96 ± 0.01	10.97 ± 0.01	10.93 ± 0.01	10.98 ± 0.01	10.96 ± 0.01	10.97 ± 0.01	
7065	11.34 ± 0.04	11.23 ± 0.05	11.35 ± 0.04	11.17 ± 0.04	11.34 ± 0.04	11.37 ± 0.04	11.34 ± 0.04	
<b>Sum</b>	<b>10.91 ± 0.02</b>	<b>10.96 ± 0.02</b>	<b>10.90 ± 0.02</b>	<b>10.92 ± 0.03</b>	<b>10.89 ± 0.02</b>	<b>10.90 ± 0.02</b>	<b>10.91 ± 0.02</b>	

**Table 11.** He<sup>+</sup> abundances for He I singlet lines and the triplet ones less affected by self-absorption.

$\lambda_0$ (Å)	Cut 1		Cut 2		Cut 3		Cut 4	Combined Cuts
	Nebula	Shock	Nebula	Shock	Low Velocity	Shock + Nebula	Nebula	
3614	10.93 ± 0.02	10.85 ± 0.04	10.89 ± 0.02	11.09 ± 0.05	10.86 ± 0.02	10.85 ± 0.02	10.89 ± 0.02	
3965	10.88 ± 0.01	10.86 ± 0.02	10.89 ± 0.01	10.93 ± 0.02	10.87 ± 0.01	10.88 ± 0.01	10.89 ± 0.01	
4026	10.89 ± 0.01	10.98 ± 0.01	10.90 ± 0.01	11.01 ± 0.01	10.93 ± 0.01	10.93 ± 0.01	10.93 ± 0.01	
4388	10.90 ± 0.01	10.96 ± 0.01	10.92 ± 0.01	10.97 ± 0.02	10.91 ± 0.01	10.91 ± 0.01	10.91 ± 0.01	
4438	10.95 ± 0.03	10.88 ± 0.04	10.92 ± 0.02	11.08 ± 0.07	10.92 ± 0.02	10.91 ± 0.03	10.94 ± 0.03	
4471	10.87 ± 0.01	10.97 ± 0.01	10.90 ± 0.01	10.93 ± 0.01	10.91 ± 0.01	10.93 ± 0.01	10.91 ± 0.01	
4922	10.90 ± 0.01	10.94 ± 0.01	10.92 ± 0.01	10.94 ± 0.01	10.92 ± 0.01	10.92 ± 0.01	10.92 ± 0.01	
5016	10.87 ± 0.01	10.78 ± 0.02	10.88 ± 0.01	10.84 ± 0.02	10.88 ± 0.01	10.88 ± 0.01	10.87 ± 0.01	
6678	10.90 ± 0.02	10.94 ± 0.02	10.91 ± 0.01	10.93 ± 0.02	10.92 ± 0.02	10.90 ± 0.01	10.92 ± 0.02	
7281	10.90 ± 0.03	10.95 ± 0.03	10.92 ± 0.03	10.92 ± 0.04	10.92 ± 0.03	10.91 ± 0.03	10.93 ± 0.03	
<b>Average</b>	<b>10.89 ± 0.02</b>	<b>10.95 ± 0.03</b>	<b>10.90 ± 0.01</b>	<b>10.95 ± 0.03</b>	<b>10.90 ± 0.02</b>	<b>10.91 ± 0.02</b>	<b>10.91 ± 0.02</b>	

This coefficients consider the distribution of population among the O<sup>2+</sup> levels with some improvements over similar estimates from Bastin & Storey (2006). Previous works on recombination coefficients of O II as Storey (1994) assumed that the O<sup>2+</sup> levels are populated according to their statistical weight, which is not suitable for densities below the critical one.

In Table 12, we present the weighted average abundance for each multiplet. In the last row of Table 12 we give the final O<sup>2+</sup> abundance obtained averaging the values obtained for multiplets 1, 2, 10, 20 and 3d – 4f transitions. These multiplets and transitions give consistent values and were also considered by Esteban et al. (2004) for determining their mean values. However, we decided to consider only the abundance obtained from multiplet 1 as representative of the O<sup>2+</sup> abundance. This is because, although it gives values consistent with the average of the other aforementioned multiplets and transitions, the inclusion of the results for several multiplets with fainter lines increases the formal uncertainties of the final mean O<sup>2+</sup> abundance.

### 5.2.3 Determination of the abundance of other heavy elements based on RLs.

Due to the high quality of our deep spectra, we were able to determine abundances of other heavy element ions such as O<sup>+</sup>, C<sup>2+</sup> and Ne<sup>2+</sup> based on the fluxes of RLs and the recombination coefficients presented in Table 4.

O<sup>+</sup> abundances were obtained from the lines of multiplet 1 of O I  $\lambda\lambda$  7771.94, 7774.17 and 7775.39 together with the adopted density and temperature of the low ionization zone for each component of each cut. Due to the high spectral resolution of our data, these O I lines are not blended with telluric emission features as it is shown in Fig 11. We do not detect the lines of multiplet 1 of O I in the high velocity components. In these cases, we have estimated upper limits of their intensity and corresponding abundances considering an hypothetical line with a flux of  $3\sigma$  of the adjacent continuum. The resulting O<sup>+</sup> abundances and the estimated upper limits for the shock components are shown in Table 13.

For C<sup>2+</sup> and Ne<sup>2+</sup>, we adopt the temperature of the high ionization zone for each component of each cut. C II RLs from different transitions were considered to derive C<sup>2+</sup> abundances, as it is shown in Table 13. Multiplet 6 of C II has two lines at 4267.00 and 4267.18 Å resolved at our spectral resolution, as shown in Fig. 12. In general, lines from all multiplets of C II considered give consistent values of C<sup>2+</sup> abundances. RLs from multiplet 1 of Ne II were used to calculate the Ne<sup>2+</sup> abundance. Although they are rather faint lines (see Fig. 13), the Ne<sup>2+</sup> abundances derived from Ne II  $\lambda\lambda$  3694.21 and 3766.26 lines for each component of cut 2 are consistent with each other. In addition, the Ne<sup>2+</sup> abundance we derive for the nebular component in cuts 2 and 3 is in good agreement with that obtained by Esteban et al. (2004) (see their Table 11).

## 6 TEMPERATURE FLUCTUATIONS

Following the procedure described by Peimbert (1967), we define the average temperature as it is shown in Eq. (7) and the mean square temperature fluctuation as in Eq. (8).

$$T_0 = \frac{\int T_e n_e n_i dV}{\int n_e n_i dV}, \quad (7)$$

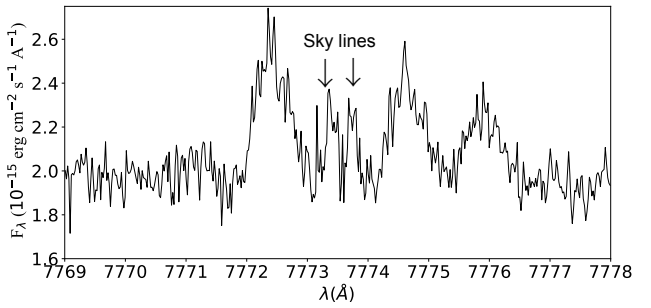


**Figure 11.** Lines of multiplet 1 of O I ( $3s^5S^0$ - $3p^5P$ ) from the spectrum of Cut 2. Due to high spectral resolution, these lines are free of blending with sky emission features.

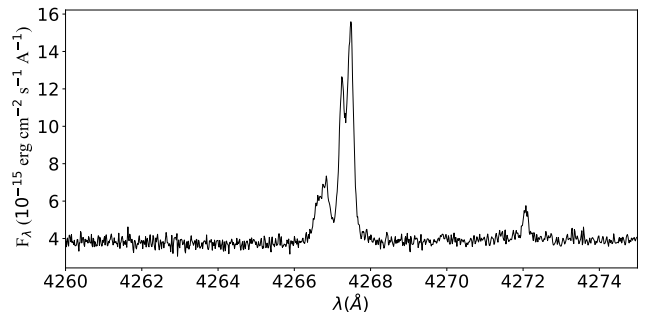


**Figure 12.** Lines of multiplet 6 of C II ( $3d^2D$ - $4f^2F^0$ ) from the spectrum of Cut 2.

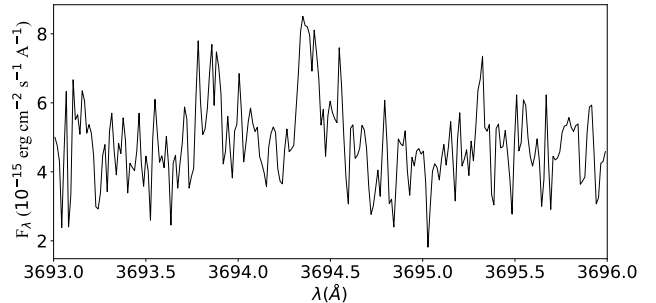


**Figure 13.** Lines of multiplet 1 of Ne II ( $3s^4P$ - $3p^4P^0$ ) from the spectrum of Cut 2.

$$t^2 = \frac{\int (T_e - T_0)^2 n_e n_i dV}{T_0 \int n_e n_i dV}. \quad (8)$$

In the case of a temperature derived from the ratio of two quantities that depend on two different powers of temperature,  $\alpha$  and  $\beta$  respectively, as the case of the temperature derived from RLs or the ratio between the Balmer or Paschen discontinuities and the flux of any other H I line, the measured temperature  $T_{\alpha/\beta}$  depends on  $t^2$  and  $T_0$  as follows:

$$T_{\alpha/\beta} = T_0 \left( 1 - \frac{\alpha + \beta - 1}{2} t^2 \right). \quad (9)$$

On the other hand, two quantities with an individual temperature dependence proportional to  $\frac{e^{kT}}{T^{1/2}}$ , as the intensity of CELs,

Table 12: O<sup>2+</sup> abundances with RLs. J: Esta tabla debe ir en los apéndices

Mult.	Transition	$\lambda_0$	Cut 1	Cut 2		Cut 3		Cut 4	Combined Cuts
			Nebula	Shock	Nebula	Shock	Nebula	Nebula	
1	$3s^4P-3p^4D^0$	4638.86	$8.547 \pm 0.038$	$8.864 \pm 0.029$	$8.546 \pm 0.019$	$8.642^{+0.114}_{-0.113}$	$8.566 \pm 0.067$	$8.519^{+0.031}_{-0.032}$	$8.632 \pm 0.044$
		4641.81	$8.433^{+0.017}_{-0.018}$	$8.772 \pm 0.019$	$8.516^{+0.014}_{-0.013}$	$8.780 \pm 0.027$	$8.502^{+0.014}_{-0.013}$	$8.509^{+0.017}_{-0.018}$	$8.575^{+0.017}_{-0.018}$
		4649.13	$8.473^{+0.024}_{-0.022}$	$8.863^{+0.017}_{-0.016}$	$8.520 \pm 0.011$	$8.876^{+0.037}_{-0.032}$	$8.536 \pm 0.015$	$8.534^{+0.018}_{-0.016}$	$8.589^{+0.016}_{-0.015}$
		4650.84	$8.469^{+0.032}_{-0.031}$	$8.830 \pm 0.030$	$8.509 \pm 0.019$	$8.906 \pm 0.049$	$8.521 \pm 0.023$	$8.558^{+0.029}_{-0.028}$	$8.602 \pm 0.028$
		4661.63	$8.534:$	$8.947^{+0.029}_{-0.028}$	$8.550:$	$8.883^{+0.034}_{-0.036}$	$8.602:$	$8.609:$	$8.672:$
		4673.73	$8.579^{+0.152}_{-0.149}$	$8.953^{+0.125}_{-0.129}$	$8.478^{+0.070}_{-0.069}$	$8.851:$	$8.790^{+0.062}_{-0.060}$	$8.749^{+0.088}_{-0.087}$	$8.730^{+0.099}_{-0.095}$
		4676.23	$8.400^{+0.052}_{-0.053}$	$8.710 \pm 0.048$	$8.475 \pm 0.022$	$8.881^{+0.070}_{-0.068}$	$8.497 \pm 0.026$	$8.507^{+0.031}_{-0.030}$	$8.543^{+0.034}_{-0.035}$
		<b>Average</b>	<b><math>8.465 \pm 0.043</math></b>	<b><math>8.826 \pm 0.060</math></b>	<b><math>8.515 \pm 0.018</math></b>	<b><math>8.826 \pm 0.063</math></b>	<b><math>8.517 \pm 0.033</math></b>	<b><math>8.525 \pm 0.026</math></b>	<b><math>8.584 \pm 0.022</math></b>
		4317.14	$8.498^{+0.052}_{-0.054}$	$9.065^{+0.027}_{-0.026}$	$8.671 \pm 0.022$	-	$8.644^{+0.047}_{-0.048}$	$8.656 \pm 0.035$	$8.723:$
		4345.56	$8.582 \pm 0.057$	$9.160^{+0.043}_{-0.045}$	$8.714 \pm 0.026$	$9.100 \pm 0.074$	$8.659 \pm 0.031$	$8.726 \pm 0.030$	$8.829^{+0.043}_{-0.044}$
2	$3s^4P-3p^4P^0$	4349.43	$8.659 \pm 0.040$	$9.023 \pm 0.022$	$8.678 \pm 0.013$	$9.009^{+0.053}_{-0.052}$	$8.650^{+0.021}_{-0.022}$	$8.715^{+0.026}_{-0.025}$	$8.767 \pm 0.030$
		4366.89	$8.631^{+0.041}_{-0.040}$	$9.203 \pm 0.027$	$8.710 \pm 0.022$	$9.167 \pm 0.056$	$8.672^{+0.030}_{-0.031}$	$8.724^{+0.031}_{-0.030}$	$8.835 \pm 0.030$
		<b>Average</b>	<b><math>8.595 \pm 0.062</math></b>	<b><math>9.076 \pm 0.072</math></b>	<b><math>8.686 \pm 0.016</math></b>	<b><math>9.070 \pm 0.070</math></b>	<b><math>8.656 \pm 0.009</math></b>	<b><math>8.706 \pm 0.027</math></b>	<b><math>8.802 \pm 0.033</math></b>
		4414.90	$8.807^{+0.053}_{-0.051}$	$8.968^{+0.055}_{-0.051}$	$8.754 \pm 0.025$	-	$8.772^{+0.026}_{-0.027}$	$8.689^{+0.053}_{-0.052}$	$8.753^{+0.036}_{-0.035}$
5	$3s^2P-3p^2D^0$	4416.97	$8.622^{+0.069}_{-0.063}$	-	$8.769^{+0.031}_{-0.030}$	-	$8.734 \pm 0.039$	$8.712^{+0.043}_{-0.044}$	$8.680^{+0.036}_{-0.034}$
		<b>Average</b>	<b><math>8.710 \pm 0.093</math></b>	<b><math>8.968^{+0.055}_{-0.051}</math></b>	<b><math>8.760 \pm 0.007</math></b>	-	<b><math>8.759 \pm 0.018</math></b>	<b><math>8.702 \pm 0.011</math></b>	<b><math>8.712 \pm 0.037</math></b>
		4069.62	$8.459^{+0.064}_{-0.060}$	-	$8.246:$	-	$8.352:$	$8.657^{+0.071}_{-0.069}$	$8.299:$
10	$3p^4D^0-3d^4F$	4069.88	$8.352^{+0.050}_{-0.049}$	$8.369:$	$8.297:$	$8.249:$	$8.386:$	$8.412^{+0.096}_{-0.091}$	$8.353:$
		4072.15	$8.449 \pm 0.026$	$8.583 \pm 0.035$	$8.421^{+0.017}_{-0.018}$	$8.719^{+0.062}_{-0.061}$	$8.423^{+0.021}_{-0.022}$	$8.372^{+0.027}_{-0.026}$	$8.467 \pm 0.026$
		4075.86	$8.436 :$	$8.757^{+0.028}_{-0.027}$	-	-	-	$8.407^{+0.030}_{-0.029}$	-
		4078.84	$8.299^{+0.166}_{-0.159}$	$8.911^{+0.093}_{-0.092}$	$8.503^{+0.040}_{-0.039}$	-	$8.787:$	-	-
		4085.11	$8.212 \pm 0.150$	$9.316:$	$8.509 \pm 0.035$	$9.291:$	$8.408 \pm 0.065$	$8.699^{+0.044}_{-0.043}$	$8.810:$
		4092.93	-	$8.490:$	$8.598^{+0.049}_{-0.047}$	$8.517:$	$8.453^{+0.073}_{-0.071}$	$8.627:$	$9.013:$
		<b>Average</b>	<b><math>8.421 \pm 0.048</math></b>	<b><math>8.671 \pm 0.096</math></b>	<b><math>8.450 \pm 0.052</math></b>	<b><math>8.719^{+0.062}_{-0.061}</math></b>	<b><math>8.423 \pm 0.009</math></b>	<b><math>8.413 \pm 0.099</math></b>	<b><math>8.467 \pm 0.026</math></b>
		4590.97	$8.414^{+0.062}_{-0.060}$	$8.632^{+0.072}_{-0.067}$	$8.385^{+0.034}_{-0.033}$	$8.760^{+0.078}_{-0.074}$	$8.387 \pm 0.031$	$8.415 \pm 0.057$	$8.433^{+0.045}_{-0.043}$
15	$3s^2D-3p^2F^0$	4121.46	$8.791:$	-	$8.865 \pm 0.030$	-	$8.806:$	$8.862:$	$8.762:$
		4132.80	$8.451^{+0.069}_{-0.071}$	$8.982^{+0.051}_{-0.053}$	$8.565^{+0.027}_{-0.026}$	$8.940^{+0.152}_{-0.150}$	$8.512 \pm 0.035$	$8.579 \pm 0.044$	$8.651^{+0.053}_{-0.051}$
		<b>Average</b>	<b><math>8.565 \pm 0.079</math></b>	<b><math>8.977 \pm 0.003</math></b>	<b><math>8.616 \pm 0.093</math></b>	<b><math>8.870 \pm 0.025</math></b>	<b><math>8.568 \pm 0.044</math></b>	<b><math>8.603 \pm 0.022</math></b>	<b><math>8.701 \pm 0.034</math></b>
20	$3p^4P^0-3d^4D$	4104.99	-	$8.801:$	$8.363^{+0.126}_{-0.123}$	-	$8.458^{+0.102}_{-0.098}$	$8.494 \pm 0.097$	-
		4110.79	$8.811:$	$9.627:$	$8.805:$	$9.215:$	$8.766:$	$9.250:$	$9.030:$
		4119.22	$8.563^{+0.049}_{-0.048}$	$8.875^{+0.061}_{-0.059}$	$8.626^{+0.023}_{-0.022}$	-	$8.475^{+0.072}_{-0.074}$	$8.722^{+0.036}_{-0.034}$	$8.605^{+0.044}_{-0.043}$
		<b>Average</b>	<b><math>8.563^{+0.049}_{-0.048}</math></b>	<b><math>8.875^{+0.061}_{-0.059}</math></b>	<b><math>8.626 \pm 0.087</math></b>	<b><math>9.215 :</math></b>	<b><math>8.469 \pm 0.008</math></b>	<b><math>8.674 \pm 0.087</math></b>	<b><math>8.605^{+0.044}_{-0.043}</math></b>
		4185.44	$8.095^{+0.062}_{-0.061}$	$8.113^{+0.117}_{-0.112}$	$7.971^{+0.045}_{-0.043}$	$8.519:$	$8.079^{+0.065}_{-0.066}$	$8.108^{+0.071}_{-0.070}$	$8.074^{+0.092}_{-0.088}$
		4189.79	$8.344^{+0.047}_{-0.044}$	$8.697^{+0.056}_{-0.052}$	$8.307^{+0.031}_{-0.029}$	$8.912^{+0.125}_{-0.122}$	$8.329^{+0.071}_{-0.070}$	$8.380^{+0.055}_{-0.052}$	$8.418^{+0.062}_{-0.063}$
3d-4f	$3p^2F^0-3d^2G$	<b>Average</b>	<b><math>8.200 \pm 0.128</math></b>	<b><math>8.327 \pm 0.314</math></b>	<b><math>8.107 \pm 0.172</math></b>	<b><math>8.912^{+0.125}_{-0.122}</math></b>	<b><math>8.146 \pm 0.119</math></b>	<b><math>8.217 \pm 0.138</math></b>	<b><math>8.211 \pm 0.176</math></b>
		4087.15	$8.588 \pm 0.092$	$8.807^{+0.120}_{-0.118}$	$8.644^{+0.065}_{-0.067}$	$9.050 \pm 0.097$	$8.431^{+0.057}_{-0.056}$	$8.526^{+0.096}_{-0.095}$	$8.651 \pm 0.082$
		4089.29	$8.451^{+0.058}_{-0.057}$	$9.036:$	$8.518^{+0.032}_{-0.030}$	$8.852:$	$8.422^{+0.028}_{-0.027}$	$8.412^{+0.051}_{-0.048}$	$8.555 \pm 0.036$
		4095.64	-	$8.762^{+0.107}_{-0.101}$	$8.499^{+0.054}_{-0.053}$	$9.269:$	$8.545:$	-	-
		4097.26	$8.547^{+0.059}_{-0.056}$	-	$8.551^{+0.029}_{-0.028}$	-	$8.577 \pm 0.031$	$8.592^{+0.039}_{-0.040}$	$8.497^{+0.036}_{-0.035}$
		4275.55	$8.464^{+0.070}_{-0.068}$	$8.752^{+0.119}_{-0.112}$	$8.520^{+0.046}_{-0.047}$	-	$8.475^{+0.053}_{-0.052}$	$8.554^{+0.063}_{-0.060}$	$8.497^{+0.062}_{-0.061}$
		<b>Average</b>	<b><math>8.494 \pm 0.052</math></b>	<b><math>8.771 \pm 0.023</math></b>	<b><math>8.534 \pm 0.032</math></b>	<b><math>9.050 \pm 0.097</math></b>	<b><math>8.468 \pm 0.067</math></b>	<b><math>8.507 \pm 0.081</math></b>	<b><math>8.525 \pm 0.041</math></b>
Mult. 1, 2, 10, 20 and 3d-4f transitions		Average	$8.465 \pm 0.072$	$8.827 \pm 0.160$	$8.539 \pm 0.084$	$8.841 \pm 0.111$	$8.512 \pm 0.075$	$8.523 \pm 0.108$	$8.541 \pm 0.137$

**Table 13.** O<sup>+</sup>, C<sup>2+</sup> and Ne<sup>2+</sup> abundances based on RLs.

Mult.	Transition	$\lambda_0$	Cut 1 Nebula	Cut 2 Shock	Cut 3 Nebula	Cut 4 Shock	Nebula	Combined Cuts
O <sup>+</sup>								
1	3s <sup>5</sup> S <sup>0</sup> -3p <sup>5</sup> P	7771.94 7774.17 7775.39	8.344 ± 0.100	<7.91	8.250 ± 0.064	<7.87	8.275 ± 0.073	8.274 <sup>+0.068</sup> <sub>-0.069</sub> 8.187 ± 0.073
C <sup>2+</sup>								
6	3d <sup>2</sup> D-4f <sup>2</sup> F <sup>0</sup>	4267.00 4267.18 4267.26	8.349 <sup>+0.030</sup> <sub>-0.031</sub>	8.457 <sup>+0.025</sup> <sub>-0.026</sub>	8.347 ± 0.017	8.557 ± 0.026	8.339 ± 0.013	8.328 <sup>+0.021</sup> <sub>-0.022</sub> 8.371 ± 0.026
16.04	4d <sup>2</sup> D-6f <sup>2</sup> F <sup>0</sup>	6151.27 6151.53	-	9.058:	8.376:	-	8.441 ± 0.120	- -
17.02	4f <sup>2</sup> F <sup>0</sup> -5g <sup>2</sup> G	9903.46 9903.89	8.326 <sup>+0.043</sup> <sub>-0.045</sub>	8.467 ± 0.066	8.363 ± 0.035	8.630 ± 0.132	8.301 <sup>+0.057</sup> <sub>-0.056</sub> 8.353 <sup>+0.043</sup> <sub>-0.042</sub>	8.377 <sup>+0.057</sup> <sub>-0.056</sub>
17.04	4f <sup>2</sup> F <sup>0</sup> -6g <sup>2</sup> G	6461.95 6462.13	8.354 ± 0.091	8.701:	8.298 ± 0.065	-	8.318 ± 0.060	8.351 ± 0.071 8.353 <sup>+0.118</sup> <sub>-0.116</sub>
17.06	4f <sup>2</sup> F <sup>0</sup> -7g <sup>2</sup> G	5342.38 5342.50	8.619:	-	8.449 <sup>+0.059</sup> <sub>-0.060</sub>	-	8.502 <sup>+0.064</sup> <sub>-0.065</sub>	- -
	<b>Adopted</b>	<b>8.342 ± 0.030</b>	<b>8.458 ± 0.025</b>	<b>8.351 ± 0.025</b>	<b>8.560 ± 0.026</b>	<b>8.340 ± 0.029</b>	<b>8.334 ± 0.022</b>	<b>8.371 ± 0.026</b>
Ne <sup>2+</sup>								
1	3s <sup>4</sup> P-3p <sup>4</sup> P <sup>0</sup>	3694.21 3766.26	-	8.637 <sup>+0.073</sup> <sub>-0.072</sub>	8.095 <sup>+0.063</sup> <sub>-0.065</sub>	-	8.315:	- -
	<b>Adopted</b>	-	<b>8.603 ± 0.050</b>	<b>8.072 ± 0.029</b>	-	<b>8.036 ± 0.153</b> <sub>-0.150</sub>	-	<b>8.036 ± 0.150</b>

will produce a line intensity ratio with a temperature dependence on  $e^{\frac{\Delta E_2 - \Delta E_1}{kT} \frac{1}{\lambda_1/\lambda_2}}$ . We can derive the temperature  $T_{\lambda_1/\lambda_2}$ :

$$T_{\lambda_1/\lambda_2} = T_0 \left[ 1 + \left( \frac{\Delta E_1 + \Delta E_2}{kT_0} - 3 \right) \frac{t^2}{2} \right] \quad (10)$$

When  $\alpha$  and  $\beta$  in Eq. (9) are negative, the low-temperature zones within the line of sight will have a larger weight on  $T_{\alpha/\beta}$ , while in the cases where  $\frac{\Delta E_1 + \Delta E_2}{kT_0}$  is larger than 3, the contribution of the high-temperature zones will be more important (Peimbert 1967).

On the basis of Eq. (9) and the estimations of the  $\alpha$  and  $\beta$  coefficients given by Peimbert & Costero (1969) and Zhang et al. (2005), for the H I and He I temperature, respectively, we have Eq. (11) and Eq. (12).

$$T_{BJ/H11} = T_0 \left( 1 - 1.67t^2 \right), \quad (11)$$

$$T_{7281/6678} = T_0 \left( 1 - 1.07t^2 \right). \quad (12)$$

On the other hand, for estimations of temperatures based on intensity ratios of CELs, we have Eq. (13), Eq. (14) and Eq. (15).

$$T_{4363/4959+5007} = T_0 \left[ 1 + \left( \frac{91300}{T_0} - 3 \right) \frac{t^2}{2} \right], \quad (13)$$

$$T_{6312/9069+9531} = T_0 \left[ 1 + \left( \frac{54000}{T_0} - 3 \right) \frac{t^2}{2} \right], \quad (14)$$

$$T_{5755/6584} = T_0 \left[ 1 + \left( \frac{68950}{T_0} - 3 \right) \frac{t^2}{2} \right]. \quad (15)$$

We have applied the combination of Eq. (11) and Eq. (13) using T(H I) and T([O III]) to estimate  $t^2$  (Peimbert 2003; Esteban et al. 2004; García-Rojas et al. 2004, 2005, 2007). Implicitly, this assumes that  $t^2(\text{H}^+) \approx t^2(\text{O}^{2+})$  and  $T_0(\text{H}^+) \approx T_0(\text{O}^{2+})$ . The same procedure has been used with Eq. (14) and Eq. (15) (Peimbert & Costero 1969; Esteban et al. 1998) in order to estimate representative values of  $t^2$  for different ionization zones. In Table (14), we show the  $t^2$  and  $T_0$  values obtained for each combination of the temperature indicators in the spectrum of the combined cuts, the only one where all the different temperature indicators are available. We have to emphasize the excellent agreement between the results obtained by combining  $T(\text{H I})$  and the  $T_e$  diagnostics based on CELs ratios with what it is obtained using  $T(\text{He I})$ .

However, the above procedure may not be entirely accurate. From equations (7) and (8), it is clear that the values of  $t^2$  and  $T_0$  depend on the integrated volume. Thus, since each ion  $X^{i+}$  will have its own Strömgren sphere, each one will have a representative  $t^2(X^{i+})$  and  $T_0(X^{i+})$ . Considering another ion,  $Y^{i+}$ , the assumption  $t^2(X^{i+}) \approx t^2(Y^{i+})$  will be only correct if  $X^{i+}$  and  $Y^{i+}$  occupy the same nebular volume. In the case of  $\text{H}^+$  and  $\text{O}^{2+}$ , if there is an appreciable amount of O in other states apart of  $\text{O}^{2+}$ , the value of  $t^2(\text{H}^+)$  may differ from  $t^2(\text{O}^{2+})$ . Based on a set of Cloudy photoionization models with different input parameters, Kingdon & Ferland (1995) derived  $t^2$  in two manners: as  $t_{\text{str}}^2$  from the formal definition of Eq. (8) and the  $t_{\text{obs}}^2$  obtained from the comparison of equations (11) and (13). They found that generally  $t_{\text{str}}^2 \neq t_{\text{obs}}^2$ , with the difference increasing with the  $T_{\text{eff}}$  of the ionizing sources. However, for the  $T_{\text{eff}}$  typical of the ionizing stars of H II regions (between 30,000 and 50,000 k), the approximation  $t_{\text{str}}^2 \approx t_{\text{obs}}^2$  seems to be valid. The main drawback one faces in determining  $t_{\text{obs}}^2$  is its high

**Table 14.**  $t^2$  and  $T_0$  derived from the different combinations of Eq. (11) and Eq. (12) with Eq. (13), Eq. (14) and Eq. (15) for the spectra of all cuts combined.

	T([O III])		T([S III])		T([N II])	
	$t^2$	$T_0$	$t^2$	$T_0$	$t^2$	$T_0$
T(H I)	$0.020 \pm 0.017$	$7770 \pm 850$	$0.051 \pm 0.030$	$8240 \pm 980$	$0.068 \pm 0.023$	$8510 \pm 960$
T(He I)	$0.018 \pm 0.012$	$7840 \pm 520$	$0.054 \pm 0.024$	$8160 \pm 570$	$0.075 \pm 0.018$	$8360 \pm 570$

intrinsic uncertainty. As we discussed in § 4.4, the determination of temperature based on the Balmer or Paschen discontinuities is very sensitive to the noise level of the nebular continuum around the position of the discontinuities. Even with the procedure followed in this work, fitting the continuum at both sides of the discontinuities several times up to a statistically representative number of tests, the inherent dispersion in the resulting temperature is larger than what is obtained from diagnostics based on CEL ratios. The sources of uncertainty in  $T(\text{He I})$  are slightly smaller, but they are still important. Uncertainties on  $T_e$  of a similar order are expected when using Eq. (9). Assuming the two ionization zones scheme for H II regions, a better approximation to  $t^2$  can be obtained using equations (16) and (17), proposed by Peimbert et al. (2002).

$$\gamma = \frac{\int n_e (\text{O}^+) dV}{\int n_e n (\text{O}^+) dV + \int n_e n (\text{O}^{2+}) dV}, \quad (16)$$

$$T_0(\text{H}^+) = \gamma T_0(\text{O}^+) + (1 - \gamma) T_0(\text{O}^{2+}). \quad (17)$$

To use Eq. (17), we need to estimate the fraction of the total O in  $\text{O}^+$  form. For the spectrum of the combined cuts,  $\gamma$  varies from 0.36 to 0.23 according to whether the abundances are determined from RLs or CELs, respectively. A reasonable approximation is to take the average value  $\gamma \approx 0.3$ . On the other hand,  $\text{He}^+$  should be present in both, the  $\text{O}^+$  and  $\text{O}^{2+}$  zones. Although there may be coexistence of  $\text{He}^0$  and  $\text{H}^+$ , the volume that  $\text{He}^0$  occupies should be small at the ionization conditions of the Orion Nebula and it can be assumed that the volume containing  $\text{H}^+$  and  $\text{He}^+$  should be approximately the same. This assumption is reinforced by the fact that the parameter  $\eta = (\text{O}^+/\text{O}^{2+})(\text{S}^{2+}/\text{S}^+)$  (Vilchez & Pagel 1988), which is a measure of the radiation hardness and is correlated with the  $T_{\text{eff}}$  of the ionizing source, has a value of  $\log(\eta) = 0.74$  for the combined cuts spectrum. Pagel et al. (1992) showed that for  $\log(\eta) < 0.9$ , the amount of  $\text{He}^0$  is negligible for a large variety of photoionization models. Therefore, we can assume  $T_0(\text{H}^+) \approx T_0(\text{He}^+)$  and  $t^2(\text{H}^+) \approx t^2(\text{He}^+)$ . Based on the previous discussion, we combined Eq. (11) and Eq. (12) for the combined cuts spectrum, obtaining  $t^2(\text{H}^+) \approx 0.036$  and  $T_0(\text{H}^+) \approx 8000$  K. Using these values in Eq. (17) and assuming that the volume occupied by  $\text{O}^+$  and  $\text{N}^+$  is the same, and that, at first order,  $\frac{T_0(\text{[OIII]})}{T_0(\text{[NII]})} \approx \frac{T_0(\text{O}^{2+})}{T_0(\text{N}^+)} \approx 0.85$ , we obtain  $T_0(\text{O}^{2+}) \approx 7580$  and  $T_0(\text{N}^+) \approx 8950$ . Then, from Eq. (13) and Eq. (15), we estimate  $t_{\text{high}}^2 = t^2(\text{O}^{2+}) \approx 0.025$  and  $t_{\text{low}}^2 = t^2(\text{N}^+) \approx 0.050$ .

The remarkably good agreement between the values obtained with Eq. (17) and those presented in Table 14 reinforces the suitability of the temperature fluctuations paradigm to describe the results. Considering the numerical values obtained for the combined

cuts spectrum, we adopt the average values  $t_{\text{high}}^2 = 0.021 \pm 0.003$ ,  $t_{\text{inter}}^2 = 0.051 \pm 0.009$  and  $t_{\text{low}}^2 = 0.064 \pm 0.011$ , where the uncertainties correspond to the standard deviation of the average. Unfortunately,  $T(\text{H I})$  based on the Balmer discontinuity can not be calculated for the individual components of the different cuts, and the estimations of  $t^2$  must rely exclusively on the calculated  $T(\text{He I})$ . However, calculations following the same procedure as the previously described to obtain the values presented in Table 14 for the individual components of each cut show similar results. These values are presented in Table A6, indicating that the values adopted for the combined cuts spectrum are also representative for the other components of each cut.

Using Eq. (15), Eq. (14) and Eq. (13) with the adopted  $t^2$  values for each ionization zone,  $T_0$  is estimated in each case for all components. Following the same scheme described in § 5.1, we estimate the ionic abundances within the the paradigm of temperature inhomogeneities and results are shown in Table 15.

## 7 THE ABUNDANCE DISCREPANCY FACTOR

A major problem in the analysis of photoionized regions is the discrepancy between the chemical abundances derived from RLs and CELs, known as the abundance discrepancy (AD) problem. The relatively weak RLs, give systematically higher abundances than CELs. This difference is commonly quantified through the abundance discrepancy factor (ADF, Liu et al. 2000), defined here as:

$$\text{ADF} (X^i) = \log \left( \frac{n(X^i)_{\text{RLs}}}{n(X^i)_{\text{CEls}}} \right). \quad (18)$$

There is an extensive collection of works dedicated to this problem in the literature (see Torres-Peimbert et al. 1980; Liu et al. 2001; Stasińska et al. 2007; Tsamis et al. 2011; Nicholls et al. 2012, and references therein). Although there is no definitive solution, there are several hypotheses to explain the AD. For example, temperature fluctuations (see §6), which would primarily affect abundances based on CELs, underestimating the real values; semi-ionized gas clumps, overestimating abundances based on RLs and underestimating those of CELs; chemical inhomogeneities with different physical conditions, affecting both estimates depending on each specific case and so on. It is even possible that the AD is the result of the sum of various phenomena affecting each nebula in a different degree. Using a set of deep spectra of Galactic H II regions, García-Rojas & Esteban (2007) found that the ADF is fairly constant around a factor 2, showing no trend with ionization degree,  $T_e$  or the effective temperature of the ionizing stars. They found that temperature fluctuations is the most likely explanation for the AD in H II regions.

In Table 16, we present the ADF obtained from  $\text{O}^+$ ,  $\text{O}^{2+}$ ,  $\text{Ne}^{2+}$  and  $\text{C}^{2+}$  abundances determined from RLs and CELs for each

**Table 15.** Chemical abundances based on CEL's derived within the paradigm of temperature inhomogeneities ( $t^2 > 0$ ).

Ion	Cut 1	Cut 2		Cut 3		Cut 4	Combined cuts
	Nebula	Shock	Nebula	Shock	Nebula	Nebula	
O <sup>+</sup>	8.18 <sup>+0.10</sup> <sub>-0.08</sub>	7.45 <sup>+0.20</sup> <sub>-0.12</sub>	8.14 <sup>+0.12</sup> <sub>-0.09</sub>	7.31 <sup>+0.20</sup> <sub>-0.12</sub>	8.05 <sup>+0.13</sup> <sub>-0.09</sub>	8.12 <sup>+0.13</sup> <sub>-0.09</sub>	8.05 <sup>+0.11</sup> <sub>-0.08</sub>
O <sup>2+</sup>	8.48 <sup>+0.06</sup> <sub>-0.05</sub>	8.70 ± 0.04	8.50 <sup>+0.05</sup> <sub>-0.04</sub>	8.59 <sup>+0.04</sup> <sub>-0.03</sub>	8.51 ± 0.04	8.52 <sup>+0.05</sup> <sub>-0.04</sub>	8.53 <sup>+0.05</sup> <sub>-0.04</sub>
N <sup>+</sup>	7.18 <sup>+0.05</sup> <sub>-0.04</sub>	6.28 <sup>+0.11</sup> <sub>-0.08</sub>	7.17 <sup>+0.07</sup> <sub>-0.05</sub>	6.39 <sup>+0.11</sup> <sub>-0.08</sub>	7.09 <sup>+0.07</sup> <sub>-0.05</sub>	7.16 <sup>+0.07</sup> <sub>-0.06</sub>	7.07 <sup>+0.06</sup> <sub>-0.05</sub>
Ne <sup>2+</sup>	7.86 <sup>+0.07</sup> <sub>-0.06</sub>	8.10 <sup>+0.05</sup> <sub>-0.04</sub>	7.89 <sup>+0.06</sup> <sub>-0.05</sub>	7.94 ± 0.04	7.91 <sup>+0.05</sup> <sub>-0.04</sub>	7.94 <sup>+0.06</sup> <sub>-0.05</sub>	7.93 <sup>+0.06</sup> <sub>-0.05</sub>
S <sup>+</sup>	5.75 <sup>+0.07</sup> <sub>-0.06</sub>	4.86 <sup>+0.13</sup> <sub>-0.09</sub>	5.75 <sup>+0.07</sup> <sub>-0.06</sub>	4.95 <sup>+0.12</sup> <sub>-0.08</sub>	5.70 <sup>+0.08</sup> <sub>-0.07</sub>	5.77 <sup>+0.08</sup> <sub>-0.06</sub>	5.66 <sup>+0.07</sup> <sub>-0.06</sub>
S <sup>2+</sup>	6.87 <sup>+0.05</sup> <sub>-0.04</sub>	7.01 <sup>+0.06</sup> <sub>-0.05</sub>	6.94 <sup>+0.06</sup> <sub>-0.05</sub>	6.94 <sup>+0.07</sup> <sub>-0.06</sub>	6.95 <sup>+0.06</sup> <sub>-0.05</sub>	6.91 ± 0.05	6.94 ± 0.05
Cl <sup>+</sup>	3.87 ± 0.05	3.04 <sup>+0.16</sup> <sub>-0.14</sub>	3.86 <sup>+0.06</sup> <sub>-0.05</sub>	<3.13	3.81 <sup>+0.06</sup> <sub>-0.05</sub>	3.90 <sup>+0.07</sup> <sub>-0.06</sub>	3.76 <sup>+0.06</sup> <sub>-0.05</sub>
Cl <sup>2+</sup>	5.00 <sup>+0.07</sup> <sub>-0.06</sub>	5.15 <sup>+0.09</sup> <sub>-0.06</sub>	5.06 <sup>+0.08</sup> <sub>-0.06</sub>	5.06 <sup>+0.10</sup> <sub>-0.07</sub>	5.09 <sup>+0.08</sup> <sub>-0.06</sub>	5.08 <sup>+0.08</sup> <sub>-0.06</sub>	5.07 <sup>+0.07</sup> <sub>-0.06</sub>
Cl <sup>3+</sup>	3.30 ± 0.06	3.71 ± 0.05	3.38 ± 0.04	3.48 <sup>+0.10</sup> <sub>-0.11</sub>	3.43 ± 0.04	3.55 <sup>+0.05</sup> <sub>-0.04</sub>	3.48 <sup>+0.06</sup> <sub>-0.05</sub>
Ar <sup>2+</sup>	6.42 ± 0.04	6.50 ± 0.03	6.42 <sup>+0.04</sup> <sub>-0.03</sub>	6.44 ± 0.03	6.43 ± 0.03	6.40 <sup>+0.04</sup> <sub>-0.03</sub>	6.43 <sup>+0.04</sup> <sub>-0.03</sub>
Ar <sup>3+</sup>	4.55 <sup>+0.07</sup> <sub>-0.06</sub>	4.91 <sup>+0.06</sup> <sub>-0.05</sub>	4.63 <sup>+0.06</sup> <sub>-0.05</sub>	4.71 <sup>+0.16</sup> <sub>-0.15</sub>	4.66 <sup>+0.05</sup> <sub>-0.04</sub>	4.79 <sup>+0.06</sup> <sub>-0.05</sub>	4.69 <sup>+0.06</sup> <sub>-0.05</sub>
Fe <sup>2+*</sup>	5.93 ± 0.02	6.10 ± 0.05	5.97 ± 0.02	5.88 ± 0.05	5.94 ± 0.02	5.92 ± 0.03	5.96 ± 0.01
Fe <sup>2+**</sup>	5.75 ± 0.02	5.76 ± 0.07	5.81 ± 0.02	5.41 ± 0.06	5.75 ± 0.02	5.72 ± 0.03	5.76 ± 0.02
Fe <sup>3+</sup>	5.99 <sup>+0.16</sup> <sub>-0.12</sub>	6.55 <sup>+0.13</sup> <sub>-0.11</sub>	6.00 <sup>+0.12</sup> <sub>-0.09</sub>	<6.78	6.23 <sup>+0.18</sup> <sub>-0.16</sub>	6.05 <sup>+0.16</sup> <sub>-0.13</sub>	6.16 <sup>+0.18</sup> <sub>-0.15</sub>
Ni <sup>2+</sup>	4.52 ± 0.19	4.62 ± 0.14	4.51 ± 0.18	4.17 ± 0.12	4.48 ± 0.16	4.51 ± 0.13	4.54 ± 0.11

\* indicates that  $T_e$  (high) was used.

\*\* indicates that  $T_e$  (low) was used.

component. The abundances based on CELs do not consider temperature fluctuations. In the case of C<sup>2+</sup>, the value of the abundance from CELs have been taken from the UV observations reported by Walter et al. (1992). We have considered the mean value of their positions number 5 and 7, which are the nearest to our slit and give  $12+\log(C^{2+}/H^+) = 7.835$ . We do not estimate the ADF(C<sup>2+</sup>) for the high-velocity component since the UV CELs values can only be compared with the nebular component. It is a common procedure to estimate  $t^2$  by looking for a temperature  $T_0$  that produces the agreement between the abundance determined from CELs and RLs, but this is only valid if the temperature fluctuations are the cause of AD. We remark that we do not use this procedure in this work, since this hypothesis might not be the only valid for the high velocity components. Our determinations of  $t^2$  are exclusively those described in §6. Therefore  $t^2 > 0$ , does not necessarily mean ADF = 0, unless the measured value of  $t^2$  is compatible with this.

From Table 16, is remarkable that the ADF is slightly different for each ion and higher in the high-velocity components. Using the value of  $t^2$  adopted for each ionization zone of the nebular components (see Table 15), we obtain abundances based on CELs consistent with those determined from RLs and, therefore, making the ADF consistent with zero within the uncertainties. This suggests that the temperature fluctuation paradigm is capable of explaining the slight difference between the ADF in O<sup>+</sup> and O<sup>2+</sup>. However, considering the high velocity components, the ionic abundances determined from CELs assuming the  $t^2$  values given in Table A6 give values of the ADF smaller but they do not cancel it. For example, in the case of the high-velocity component of cut 3, the ADF(O<sup>2+</sup>) goes from 0.39 to 0.24 when considering  $t^2 = 0.021$ . This suggests the presence of another effect apart the classic description of temperature inhomogeneities.

## 8 TOTAL ABUNDANCES

We have to use ionization correction factors (ICFs) to estimate the contribution of the unseen ions in the total abundance of some elements for some studied components. For N, Ne, S and Ar we use the ICFs proposed by Amayo et al. (2020). In the case of Ni, we use the ICF derived by Delgado-Inglada et al. (2016). For the helium abundance we explore the ICF of Kunth & Sargent (1983). In all cases, we propagate all sources of uncertainty involved in calculating the total abundance of each element, including those related to the ICF. Amayo et al. (2020) give expressions for estimating the uncertainty of each ICF. We have also considered the contribution of the error in the ratio of O<sup>+</sup> and O<sup>2+</sup> abundances, the parameter on which the ICFs depend. Results of total abundances based on CELs are presented in Table 17 and in Table 18, for the case of  $t^2 = 0$  and  $t^2 > 0$ , respectively. Total abundances based in RLs are presented in Table 19. In this case, we do not expect significant changes in the total abundances within the temperature fluctuation paradigm due to the low dependence on temperature of RLs.

### 8.1 Total abundance of Fe

Considering the absence of HeII lines in our spectra, the number of photons with energies greater than 54 eV can be considered negligible. Thus, we do not expect to have Fe<sup>4+</sup> in the nebula and therefore  $\text{Fe/H} = \text{Fe}^+/H^+ + \text{Fe}^{2+}/H^+ + \text{Fe}^{3+}/H^+$ . We have determined the abundance of Fe<sup>2+</sup> and Fe<sup>3+</sup> (or at least an upper limit) for all the components of each cut. So, we only lack the Fe<sup>+</sup> abundance to obtain the total Fe/H ratio. In the high velocity components, the absence of usually relatively intense [Fe II] lines as  $\lambda\lambda 4287, 5158$  and 5262, together with the high ionization degree of the gas, are indicative of a negligible contribution of Fe<sup>+</sup> to the total abundance. Thus, in these cases we have considered  $\text{Fe/H} = \text{Fe}^{2+}/H^+ + \text{Fe}^{3+}/H^+$ . In the nebular components, although a large number of [Fe II] lines have

**Table 16.** Abundance discrepancy factor (ADF) for different ions in the components of each cut.

Cut	Component	ADF(O <sup>+</sup> )	ADF(O <sup>2+</sup> )	ADF(Ne <sup>2+</sup> )	ADF(C <sup>2+</sup> ) <sup>*</sup>
1	Nebular	0.46 ± 0.14	0.15 ± 0.07	-	0.51 ± 0.03
2	High Velocity	<0.80	0.29 ± 0.08	0.70 ± 0.08	-
2	Nebular	0.42 ± 0.12	0.17 ± 0.05	0.37 ± 0.04	0.52 ± 0.03
3	High Velocity	<0.82	0.39 ± 0.08	-	-
3	Nebular	0.52 ± 0.14	0.17 ± 0.06	0.31 ± 0.15	0.51 ± 0.03
4	Nebular	0.46 ± 0.14	0.17 ± 0.06	-	0.50 ± 0.02
Combined cuts		0.44 ± 0.12	0.21 ± 0.05	-	0.54 ± 0.03

\* We adopt  $12 + \log(C^{2+}/H^+) = 7.835$  from UV CELs considering the slit positions 5 and 7 of [Walter et al. \(1992\)](#).

been detected, their emission is mainly produced by fluorescence ([Rodríguez 1999](#); [Verner et al. 2000](#)). Therefore, most of the observed lines will not provide reliable estimates of Fe<sup>+</sup> abundance. Unfortunately, [Fe II]  $\lambda 8617$ , a line almost insensitive to fluorescence ([Lucy 1995](#); [Baldwin et al. 1996](#)) can not be observed due to the physical gap of the CCDs in the Red Arm of UVES. However, previous studies with direct estimations of Fe<sup>+</sup> in the Orion Nebula as [Rodríguez \(2002\)](#) or [Mesa-Delgado et al. \(2009\)](#), obtain Fe<sup>+/Fe<sup>+2</sup> ratios between 0.05 and 0.27. Considering the approximation  $Fe/H = Fe^{2+}/H^+ + Fe^{3+}/H^+$ , the neglected Fe<sup>+/H<sup>+</sup> ratio would contribute to Fe/H up to 0.06 dex in the worst case (calculating Fe<sup>+/H<sup>+</sup> with  $T_e$ (high) and assuming  $Fe^{+}/Fe^{+2} = 0.27$ ). This maximum increase is within the range of uncertainties associated with the sum of Fe<sup>2+</sup> and Fe<sup>3+</sup> abundances and therefore, it seems reasonable to consider  $Fe/H \approx Fe^{2+}/H^+ + Fe^{3+}/H^+$  for the nebular component as well. [Rodríguez & Rubin \(2005\)](#) proposed two ICFs for Fe, one when Fe<sup>2+</sup> and Fe<sup>3+</sup> abundances are available and the other when only Fe<sup>+/H<sup>+</sup> is known. However, the values obtained using both ICFs are discrepant, perhaps due to errors in the atomic data of the ions involved, and the true total Fe abundance is expected to be in between the values obtained from both ICFs ([Rodríguez & Rubin 2005](#)). We have not used this ICF in our analysis.</sup></sup></sup></sup>

As it is shown in Table 17 and Table 18, the abundance of Fe is higher in the high-velocity components, compared with the nebular components. This increase is independent of whether the temperature  $T_e$ (low) or  $T_e$ (high) is taken to derive Fe<sup>2+</sup>. The physical conditions derived in § 4.2 indicate a greater similarity between the  $T_e$ ([Fe III]) and  $T_e$ (high), contrary to what the similarity between the ionization potential of Fe<sup>2+</sup> and N<sup>+</sup> (a representative ion of low ionization degree zone) could indicate. This suggests that the relationships between temperatures are complex. Considering that much of the Fe is depleted in dust grains, an important process that can condition the density and temperature derived from [Fe III] lines are the dust destruction processes.

## 8.2 Total abundances with RLs

In the case of the total abundances derived with RLs, the values of the ICFs were estimated using the O<sup>+</sup> and O<sup>2+</sup> abundances from RLs. In the high-velocity components, since the contribution of O<sup>+</sup> to the total abundance is rather small, the ICF values are close to 1, even considering the upper limit to O<sup>+</sup>, presented in Table 13.

Thus, in these components we took ICF=1. C: Esto queda muy raro, pues no queda claro que icf tomas = 1. Supongo que sera para C, Ne y He, deberiamos decir que ICFs usariamos y que usando dichos ICFs con el cociente O++/O+ que medimos con = 1.

A case that deserves emphasis is the total abundance of He. Based on photoionization models of planetary nebulae, [Delgado-Inglada et al. \(2014\)](#) suggest that the classical ICF schemes for helium are not applicable since the total abundance of He<sup>0</sup> strongly depends on the  $T_{eff}$  of the ionizing source. However, the use of the scheme of [Kunth & Sargent \(1983\)](#) reproduces well in the nebular components the values obtained in the high-velocity components where ICF = 1 has been used. Considering the high degree of ionization, the absence of an ionization front and emission of lines of neutral elements and a hardness radiation of  $\log(\eta) < 0.9$ , it is likely that the He<sup>+</sup> abundance in the high velocity components is close to the total abundance of He, which has to be the same for M42. This traditional ICF scheme has been chosen primarily because it is based on ionic abundances of O, which have been measured with RLs. C: Este parrafo del He hay que reescribirlo. La cita de Delgado Ingla da hay que quitarla, es para PNe y ya de entrada puede hacer dudar de cualquier cosa que digamos detras. Creo que hay que dar los argumentos para corroborar que el ICF = 1 en esta componente. Creo que se puede comentar que con los ICFs que usamos en el paper del Helio obtenemos valores cercanos a 1 y lo del log(eta)<0.9 (dar el numero que obtenemos en este caso). Finalmente hay que hacer hincapié que esta es la mejor estimacion del He total en la Nebulosa de Orion y posiblemente en una region HII galáctica.

## 9 KINEMATICAL ANALYSIS

We calculate the heliocentric velocity of each line comparing its observed wavelength (after applying the heliocentric correction) with its theoretical wavelength in air. All the theoretical values have been taken from the Atomic Line List v2.05b21 ([Van Hoof 2018](#)). Wavelengths from this compilation list are mainly calculated from the theoretical energy difference between the levels connected by the transition. The exception are the hydrogenic lines, which include a weighted average of all the fine structure components. We detect some relevant inaccuracies in the theoretical wavelengths of [Cl III], [Cl IV] and [Ne III] in the Atomic Line List v2.05b21. This

**Table 17.** Total abundances based on CELs with  $t^2 = 0.0$ .

Element	Cut 1	Cut 2		Cut 3		Cut 4	Combined cuts
	Nebula	Shock	Nebula	Shock	Nebula	Nebula	
O	$8.45 \pm 0.03$	$8.56 \pm 0.02$	$8.46 \pm 0.03$	$8.46 \pm 0.02$	$8.45 \pm 0.03$	$8.47 \pm 0.03$	$8.46 \pm 0.03$
N	$7.66^{+0.16}_{-0.15}$	$7.53^{+0.28}_{-0.22}$	$7.71^{+0.18}_{-0.16}$	$7.67^{+0.29}_{-0.22}$	$7.68^{+0.19}_{-0.16}$	$7.72^{+0.18}_{-0.16}$	$7.68 \pm 0.17$
Ne	$7.85^{+0.13}_{-0.12}$	$7.93^{+0.06}_{-0.05}$	$7.85^{+0.11}_{-0.10}$	$7.80^{+0.06}_{-0.05}$	$7.86^{+0.11}_{-0.09}$	$7.89^{+0.12}_{-0.10}$	$7.85^{+0.11}_{-0.09}$
S	$6.85^{+0.07}_{-0.06}$	$7.12^{+0.15}_{-0.14}$	$6.91^{+0.11}_{-0.09}$	$7.05^{+0.15}_{-0.13}$	$6.94^{+0.09}_{-0.08}$	$6.89^{+0.09}_{-0.08}$	$6.93^{+0.09}_{-0.08}$
Cl	$4.92 \pm 0.06$	$5.03 \pm 0.06$	$4.97 \pm 0.06$	$4.96 \pm 0.08$	$4.99 \pm 0.06$	$4.99 \pm 0.06$	$4.97 \pm 0.05$
Ar	$6.31 \pm 0.06$	$6.42 \pm 0.06$	$6.31^{+0.07}_{-0.06}$	$6.37^{+0.07}_{-0.06}$	$6.33 \pm 0.06$	$6.29^{+0.07}_{-0.06}$	$6.31^{+0.07}_{-0.06}$
Fe*	$6.03 \pm 0.06$	$6.41 \pm 0.07$	$6.07 \pm 0.06$	$<6.54$	$6.06 \pm 0.06$	$6.05 \pm 0.06$	$6.08 \pm 0.06$
Fe**	$5.91 \pm 0.08$	$6.31 \pm 0.08$	$5.94 \pm 0.05$	$<6.50$	$5.94 \pm 0.07$	$5.92 \pm 0.08$	$5.95 \pm 0.07$
Ni	$4.58^{+0.17}_{-0.15}$	$5.20^{+0.24}_{-0.15}$	$4.57^{+0.20}_{-0.18}$	$4.88^{+0.28}_{-0.16}$	$4.58^{+0.21}_{-0.17}$	$4.61^{+0.17}_{-0.14}$	$4.66^{+0.14}_{-0.12}$

**Table 18.** Total abundances based on CELs with  $t^2 > 0.0$ .

Element	Cut 1	Cut 2		Cut 3		Cut 4	Combined cuts
	Nebula	Shock	Nebula	Shock	Nebula	Nebula	
O	$8.66 \pm 0.05$	$8.72 \pm 0.04$	$8.66 \pm 0.05$	$8.61 \pm 0.04$	$8.64 \pm 0.04$	$8.67 \pm 0.05$	$8.66 \pm 0.05$
N	$7.74^{+0.21}_{-0.15}$	$7.60^{+0.39}_{-0.23}$	$7.77^{+0.24}_{-0.17}$	$7.73^{+0.39}_{-0.23}$	$7.76^{+0.23}_{-0.17}$	$7.78^{+0.23}_{-0.17}$	$7.76^{+0.23}_{-0.16}$
Ne	$8.10^{+0.19}_{-0.15}$	$8.14^{+0.09}_{-0.08}$	$8.10^{+0.16}_{-0.14}$	$7.98^{+0.08}_{-0.07}$	$8.08^{+0.14}_{-0.12}$	$8.14^{+0.16}_{-0.13}$	$8.09^{+0.15}_{-0.12}$
S	$6.91^{+0.11}_{-0.09}$	$7.19^{+0.19}_{-0.17}$	$6.98^{+0.12}_{-0.09}$	$7.12^{+0.18}_{-0.16}$	$7.01^{+0.11}_{-0.09}$	$6.96^{+0.12}_{-0.09}$	$7.00^{+0.12}_{-0.09}$
Cl	$5.04 \pm 0.06$	$5.17 \pm 0.07$	$5.10 \pm 0.07$	$5.08 \pm 0.08$	$5.12 \pm 0.07$	$5.12 \pm 0.06$	$5.10 \pm 0.06$
Ar	$6.43^{+0.11}_{-0.09}$	$6.53^{+0.13}_{-0.11}$	$6.43^{+0.10}_{-0.08}$	$6.46^{+0.11}_{-0.10}$	$6.43^{+0.08}_{-0.07}$	$6.41^{+0.09}_{-0.08}$	$6.43^{+0.10}_{-0.08}$
Fe*	$6.26 \pm 0.08$	$6.68 \pm 0.09$	$6.29 \pm 0.05$	$<6.83$	$6.41 \pm 0.11$	$6.29 \pm 0.08$	$6.37 \pm 0.10$
Fe**	$6.19 \pm 0.09$	$6.62 \pm 0.10$	$6.22 \pm 0.06$	$<6.80$	$6.35 \pm 0.13$	$6.22 \pm 0.10$	$6.31 \pm 0.11$
Ni	$4.68^{+0.28}_{-0.21}$	$5.27^{+0.38}_{-0.21}$	$4.70^{+0.27}_{-0.20}$	$4.85^{+0.35}_{-0.19}$	$4.70^{+0.25}_{-0.18}$	$4.70^{+0.22}_{-0.16}$	$4.77^{+0.21}_{-0.15}$

**Table 19.** Total abundances based on RLs.

Element	Cut 1	Cut 2		Cut 3		Cut 4	Combined cuts
	Nebula	Shock	Nebula	Shock	Nebula	Nebula	
He	$10.94 \pm 0.02$	$10.95 \pm 0.03$	$10.94 \pm 0.01$	$10.95 \pm 0.03$	$10.94 \pm 0.02$	$10.95 \pm 0.02$	$10.94 \pm 0.02$
C	$8.48^{+0.09}_{-0.08}$	$8.46 \pm 0.03$	$8.45 \pm 0.05$	$8.56 \pm 0.03$	$8.45 \pm 0.06$	$8.44^{+0.06}_{-0.05}$	$8.48^{+0.06}_{-0.05}$
O	$8.71 \pm 0.05$	$8.83 \pm 0.06$	$8.70 \pm 0.03$	$8.83 \pm 0.06$	$8.71 \pm 0.03$	$8.72 \pm 0.03$	$8.73 \pm 0.03$
Ne	-	$8.60 \pm 0.05$	$8.34 \pm 0.15$	-	$8.29^{+0.25}_{-0.20}$	-	-

conclusion is based on the discrepant velocities that those lines show with respect to the rest of lines in the shock components, that show fairly similar velocities independently of the ionization state of the ions and the elements (see §9.1). For example, in the case of [Ne III] $\lambda\lambda$ 3869, 3967, the Atomic Line List v2.05b21 gives  $\lambda\lambda$ 3869.07 $\pm$ 0.09 and 3967.79 $\pm$ 0.10 based on the works of [Persson et al. \(1991\)](#) and [Feuchtgruber et al. \(1997\)](#). These wavelengths give velocities about  $-20$  km s $^{-1}$  displaced with respect to the mean velocity obtained for the rest of the lines. In this case, we decided to adopt the wavelengths  $\lambda\lambda$ 3868.75 and 3967.46 obtained by [Bowen \(1955\)](#) from high-resolution spectroscopy of nebulae. The [Cl III] and [Cl IV] lines show a similar problem; in this case, we adopt the reference wavelengths used by [Esteban et al. \(2004\)](#) that give consistent velocities. The wavelengths adopted for [S III] lines deserve special attention. The values given by the Atomic Line List v2.05b21

are  $\lambda\lambda$ 6312.1 $\pm$ 0.36, 8829.4 $\pm$ 0.49, 9068.6 $\pm$ 0.52 and 9530.6 $\pm$ 0.57, taken from the work by [Kaufman & Martin \(1993\)](#). There is a small (but noticeable at our spectral resolution) discrepancy in the velocity obtained for [S III]  $\lambda$ 6312 and the rest of the lines of about 10 km s $^{-1}$ . Assuming the velocities measured for the H I lines and a large number of other bright lines of the shock component, our best estimation of the rest wavelengths of the observed [S III] lines are  $\lambda\lambda$ 6312.07 $\pm$ 0.01, 8829.70 $\pm$ 0.01, 9068.93 $\pm$ 0.04 and 9530.98 $\pm$ 0.01.

### 9.1 Velocity structure

In Table A7, we present the average velocity and full width at half maximum (FWHM) of each kind of line observed for the shock and nebular components of cut 2 and the shock component of cut 3.

The behaviour of the nebular component of cut 2 is representative of what is observed in the nebular components of the other cuts. In each column, we include in parentheses the number of lines of each kind whose values have been averaged. In this analysis, we discard lines with known blends and those affected by ghosts or by telluric emissions/absorptions. For O I, O II, C II and Ne II lines, we include only the lines used in § 5.2 for abundance determinations, ensuring that they are pure recombination lines and not affected by fluorescence. In the special case of [S III] lines we consider only the  $\lambda 6312$  line, due to the aforementioned inaccuracies in the theoretical wavelengths of the rest of the [S III] lines. Fig. 14, shows the heliocentric velocity as a function of ionization potential relation for the data collected in Table A7.

From Fig. 14, it is clear that the nebular component presents a pattern consistent with the "blister" model for the Huygens Region of the Orion Nebula (O'Dell 2001; Ferland 2001; O'Dell et al. 2020, and references therein). The basic idea is that a layer of gas of the Orion Molecular Cloud (OMC) facing the direction towards the Sun is ionized by  $\theta^1$  Ori C, which is located in the foreground of OMC. As the gas gets ionized, it is accelerated towards the observer. Velocities of [O I], [C I], [N I], [Cr II], [Ni II] and [Fe II] are similar to the average velocity of the molecules in the OMC ( $\sim 28$  km s $^{-1}$  Goudis 1982; O'Dell 2018, and references therein). This behaviour has been observed in previous works (Kaler 1967; Fehrenbach 1977; O'Dell & Wen 1992; Esteban & Peimbert 1999) and there is evidence that this emission arise from the partially ionized zone of the nebula. A rapid drop in the observed velocity (which means an increase in velocity compared to the OMC's systemic velocity) of the ions whose ionization potential are between 9 and 13 eV is observed for the nebular component. Elements with ionization potentials beyond 13 eV exhibit a consistent behavior with a constant heliocentric velocity around  $\sim 16$  km s $^{-1}$ .

In the high-velocity components, we observe a homogeneous constant velocity independently of the ionization potential of the ions. There is a difference of around  $\sim 6$  Km s $^{-1}$  in the heliocentric velocity between the high-velocity components of cuts 2 and 3. This is due to the possible contamination of the line profiles by unresolved lower velocity components in the cut 3, as its elongated shape in the spectra (see Fig. 2) and its wider FWHM indicate.

In all components, the heliocentric velocities of the O I, O II, C II and Ne II lines that have been used to derive abundances are consistent with the velocity of the CELs of the recombining ions. This reinforces the assumption that they are produced by pure recombination. The clearest case are the O I lines considered here (those from multiplet 1) in the nebular component. If they were not coming from recombination processes, they would be emitted in neutral and partially ionized zones of the nebula, showing a heliocentric velocity similar to the systematic one of the OMC, around 10 Km s $^{-1}$  higher (from the observer's reference system) than the observed value.

## 9.2 Electron temperature from thermal broadening of the line profiles

The observed line widths are the result of several physical processes. Apart from the instrumental width,  $\sigma_{\text{ins}}$ , the main contributors are the thermal width,  $\sigma_{\text{th}}$ , the fine structure broadening,  $\sigma_{\text{fs}}$  and the non-thermal contribution,  $\sigma_{\text{nt}}$ , which includes effects as turbulence and any other additional broadening process. Following García-

Díaz et al. (2008, their equation 2), we use Eq. (19) to express the relationship commented above.

$$\sigma_{\text{obs}}^2 = \sigma_{\text{th}}^2 + \sigma_{\text{fs}}^2 + \sigma_{\text{ins}}^2 + \sigma_{\text{nt}}^2. \quad (19)$$

The thermal contribution of Eq. (19) is the Doppler broadening and depends linearly on the temperature,  $\sigma_{\text{th}}^2 = 82.5 T_4/A$  (km/s) $^2$ , where  $A$  is the atomic weight of the emitting ion and  $T_4 = T_e/10^4$  (García-Díaz et al. 2008).

In principle, using Eq. (19) we can estimate  $T_e$  from the subtraction of the observed widths of H I and [O III] lines. The instrumental width affects the same for both kinds of lines and should be cancelled in the subtraction. García-Díaz et al. (2008) estimated  $\sigma_{\text{fs}}^2$  (H I) = 10.233 (km/s) $^2$ , finding that  $\sigma_{\text{fs}}^2$  ([O III]) is negligible. On the other hand,  $\sigma_{\text{nt}}^2$  (H I) is not strictly equal to  $\sigma_{\text{nt}}^2$  ([O III]), since the nebular volume occupied by both ions is different. García-Díaz et al. (2008), define  $f$  as the fraction of the volume of H $^+$  occupied by O $^{2+}$  and  $(1-f)$  the fraction filled by O $^+$  and other ions with lower degree of ionization, as N $^+$ . We assume the average value  $\langle f \rangle = 0.76$  estimated by García-Díaz et al. (2008) for the Orion Nebula. Using equations 7 to 10 from García-Díaz et al. (2008), we obtain  $T_e = 8340 \pm 410$  k for the nebular component. In the case of the shock components, we assume  $f = 1.0$  and obtain  $T_e = 8670 \pm 50$  K and  $T_e = 10474 \pm 790$  K for cuts 2 and 3, respectively.

The resulting  $T_e$  values obtained from the observed line widths in the nebular component of cut 2 (representative of the nebular component of the rest of the cuts) and the shock component of the same cut, are in remarkably good agreement with those obtained from the [O III] line ratios, shown in Table 5. In the case of the shock component of cut 3, the large difference between the values obtained from both methods is due to the contamination by several unresolved velocity components, as it is shown in Fig. 2, that broadens the lines and provides wrong higher temperatures.

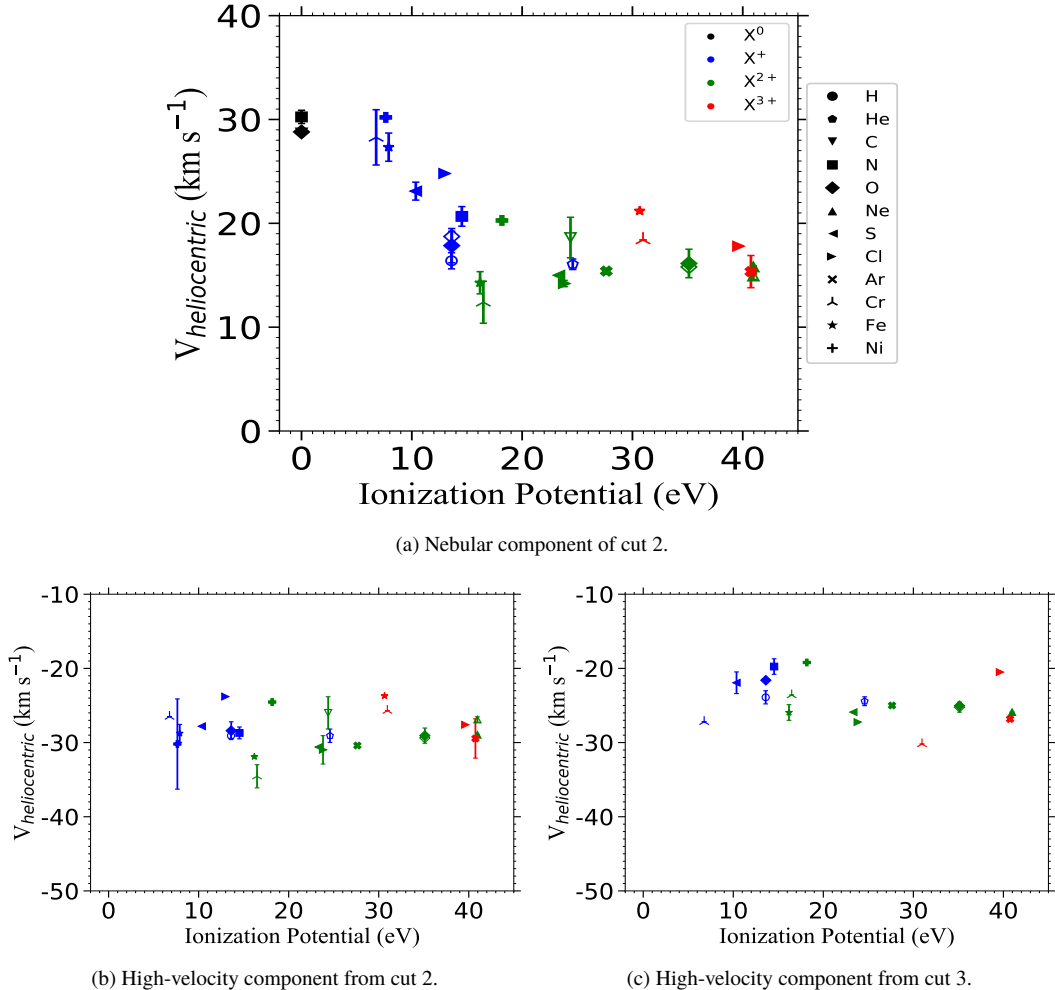
## 10 PHYSICAL ASPECTS OF THE HIGH VELOCITY COMPONENTS

In Fig. 2 we can see that the high-velocity component of cut 3, coincident with HH529III, shows an elongated shape on the spectral axis produced by its larger velocity dispersion. This is the expected kinematical feature at the shock front (working surface) of a jet beam that impacts the surrounding nebular gas. On the other hand, the high-velocity component of cut 2 (HH529II) presents a lower velocity dispersion, with a "ball shape" in the 2D spectra. On the other hand, the physical conditions given in §4 show that the high-velocity component of cut 3 is denser than that of cut 2 between a factor 2 or 4, indicating that the compression of the gas is higher in HH529III.

From a dynamical point of view, Dyson (1984) shown that the interaction of the outflows from low-mass protostars is isothermal. Moreover, this is the appropriate situation for a shock immersed in a fully ionized medium, where the temperature is defined by the thermal equilibrium of an ionized gas. In this case, the compression of the gas is not limited as in the adiabatic case. Using the total or 3D velocity ( $v_{\text{tot}}$ ) of the shock components within the reference framework of the shock, and the sound speed in an ionized gas  $c_0$ , we can estimate the Mach number  $M$ , using Eq. (20) and Eq. (21).

$$M = \frac{|v_{\text{tot}}|}{c_0}, \quad (20)$$

**Figure 14.** Observed heliocentric motion of the ions as a function of the ionization potential for the nebular component and the high-velocity ones. Filled and empty symbols represent CELs and RLs, respectively.



$$c_0 = \sqrt{\frac{\gamma k T}{\mu_0 m_H}}. \quad (21)$$

In §9.1, the heliocentric velocities of the different ions were presented for both shocks. Considering the OMC reference framework ( $\sim 28 \text{ km s}^{-1}$ , Goudis 1982) and the flow angle estimated by O'Dell et al. (2015) for HH529, we obtain total velocities of  $-52.30 \pm 0.89 \text{ km s}^{-1}$  and  $-57.51 \pm 0.36 \text{ km s}^{-1}$  for the high velocity component of cut 3 (HH529III) and cut 2 (HH529II) respectively. Considering  $T_e = 8400 \pm 150 \text{ K}$  for the nebular component and  $\gamma = 1$  (isothermal process), we obtain  $c_0 = 11.80 \pm 0.10 \text{ km s}^{-1}$ . Thus, assuming that both are external working surfaces, we derive a Mach number of  $M = 4.43 \pm 0.08$  and  $M = 4.87 \pm 0.05$  for HH529III and HH529II, respectively.

In the case of an isothermal shock, the ratio between the gas densities before ( $n_{\text{pre}}$ ) and after ( $n_{\text{post}}$ ) the shock follows Eq. (22).

$$\frac{n_{\text{post}}}{n_{\text{pre}}} = M^2 \quad (22)$$

As discussed in §4.2, the density diagnostic based on the [Fe III] lines, is the most representative for the shock fronts considering the geometry of the jet beam. Using this value presented

in Table 5, we obtain a pre-shock density  $n_{\text{pre}} = 2240 \pm 390 \text{ cm}^{-3}$  for HH529III. This value is consistent with densities determined in photoionized areas of the Orion Nebula outside the Huygens region, where the density decreases radially (Mesa-Delgado et al. 2008). This would place HH529III in the foreground of the main ionization front. E: On the other hand, considering also HH529II an external working surface, we would obtain a pre-shock density  $n_{\text{pre}} = 500 \pm 80 \text{ cm}^{-3}$ , indicating that HH529II is impacting the ambient gas in a zone more external from where HH529III does. Thus, HH529II would be located well ahead towards the observer. This scenario seems unlikely, considering the very uniform velocity structure of HH529II and the fairly similar ionization state of the gas in both HH objects. These evidences suggest that the high-velocity component of cut 2 can correspond to an "internal working surface" (Masciadri & Raga 2001) of the jet beam. This internal shock may have its origin in a somewhat later ejection of material from the common origin of HH529 (located at the star COUP 666 by O'Dell et al. 2015), flowing along the jet beam opened by the main shock front (HH529III). This scenario has been studied in detail by Raga & Reipurth (2004) for HH jets emerging from a neutral cloud into an H II region.

In both high-velocity components, it is noticeable the absence of [OI] (see Fig. 2) and the weakness of lines of low ionization

potential ions. This proves that HH529II and HH529III objects are fully photoionized and do not contain a trapped ionization front (Masciadri & Raga 2001), contrary to what was found by Mesa-Delgado et al. (2009) for HH20S. Due to the fact that HH529 is fully photoionized, we can assure that the entire jet beam inside the HII region is observable in optical emission lines, contrary to partially ionized or neutral Herbig-Haro objects, where only limited regions can be observed (Raga et al. 2000a,b). Considering the velocity flow angle with respect the sky plane of  $83^\circ$  estimated by O'Dell et al. (2015) for the HH529 system, the observed spectra of the high-velocity components should integrate the emission along the whole or an important fraction of the ionized jet beam, including the compressed gas in the leading working surface and the gas of the jet beam behind.

In §8, we have observed an increase of the Fe abundance in the high-velocity components of between 0.35 and 0.47 dex with respect to the nebular component, which represents an increase of a factor between 2 and 3 of Fe in the gas-phase. C: Mesa-Delgado et al. (2009) obtained an increase of the Fe/H ratio of about 0.85 dex (a factor 7) for the high-velocity component of HH20S. These results are consistent with theoretical studies predicting that fast shocks are effective destroying dust grains (see Jones et al. 1994; Mouri & Taniguchi 2000, and references therein). C: However, the Fe abundances measured at the shocks of HH529II, HH529III and HH20S are still lower than the solar value of  $12 + \log(\text{Fe}/\text{H}) = 7.45 \pm 0.02$  recommended by Lodders (2019), indicating that the dust is not completely destroyed in the ionized gas entrained by the shocks associated with the HH objects. Another evidence of surviving dust is the detection of thermal dust mid-IR emission at  $11.7 \mu\text{m}$  coincident with both HH529II and III as well as HH20S (Smith et al. 2005). Those authors find that the dust emission is seen behind the shocks or density enhancements within the body of the jet beam, indicating that the dust is either heated by radiation coming from  $\theta^1\text{Ori C}$  or locally by trapped Ly $\alpha$  emission from the high-density zones behind the shocks.

## 11 DISCUSSION

J: - Poner los resultados en el contexto de la geometría.  
 - Efecto en la determinación de abundancias al considerar el espectro integrado.

## 12 CONCLUSIONS

### ACKNOWLEDGEMENTS

We acknowledge support from the State Research Agency (AEI) of the Spanish Ministry of Science, Innovation and Universities (MCIU) and the European Regional Development Fund (FEDER) under grants AYA2015-65205-P and AYA2017-83383-P. JGR acknowledges support from an Advanced Fellowship from the Severo Ochoa excellence program (SEV-2015-0548). KZA-C acknowledges support from Mexican CONACYT posdoctoral grant 364239. The authors acknowledge support under grant P/308614 financed by funds transferred from the Spanish Ministry of Science, Innovation and Universities, charged to the General State Budgets and with funds transferred from the General Budgets of the Autonomous Community of the Canary Islands by the MCIU.

## REFERENCES

- Astropy Collaboration et al., 2013, *A&A*, **558**, A33  
 Aver E., Olive K. A., Skillman E. D., 2011, *J. Cosmology Astropart. Phys.*, **2011**, 043  
 Baldwin J. A., et al., 1996, *ApJ*, **468**, L115  
 Ballester P., Modigliani A., Boitquin O., Cristiani S., Hanuschik R., Kaufer A., Wolf S., 2000, *The Messenger*, **101**, 31  
 Bally J., O'Dell C. R., McCaughrean M. J., 2000, *AJ*, **119**, 2919  
 Bastin R. J., Storey P. J., 2006, in Barlow M. J., Méndez R. H., eds, IAU Symposium Vol. 234, Planetary Nebulae in our Galaxy and Beyond. pp 369–370, doi:10.1017/S1743921306003280  
 Bautista M. A., 2001, *A&A*, **365**, 268  
 Benjamin R. A., Skillman E. D., Smits D. P., 2002, *ApJ*, **569**, 288  
 Berg D. A., Pogge R. W., Skillman E. D., Croxall K. V., Moustakas J., Rogers N. S. J., Sun J., 2020, *ApJ*, **893**, 96  
 Blagrade K. P. M., Martin P. G., Baldwin J. A., 2006, *ApJ*, **644**, 1006  
 Blagrade K. P. M., Martin P. G., Rubin R. H., Dufour R. J., Baldwin J. A., Hester J. J., Walter D. K., 2007, *ApJ*, **655**, 299  
 Bohigas J., 2015, *MNRAS*, **453**, 1281  
 Bowen I. S., 1955, *ApJ*, **121**, 306  
 Brown R. L., Mathews W. G., 1970, *ApJ*, **160**, 939  
 Butler K., Zeippen C. J., 1989, *A&A*, **208**, 337  
 D'Odorico S., Cristiani S., Dekker H., Hill V., Kaufer A., Kim T., Primas F., 2000, Performance of UVES, the echelle spectrograph for the ESO VLT and highlights of the first observations of stars and quasars. pp 121–130, doi:10.1111/12.390133  
 Davey A. R., Storey P. J., Kisielius R., 2000, *A&AS*, **142**, 85  
 Delgado-Inglada G., Morisset C., Stasińska G., 2014, *MNRAS*, **440**, 536  
 Delgado-Inglada G., Mesa-Delgado A., García-Rojas J., Rodríguez M., Esteban C., 2016, *MNRAS*, **456**, 3855  
 Domínguez-Guzmán G., Rodríguez M., Esteban C., García-Rojas J., 2019, arXiv e-prints, p. arXiv:1906.02102  
 Dyson J. E., 1984, *Ap&SS*, **106**, 181  
 Ellis D. G., Martinson I., 1984, *Phys. Scr.*, **30**, 255  
 Espíritu J. N., Peimbert A., Delgado-Inglada G., Ruiz M. T., 2017, *Rev. Mex. Astron. Astrofis.*, **53**, 95  
 Esteban C., Peimbert M., 1999, *A&A*, **349**, 276  
 Esteban C., Peimbert M., Torres-Peimbert S., Escalante V., 1998, *MNRAS*, **295**, 401  
 Esteban C., Peimbert M., García-Rojas J., Ruiz M. T., Peimbert A., Rodríguez M., 2004, *MNRAS*, **355**, 229  
 Fang X., Liu X. W., 2011, *MNRAS*, **415**, 181  
 Fang X., Liu X. W., 2013, *MNRAS*, **429**, 2791  
 Fehrenbach C., 1977, *A&AS*, **29**, 71  
 Ferland G. J., 2001, *PASP*, **113**, 41  
 Ferland G. J., Henney W. J., O'Dell C. R., Porter R. L., van Hoof P. A. M., Williams R. J. R., 2012, *ApJ*, **757**, 79  
 Feuchtgruber H., et al., 1997, *ApJ*, **487**, 962  
 Fritzsche S., Fricke B., Geschke D., Heitmann A., Sienkiewicz J. E., 1999, *ApJ*, **518**, 994  
 Froese Fischer C., Tachiev G., 2004, *Atomic Data and Nuclear Data Tables*, **87**, 1  
 Froese Fischer C., Rubin R. H., Rodríguez M., 2008, *MNRAS*, **391**, 1828  
 Galavis M. E., Mendoza C., Zeippen C. J., 1995, *A&AS*, **111**, 347  
 García-Díaz M. T., Henney W. J., López J. A., Doi T., 2008, *Rev. Mex. Astron. Astrofis.*, **44**, 181  
 García-Rojas J., Esteban C., 2007, *ApJ*, **670**, 457  
 García-Rojas J., Esteban C., Peimbert M., Rodríguez M., Ruiz M. T., Peimbert A., 2004, *ApJS*, **153**, 501  
 García-Rojas J., Esteban C., Peimbert A., Peimbert M., Rodríguez M., Ruiz M. T., 2005, *MNRAS*, **362**, 301  
 García-Rojas J., Esteban C., Peimbert A., Rodríguez M., Peimbert M., Ruiz M. T., 2007, *Rev. Mex. Astron. Astrofis.*, **43**, 3  
 García-Rojas J., Peña M., Morisset C., Delgado-Inglada G., Mesa-Delgado A., Ruiz M. T., 2013, *A&A*, **558**, A122  
 García-Rojas J., Madonna S., Luridiana V., Sterling N. C., Morisset C., Delgado-Inglada G., Toribio San Cipriano L., 2015, *MNRAS*, **452**,

2606

- Goudis C., 1982, The Orion complex: A case study of interstellar matter. Vol. 90, doi:10.1007/978-94-009-7712-9,
- Grieve M. F. R., Ramsbottom C. A., Hudson C. E., Keenan F. P., 2014, *ApJ*, **780**, 110
- Jenkins E. B., 2009, *ApJ*, **700**, 1299
- Johansson S., Zethson T., Hartman H., Ekberg J. O., Ishibashi K., Davidson K., Gull T., 2000, *A&A*, **361**, 977
- Jones A. P., Tielens A. G. G. M., Hollenbach D. J., McKee C. F., 1994, *ApJ*, **433**, 797
- Kaler J. B., 1967, *ApJ*, **148**, 925
- Kaufman V., Martin W. C., 1993, *Journal of Physical and Chemical Reference Data*, **22**, 279
- Kaufman V., Sugar J., 1986, *Journal of Physical and Chemical Reference Data*, **15**, 321
- Kingdon J. B., Ferland G. J., 1995, *ApJ*, **450**, 691
- Kisielius R., Storey P. J., Davey A. R., Neale L. T., 1998, *A&AS*, **133**, 257
- Kisielius R., Storey P. J., Ferland G. J., Keenan F. P., 2009, *MNRAS*, **397**, 903
- Kunth D., Sargent W. L. W., 1983, *ApJ*, **273**, 81
- Liu X. W., Storey P. J., Barlow M. J., Danziger I. J., Cohen M., Bryce M., 2000, *MNRAS*, **312**, 585
- Liu X. W., Luo S. G., Barlow M. J., Danziger I. J., Storey P. J., 2001, *MNRAS*, **327**, 141
- Lodders K., 2019, arXiv e-prints, p. arXiv:1912.00844
- Lucy L. B., 1995, *A&A*, **294**, 555
- Luridiana V., Morisset C., Shaw R. A., 2015, *A&A*, **573**, A42
- Masciadri E., Raga A. C., 2001, *A&A*, **376**, 1073
- McLaughlin B. M., Lee T.-G., Ludlow J. A., Land i E., Loch S. D., Pindzola M. S., Ballance C. P., 2011, *Journal of Physics B Atomic Molecular Physics*, **44**, 175206
- McNabb I. A., Fang X., Liu X. W., Bastin R. J., Storey P. J., 2013, *MNRAS*, **428**, 3443
- Mendoza C., 1983, in Aller L. H., ed., IAU Symposium Vol. 103, Planetary Nebulae. pp 143–172
- Mendoza C., Zeippen C. J., 1982a, *MNRAS*, **198**, 127
- Mendoza C., Zeippen C. J., 1982b, *MNRAS*, **199**, 1025
- Mendoza C., Zeippen C. J., 1983, *MNRAS*, **202**, 981
- Mesa-Delgado A., Esteban C., García-Rojas J., 2008, *ApJ*, **675**, 389
- Mesa-Delgado A., Esteban C., García-Rojas J., Luridiana V., Bautista M., Rodríguez M., López-Martín L., Peimbert M., 2009, *MNRAS*, **395**, 855
- Moehler S., Dreizler S., LeBlanc F., Khalack V., Michaud G., Richer J., Sweigart A. V., Grundahl F., 2014a, *A&A*, **565**, A100
- Moehler S., et al., 2014b, *A&A*, **568**, A9
- Mouri H., Taniguchi Y., 2000, *ApJ*, **534**, L63
- Nicholls D. C., Dopita M. A., Sutherland R. S., 2012, *ApJ*, **752**, 148
- Noll S., Kausch W., Barden M., Jones A. M., Szyszka C., Kimeswenger S., Vinther J., 2012, *A&A*, **543**, A92
- O'Dell C. R., 2001, *ARA&A*, **39**, 99
- O'Dell C. R., 2018, *MNRAS*, **478**, 1017
- O'Dell C. R., Henney W. J., 2008, *AJ*, **136**, 1566
- O'Dell C. R., Wen Z., 1992, *ApJ*, **387**, 229
- O'Dell C. R., Ferland G. J., Henney W. J., Peimbert M., García-Díaz M. T., Rubin R. H., 2015, *AJ*, **150**, 108
- O'Dell C. R., Abel N. P., Ferland G. J., 2020, *ApJ*, **891**, 46
- Olive K. A., Skillman E. D., 2004, *ApJ*, **617**, 29
- Osterbrock D. E., Ferland G. J., 2006, Astrophysics of gaseous nebulae and active galactic nuclei
- Osterbrock D. E., Tran H. D., Veilleux S., 1992, *ApJ*, **389**, 305
- Pagel B. E. J., Simonson E. A., Terlevich R. J., Edmunds M. G., 1992, *MNRAS*, **255**, 325
- Peimbert M., 1967, *ApJ*, **150**, 825
- Peimbert A., 2003, *ApJ*, **584**, 735
- Peimbert M., Costero R., 1969, Boletín de los Observatorios Tonantzintla y Tacubaya, **5**, 3
- Peimbert A., Peimbert M., 2013, *ApJ*, **778**, 89
- Peimbert A., Peimbert M., Luridiana V., 2002, *ApJ*, **565**, 668
- Pequignot D., Petitjean P., Boisson C., 1991, *A&A*, **251**, 680
- Persson W., Wahlström C.-G., Jönsson L., Di Rocco H. O., 1991, *Phys. Rev. A*, **43**, 4791
- Podobedova L. I., Kelleher D. E., Wiese W. L., 2009, *Journal of Physical and Chemical Reference Data*, **38**, 171
- Porter R. L., Ferland G. J., MacAdam K. B., 2007, *ApJ*, **657**, 327
- Porter R. L., Ferland G. J., Storey P. J., Detisch M. J., 2012, *MNRAS*, **425**, L28
- Porter R. L., Ferland G. J., Storey P. J., Detisch M. J., 2013, *MNRAS*, **433**, L89
- Price-Whelan A. M., et al., 2018, *AJ*, **156**, 123
- Quinet P., 1996, *A&AS*, **116**, 573
- Raga A. C., Reipurth B., 2004, *Rev. Mex. Astron. Astrofis.*, **40**, 15
- Raga A. C., López-Martín J., López J. A., Meaburn J., 2000a, in Arthur S. J., Brickhouse N. S., Franco J., eds, *Revista Mexicana de Astronomía y Astrofísica Conference Series Vol. 9, Revista Mexicana de Astronomía y Astrofísica Conference Series*. pp 191–193
- Raga A., et al., 2000b, *MNRAS*, **314**, 681
- Ramsbottom C. A., Bell K. L., 1997, *Atomic Data and Nuclear Data Tables*, **66**, 65
- Rodríguez M., 1999, *A&A*, **348**, 222
- Rodríguez M., 2002, *A&A*, **389**, 556
- Rodríguez M., 2020, arXiv e-prints, p. arXiv:2005.03798
- Rodríguez M., Rubin R. H., 2005, *ApJ*, **626**, 900
- Smith N., Bally J., Shuping R. Y., Morris M., Kassis M., 2005, *AJ*, **130**, 1763
- Stasińska G., Tenorio-Tagle G., Rodríguez M., Henney W. J., 2007, *A&A*, **471**, 193
- Storey P. J., 1994, *A&A*, **282**, 999
- Storey P. J., Hummer D. G., 1995, *MNRAS*, **272**, 41
- Storey P. J., Zeippen C. J., 2000, *MNRAS*, **312**, 813
- Storey P. J., Sochi T., Badnell N. R., 2014, *MNRAS*, **441**, 3028
- Storey P. J., Sochi T., Bastin R., 2017, *MNRAS*, **470**, 379
- Sugar J., Corliss C., 1985, Atomic energy levels of the iron-period elements: Potassium through Nickel
- Tayal S. S., 2004, *A&A*, **418**, 363
- Tayal S. S., 2011, *ApJS*, **195**, 12
- Tayal S. S., Zatsarinsky O., 2010, *ApJS*, **188**, 32
- Tody D., 1993, *IRAF in the Nineties*. p. 173
- Torres-Peimbert S., Peimbert M., Daltabuit E., 1980, *ApJ*, **238**, 133
- Tsamis Y. G., Walsh J. R., Vilchez J. M., Péquignot D., 2011, *MNRAS*, **412**, 1367
- Van Hoof P. A. M., 2018, *Galaxies*, **6**
- Verner E. M., Verner D. A., Baldwin J. A., Ferland G. J., Martin P. G., 2000, *ApJ*, **543**, 831
- Vilchez J. M., Pagel B. E. J., 1988, *MNRAS*, **231**, 257
- Walter D. K., Dufour R. J., Hester J. J., 1992, *ApJ*, **397**, 196
- Wesson R., Jones D., García-Rojas J., Boffin H. M. J., Corradi R. L. M., 2018, *MNRAS*, **480**, 4589
- Wiese W. L., Fuhr J. R., Deters T. M., 1996, *Journal of Physical and Chemical Reference Data, Monograph 7*, 403
- Zhang Y., Liu X. W., 2006, in Barlow M. J., Méndez R. H., eds, *IAU Symposium Vol. 234, Planetary Nebulae in our Galaxy and Beyond*. pp 547–548 (arXiv:astro-ph/0605180), doi:10.1017/S1743921306004170
- Zhang H. L., Pradhan A. K., 1997, *A&AS*, **126**, 373
- Zhang, Hong Lin 1996, *Astron. Astrophys. Suppl. Ser.*, **119**, 523
- Zhang Y., Liu X. W., Liu Y., Rubin R. H., 2005, *MNRAS*, **358**, 457

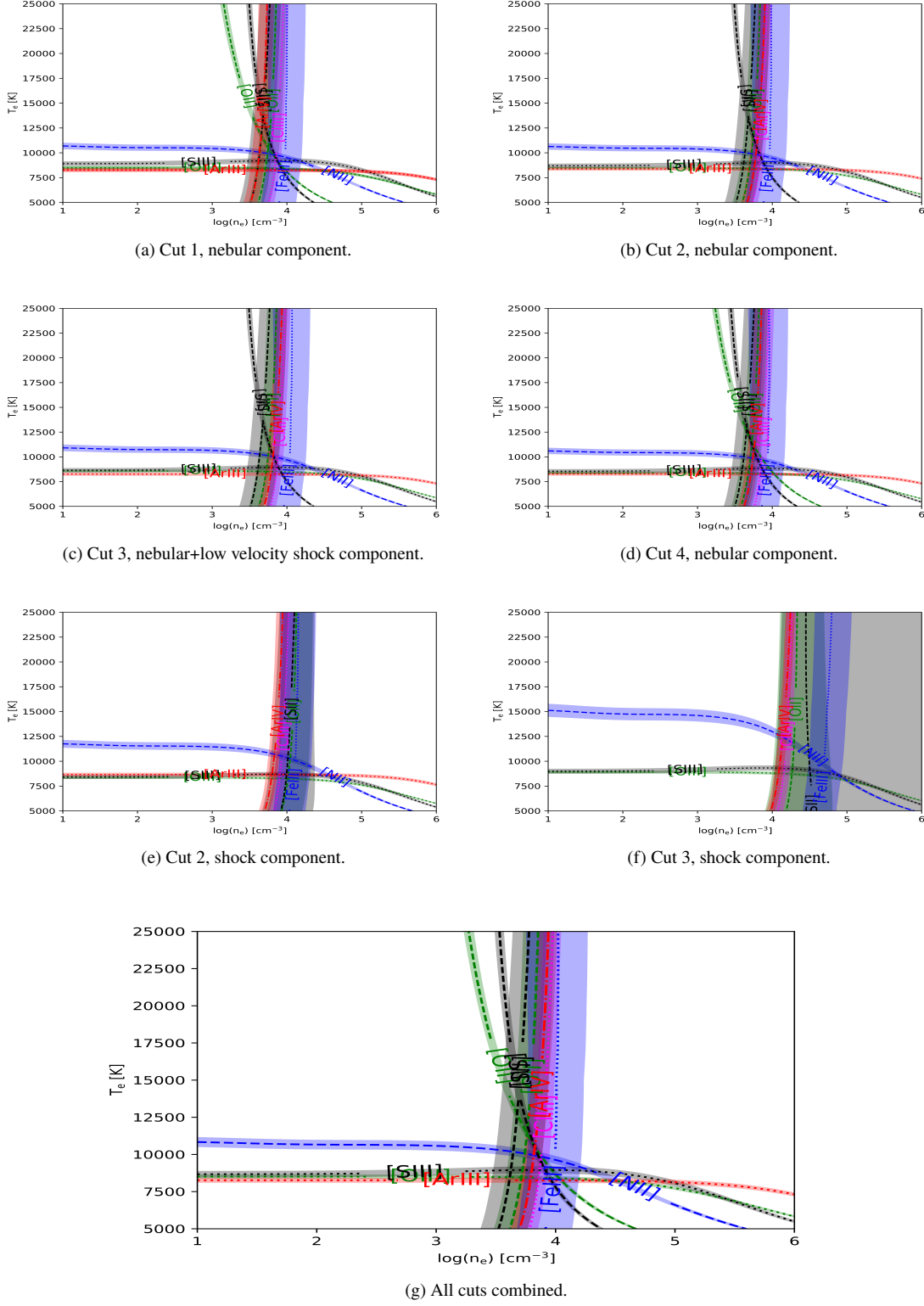
**Table A1.** Slope and intercept for Eq. 4 for a range of densities.

$n_e$ ( $\text{cm}^{-3}$ )	$\alpha$	$\beta$
100	92984	-7455
500	81830	-6031
1000	77896	-5527
2000	69126	-4378
3000	65040	-3851
4000	62517	-3529
5000	60744	-3305
6000	59402	-3137
7000	58334	-3004
8000	57456	-2895
9000	56715	-2804
10000	56077	-2726
12000	55637	-2676
15000	55087	-2611
20000	54364	-2523

**APPENDIX A: SOME EXTRA MATERIAL**

J: In this appendix we show some of the Tables and Figures of the paper. Bla bla bla

This paper has been typeset from a  $\text{\TeX}/\text{\LaTeX}$  file prepared by the author.

**Figure A1.** Plasma diagnostic plots for the different cuts and components in the spectra of HH 529 III.

**Table A2.** Fe<sup>2+</sup> abundances based on  $T_e$  (low).

$\lambda$	Cut 1 Nebula	Cut 2 Shock	Cut 2 Nebula	Cut 3 Shock	Cut 3 Nebula	Cut 4 Nebula	Combined cuts
4658	$5.51 \pm 0.02$	$5.53^{+0.09}_{-0.07}$	$5.56^{+0.04}_{-0.03}$	$5.23^{+0.10}_{-0.07}$	$5.51 \pm 0.04$	$5.47^{+0.05}_{-0.04}$	$5.52 \pm 0.03$
4702	$5.51 \pm 0.02$	$5.54^{+0.09}_{-0.07}$	$5.56^{+0.04}_{-0.03}$	$5.23^{+0.10}_{-0.07}$	$5.52 \pm 0.04$	$5.47^{+0.05}_{-0.04}$	$5.52^{+0.04}_{-0.03}$
4734	$5.48 \pm 0.03$	$5.53^{+0.09}_{-0.07}$	$5.56 \pm 0.04$	$5.35^{+0.11}_{-0.08}$	$5.50^{+0.05}_{-0.04}$	$5.47^{+0.05}_{-0.04}$	$5.52 \pm 0.04$
4755	$5.51^{+0.03}_{-0.02}$	$5.55^{+0.09}_{-0.07}$	$5.58^{+0.04}_{-0.03}$	$5.29^{+0.11}_{-0.08}$	$5.52^{+0.05}_{-0.04}$	$5.49^{+0.05}_{-0.04}$	$5.54^{+0.04}_{-0.03}$
4770	$5.51 \pm 0.03$	$5.58^{+0.09}_{-0.07}$	$5.59 \pm 0.04$	$5.36^{+0.11}_{-0.08}$	$5.55^{+0.05}_{-0.04}$	$5.48^{+0.05}_{-0.04}$	$5.56^{+0.04}_{-0.03}$
4778	$5.51 \pm 0.04$	$5.69^{+0.09}_{-0.07}$	$5.59 \pm 0.04$	$5.20^{+0.14}_{-0.11}$	$5.51^{+0.05}_{-0.04}$	$5.42^{+0.06}_{-0.05}$	$5.55 \pm 0.04$
4881	$5.53 \pm 0.02$	$5.56^{+0.08}_{-0.07}$	$5.58^{+0.04}_{-0.03}$	$5.28^{+0.10}_{-0.08}$	$5.53 \pm 0.04$	$5.49^{+0.05}_{-0.04}$	$5.54 \pm 0.03$
5011	$5.52 \pm 0.04$	$5.73^{+0.09}_{-0.07}$	$5.56 \pm 0.04$	$5.41^{+0.11}_{-0.09}$	$5.51^{+0.05}_{-0.04}$	$5.51^{+0.06}_{-0.05}$	$5.57 \pm 0.04$
5271	$5.55 \pm 0.02$	$5.56^{+0.08}_{-0.06}$	$5.58^{+0.04}_{-0.03}$	$5.28^{+0.10}_{-0.07}$	$5.55 \pm 0.04$	$5.52 \pm 0.04$	$5.55 \pm 0.03$
5412	$5.57^{+0.06}_{-0.05}$	$5.63^{+0.10}_{-0.08}$	$5.60^{+0.05}_{-0.04}$	-	$5.57^{+0.05}_{-0.04}$	$5.58^{+0.07}_{-0.06}$	$5.56 \pm 0.05$
8838	$5.37^{+0.11}_{-0.10}$	$5.33^{+0.19}_{-0.15}$	$5.48^{+0.08}_{-0.07}$	-	$5.34^{+0.09}_{-0.08}$	$5.47^{+0.11}_{-0.09}$	$5.34^{+0.09}_{-0.08}$
<b>Weighted Average</b>	<b><math>5.52 \pm 0.03</math></b>	<b><math>5.56 \pm 0.08</math></b>	<b><math>5.57 \pm 0.02</math></b>	<b><math>5.28 \pm 0.06</math></b>	<b><math>5.52 \pm 0.04</math></b>	<b><math>5.48 \pm 0.03</math></b>	<b><math>5.53 \pm 0.04</math></b>

**Table A3.** Fe<sup>2+</sup> abundances based on  $T_e$  (high).

$\lambda$	Cut 1 Nebula	Cut 2 Shock	Cut 2 Nebula	Cut 3 Shock	Cut 3 Nebula	Cut 4 Nebula	Combined cuts
4658	$5.77^{+0.05}_{-0.04}$	$5.91^{+0.03}_{-0.02}$	$5.81 \pm 0.03$	$5.70^{+0.03}_{-0.02}$	$5.78 \pm 0.03$	$5.75 \pm 0.03$	$5.79 \pm 0.03$
4702	$5.76^{+0.05}_{-0.04}$	$5.91 \pm 0.03$	$5.80 \pm 0.03$	$5.71 \pm 0.03$	$5.78 \pm 0.03$	$5.74 \pm 0.03$	$5.79^{+0.04}_{-0.03}$
4734	$5.74^{+0.05}_{-0.04}$	$5.90^{+0.04}_{-0.03}$	$5.81^{+0.04}_{-0.03}$	$5.82^{+0.06}_{-0.05}$	$5.77^{+0.04}_{-0.03}$	$5.75^{+0.04}_{-0.03}$	$5.79 \pm 0.04$
4755	$5.76^{+0.05}_{-0.04}$	$5.93 \pm 0.03$	$5.83 \pm 0.03$	$5.77 \pm 0.05$	$5.79 \pm 0.03$	$5.76 \pm 0.03$	$5.81 \pm 0.03$
4770	$5.76^{+0.05}_{-0.04}$	$5.95 \pm 0.03$	$5.84 \pm 0.03$	$5.83 \pm 0.05$	$5.81^{+0.04}_{-0.03}$	$5.75^{+0.04}_{-0.03}$	$5.82^{+0.04}_{-0.03}$
4778	$5.76^{+0.06}_{-0.05}$	$6.07 \pm 0.04$	$5.84^{+0.04}_{-0.03}$	$5.68^{+0.10}_{-0.09}$	$5.78^{+0.04}_{-0.03}$	$5.70^{+0.05}_{-0.04}$	$5.82 \pm 0.04$
4881	$5.79 \pm 0.04$	$5.93 \pm 0.03$	$5.83 \pm 0.03$	$5.76 \pm 0.04$	$5.79 \pm 0.03$	$5.76 \pm 0.03$	$5.80 \pm 0.03$
5011	$5.76^{+0.06}_{-0.05}$	$6.08 \pm 0.04$	$5.79 \pm 0.03$	$5.86^{+0.07}_{-0.06}$	$5.76 \pm 0.03$	$5.77^{+0.05}_{-0.04}$	$5.82 \pm 0.04$
5271	$5.77 \pm 0.04$	$5.90 \pm 0.03$	$5.81 \pm 0.03$	$5.72^{+0.04}_{-0.03}$	$5.79 \pm 0.03$	$5.77 \pm 0.03$	$5.79 \pm 0.03$
5412	$5.80^{+0.07}_{-0.06}$	$5.97^{+0.07}_{-0.06}$	$5.83 \pm 0.04$	-	$5.81 \pm 0.04$	$5.83 \pm 0.06$	$5.80 \pm 0.05$
8838	$5.73^{+0.12}_{-0.11}$	$5.87 \pm 0.13$	$5.83^{+0.07}_{-0.06}$	-	$5.72^{+0.08}_{-0.07}$	$5.86 \pm 0.09$	$5.72^{+0.09}_{-0.08}$
<b>Weighted Average</b>	<b><math>5.77 \pm 0.02</math></b>	<b><math>5.93 \pm 0.05</math></b>	<b><math>5.82 \pm 0.02</math></b>	<b><math>5.73 \pm 0.05</math></b>	<b><math>5.78 \pm 0.02</math></b>	<b><math>5.76 \pm 0.03</math></b>	<b><math>5.80 \pm 0.02</math></b>

**Table A4.** Cl<sup>2+</sup> and Cl abundances and Cl/O ratio using  $T_e$ (low),  $T_e$ ([S III]) and  $T_e$ (high).

Cut	Component	O <sup>2+</sup> /O	Cl <sup>2+</sup> /H <sup>+</sup>	$T_e$ (low)	$T_e$ (high)	$T_e$ ([S III])	$T_e$ (high)			
		Cl/H	Cl/O	Cl <sup>2+</sup> /H <sup>+</sup>	Cl/H	Cl/O	Cl <sup>2+</sup> /H <sup>+</sup>	Cl/H	Cl/O	
1	Nebular	$0.73 \pm 0.04$	$4.78 \pm 0.02$	$4.83 \pm 0.02$	$-3.63 \pm 0.03$	$4.88^{+0.06}_{-0.05}$	$4.92 \pm 0.06$	$-3.53 \pm 0.07$	$5.01 \pm 0.03$	$5.04 \pm 0.03$
2	Shock	$0.96 \pm 0.04$	$4.75^{+0.08}_{-0.06}$	$4.79 \pm 0.08$	$-3.77 \pm 0.08$	$5.01^{+0.06}_{-0.05}$	$5.03 \pm 0.06$	$-3.53 \pm 0.07$	$5.08 \pm 0.03$	$5.10 \pm 0.03$
2	Nebular	$0.77 \pm 0.05$	$4.81^{+0.04}_{-0.03}$	$4.86 \pm 0.04$	$-3.61 \pm 0.06$	$4.93^{+0.06}_{-0.05}$	$4.97 \pm 0.06$	$-3.49 \pm 0.07$	$5.03 \pm 0.03$	$5.06 \pm 0.03$
3	Shock	$0.95 \pm 0.04$	$4.61^{+0.07}_{-0.06}$	$4.64 \pm 0.09$	$-3.82 \pm 0.09$	$4.95^{+0.06}_{-0.05}$	$4.96 \pm 0.08$	$-3.50 \pm 0.08$	$5.03 \pm 0.03$	$5.04 \pm 0.03$
3	Low velocity shock+nebula	$0.79 \pm 0.05$	$4.80^{+0.04}_{-0.03}$	$4.85 \pm 0.04$	$-3.60 \pm 0.06$	$4.96^{+0.06}_{-0.05}$	$4.99 \pm 0.06$	$-3.46 \pm 0.07$	$5.03^{+0.03}_{-0.02}$	$5.06 \pm 0.03$
4	Nebular	$0.78 \pm 0.05$	$4.79 \pm 0.04$	$4.85 \pm 0.04$	$-3.62 \pm 0.06$	$4.95^{+0.05}_{-0.04}$	$4.99 \pm 0.06$	$-3.48 \pm 0.07$	$5.03 \pm 0.03$	$5.06 \pm 0.03$
-	Combined cuts	$0.81 \pm 0.05$	$4.79 \pm 0.03$	$4.84 \pm 0.03$	$-3.62 \pm 0.05$	$4.94^{+0.05}_{-0.04}$	$4.97 \pm 0.05$	$-3.50 \pm 0.06$	$5.02 \pm 0.03$	$5.05 \pm 0.03$

**Table A5.** Ni<sup>2+</sup> abundances per line.

$\lambda$	Cut 1 Nebula	Cut 2 Shock	Cut 2 Nebula	Cut 3 Shock	Cut 3 Nebula	Cut 4 Nebula	Combined cuts
6000	$4.52 \pm 0.08$	$4.38^{+0.13}_{-0.12}$	$4.34^{+0.07}_{-0.06}$	-	$4.40 \pm 0.07$	$4.42^{+0.10}_{-0.09}$	$4.35 \pm 0.08$
6534	$4.22^{+0.10}_{-0.11}$	$4.56:$	$4.19 \pm 0.06$	$4.22:$	$4.16 \pm 0.07$	$4.18 \pm 0.11$	$4.26 \pm 0.07$
6682	$4.76^{+0.14}_{-0.13}$	-	$4.70^{+0.14}_{-0.13}$	-	$4.44^{+0.14}_{-0.13}$	-	-
6797	$4.50^{+0.23}_{-0.22}$	$4.96:$	$4.79 \pm 0.08$	-	$4.77 \pm 0.10$	$4.81:$	$4.77 \pm 0.14$
6946	$3.94^{+0.26}_{-0.23}$	$4.70^{+0.19}_{-0.17}$	$4.23 \pm 0.11$	$4.29:$	$4.21 \pm 0.11$	$4.23^{+0.15}_{-0.14}$	$4.31:$
7890	$4.42 \pm 0.04$	$4.48^{+0.08}_{-0.06}$	$4.49 \pm 0.04$	$4.18^{+0.12}_{-0.10}$	$4.45^{+0.05}_{-0.04}$	$4.45^{+0.05}_{-0.04}$	$4.46 \pm 0.04$
<b>Weighted Average</b>	<b><math>4.37 \pm 0.14</math></b>	<b><math>4.47 \pm 0.11</math></b>	<b><math>4.33 \pm 0.17</math></b>	<b><math>4.18 \pm 0.12</math></b>	<b><math>4.32 \pm 0.16</math></b>	<b><math>4.36 \pm 0.12</math></b>	<b><math>4.38 \pm 0.10</math></b>

**Table A6.** Values of  $t^2$  estimated for each component, based on the combination of Eq.(12) with Eq.(13), Eq.(14) and Eq.(15).

Cut	Component	$t^2(\text{O}^{2+})$	$t^2(\text{S}^{2+})$	$t^2(\text{N}^+)$
1	Nebular	$0.004 \pm 0.012$	$0.040 \pm 0.026$	$0.053 \pm 0.018$
2	Shock	$0.023 \pm 0.014$	$0.057 \pm 0.028$	$0.105 \pm 0.026$
2	Nebular	$0.008 \pm 0.012$	$0.039 \pm 0.025$	$0.058 \pm 0.018$
3	Shock	$0.024 \pm 0.012$	$0.065 \pm 0.028$	$0.147 \pm 0.032$
3	Low velocity shock+nebula	$0.010 \pm 0.013$	$0.036 \pm 0.026$	$0.064 \pm 0.019$
4	Nebular	$0.022 \pm 0.014$	$0.062 \pm 0.027$	$0.079 \pm 0.020$

**Table A7.** Average velocities and FWHM for the observed ions for selected cuts and components.

Ion	I.P. (eV)	Nebular Cut 2		Shock Cut 2		Shock Cut 3	
		$\langle V \rangle$ (Km s $^{-1}$ )	$\langle \text{FWHM} \rangle$ (Km s $^{-1}$ )	$\langle V \rangle$ (Km s $^{-1}$ )	$\langle \text{FWHM} \rangle$ (Km s $^{-1}$ )	$\langle V \rangle$ (Km s $^{-1}$ )	$\langle \text{FWHM} \rangle$ (Km s $^{-1}$ )
[O I]	0.00	$28.80 \pm 0.03$ (2)	$11.80 \pm 0.02$ (2)	-	-	-	-
[C I]	0.00	$28.70 \pm 0.03$ (3)	$9.49 \pm 0.10$ (3)	-	-	-	-
[N I]	0.00	$30.25 \pm 0.64$ (3)	$9.51 \pm 0.60$ (3)	-	-	-	-
[Cr II]	6.77	$28.28 \pm 2.66$ (5)	$9.71 \pm 1.19$ (5)	$-26.50 \pm 1.00$ (1)	$25.60 \pm 1.00$ (1)	$-27.20 \pm 1.00$ (1)	$39.40 \pm 1.00$ (1)
[Ni II]	7.64	$30.20 \pm 0.08$ (10)	$11.75 \pm 0.63$ (10)	$-30.20 \pm 6.09$ (3)	$15.81 \pm 2.83$ (3)	-	-
[Fe II]	7.90	$27.33 \pm 1.36$ (34)	$11.84 \pm 2.29$ (34)	$-28.76 \pm 1.21$ (2)	$13.66 \pm 0.97$ (2)	-	-
[S II]	10.36	$23.10 \pm 0.86$ (4)	$21.52 \pm 0.90$ (4)	$-27.80 \pm 0.03$ (4)	$16.29 \pm 0.45$ (4)	$-21.94 \pm 1.46$ (6)	$22.92 \pm 1.00$ (6)
[Cl II]	12.97	$24.80 \pm 1.00$ (1)	$20.40 \pm 1.00$ (1)	$-23.80 \pm 1.00$ (1)	$18.90 \pm 1.00$ (1)	-	-
H I	13.60	$16.39 \pm 0.78$ (51)	$24.95 \pm 0.16$ (51)	$-29.08 \pm 0.36$ (51)	$27.20 \pm 0.01$ (51)	$-23.90 \pm 0.89$ (45)	$33.12 \pm 0.44$ (45)
[O II]	13.62	$17.85 \pm 1.65$ (2)	$18.69 \pm 0.69$ (2)	$-28.40 \pm 1.20$ (2)	$20.04 \pm 1.10$ (2)	$-21.60 \pm 0.03$ (2)	$25.27 \pm 0.53$ (2)
O I	13.62	$18.73 \pm 0.50$ (3)	$23.29 \pm 0.86$ (3)	-	-	-	-
[N II]	14.53	$20.67 \pm 0.95$ (4)	$19.45 \pm 0.05$ (4)	$-28.70 \pm 0.80$ (4)	$18.13 \pm 0.45$ (4)	$-19.75 \pm 1.05$ (3)	$25.98 \pm 0.19$ (3)
[Fe III]	16.19	$13.83 \pm 1.09$ (21)	$12.10 \pm 0.32$ (21)	$-31.90 \pm 0.02$ (17)	$13.56 \pm 0.34$ (17)	$-26.43 \pm 1.07$ (13)	$25.11 \pm 2.47$ (13)
[Cr III]	16.49	$12.40 \pm 2.02$ (4)	$16.98 \pm 4.86$ (4)	$-34.54 \pm 1.56$ (3)	$20.24 \pm 1.56$ (3)	$-23.60 \pm 1.00$ (1)	$10.80 \pm 1.00$ (1)
[Ni III]	18.17	$20.28 \pm 0.15$ (2)	$15.36 \pm 0.87$ (2)	$-24.54 \pm 0.24$ (2)	$12.80 \pm 1.57$ (2)	$-19.20 \pm 1.00$ (1)	$25.70 \pm 1.00$ (1)
[S III]	23.34	$15.00 \pm 1.00$ (1)	$12.70 \pm 1.00$ (1)	$-30.60 \pm 1.00$ (1)	$15.10 \pm 1.00$ (1)	$-25.90 \pm 1.00$ (1)	$25.10 \pm 1.00$ (1)
[Cl III]	23.81	$14.20 \pm 0.30$ (4)	$12.44 \pm 0.29$ (4)	$-30.98 \pm 1.91$ (3)	$16.16 \pm 1.06$ (3)	$-27.24 \pm 0.08$ (2)	$25.81 \pm 1.08$ (2)
C II	24.38	$18.63 \pm 1.95$ (6)	$13.71 \pm 0.69$ (6)	$-26.00 \pm 2.18$ (5)	$21.61 \pm 1.82$ (5)	$-23.39 \pm 1.93$ (2)	$46.05 \pm 4.30$ (2)
He I	24.59	$15.87 \pm 0.53$ (75)	$15.81 \pm 0.33$ (75)	$-29.08 \pm 0.90$ (66)	$21.52 \pm 1.23$ (66)	$-24.42 \pm 0.60$ (42)	$26.51 \pm 0.63$ (42)
[Ar III]	27.63	$15.40 \pm 0.04$ (2)	$11.10 \pm 0.04$ (2)	$-30.40 \pm 0.04$ (2)	$16.10 \pm 0.04$ (2)	$-25.00 \pm 1.00$ (1)	$25.10 \pm 1.00$ (1)
[Fe IV]	30.65	$21.20 \pm 1.00$ (1)	$12.30 \pm 1.00$ (1)	$-23.70 \pm 1.00$ (1)	$19.40 \pm 1.00$ (1)	-	-
[Cr IV]	30.96	$18.40 \pm 1.00$ (1)	$12.10 \pm 1.00$ (1)	$-25.70 \pm 1.00$ (1)	$21.90 \pm 1.00$ (1)	$-30.20 \pm 1.00$ (1)	$39.40 \pm 1.00$ (1)
[O III]	35.12	$16.13 \pm 1.37$ (3)	$11.75 \pm 0.45$ (3)	$-29.07 \pm 1.03$ (3)	$17.60 \pm 0.01$ (3)	$-25.03 \pm 0.42$ (3)	$25.02 \pm 0.70$ (3)
O II	35.12	$15.80 \pm 0.03$ (6)	$12.64 \pm 0.44$ (6)	$-29.38 \pm 0.12$ (6)	$18.89 \pm 0.43$ (6)	$-25.23 \pm 0.68$ (6)	$31.78 \pm 3.46$ (6)
[Cl IV]	39.61	$17.80 \pm 1.00$ (1)	$10.50 \pm 1.00$ (1)	$-27.60 \pm 1.00$ (1)	$21.90 \pm 1.00$ (1)	$-20.50 \pm 1.00$ (1)	$33.10 \pm 1.00$ (1)
[Ar IV]	40.74	$15.35 \pm 1.55$ (2)	$11.69 \pm 0.69$ (2)	$-29.45 \pm 2.65$ (2)	$21.20 \pm 2.20$ (2)	$-26.83 \pm 0.07$ (2)	$27.88 \pm 2.92$ (2)
[Ne III]	40.96	$15.80 \pm 0.10$ (2)	$12.35 \pm 0.05$ (2)	$-28.95 \pm 0.05$ (2)	$16.22 \pm 0.04$ (2)	$-25.90 \pm 0.03$ (2)	$25.50 \pm 0.03$ (2)
Ne II	40.96	$14.92 \pm 0.33$ (2)	$14.44 \pm 1.49$ (2)	$-26.89 \pm 0.37$ (2)	$22.28 \pm 0.14$ (2)	-	-
N I	14.53	$29.82 \pm 0.25$ (16)	$9.47 \pm 0.20$ (16)	$-29.80 \pm 1.00$ (1)	$36.00 \pm 1.00$ (1)	$-25.40 \pm 1.00$ (1)	$29.40 \pm 1.00$ (1)
Si II	16.35	$19.25 \pm 2.45$ (10)	$19.42 \pm 1.35$ (10)	$-29.18 \pm 1.06$ (8)	$17.35 \pm 1.78$ (8)	$-26.90 \pm 1.16$ (7)	$23.89 \pm 2.25$ (7)
Si III	33.49	$12.91 \pm 1.00$ (1)	$13.23 \pm 2.79$ (1)	$-31.80 \pm 1.00$ (1)	$10.80 \pm 1.00$ (1)	-	-
Ne I	21.57	$16.66 \pm 2.38$ (6)	$15.66 \pm 0.65$ (6)	$-31.78 \pm 5.50$ (3)	$23.81 \pm 2.20$ (3)	-	-
S II	23.34	$16.50 \pm 0.69$ (5)	$16.69 \pm 4.21$ (5)	$-26.88 \pm 0.44$ (3)	$25.49 \pm 3.34$ (3)	$-34.90 \pm 1.00$ (1)	$33.10 \pm 1.00$ (1)
N II	29.60	$15.07 \pm 2.57$ (25)	$13.65 \pm 1.94$ (25)	$-29.93 \pm 1.10$ (10)	$18.33 \pm 2.29$ (10)	$-25.31 \pm 3.86$ (7)	$24.49 \pm 7.94$ (7)
S III	34.79	$16.06 \pm 0.80$ (4)	$13.83 \pm 2.61$ (4)	$-29.04 \pm 1.87$ (4)	$25.21 \pm 3.48$ (4)	$-38.86 \pm 4.34$ (3)	$15.85 \pm 4.12$ (3)
N III	47.45	$11.52 \pm 0.81$ (2)	$11.94 \pm 0.16$ (2)	$-36.50 \pm 1.00$ (1)	$22.70 \pm 1.00$ (1)	-	-

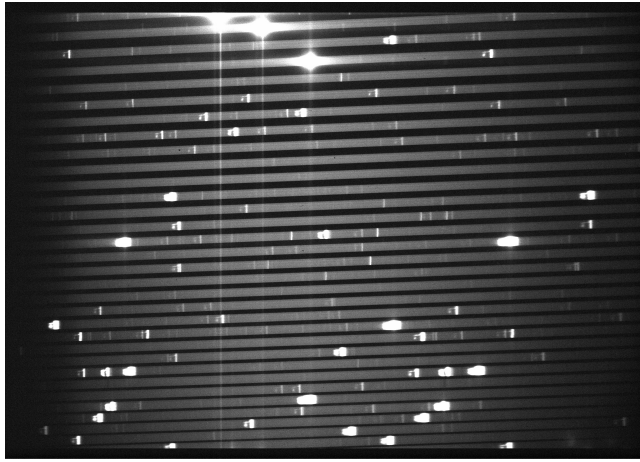


**Figure A2.** Image of part of the echelle orders extracted in the UVES blue arm using dichroic #2 setting ( $\Delta\lambda = 3750 - 4995 \text{ \AA}$ ). The contrast highlights reflections in the optical system of the spectrograph that can affect some lines. We have established that order 1 is the order at the bottom and 31 at the top.

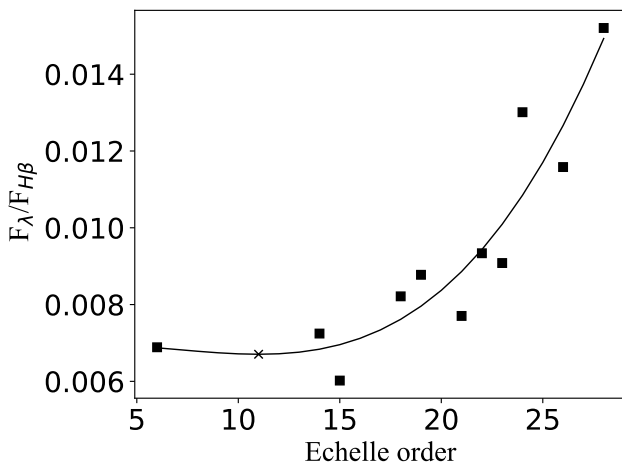


**Figure A3.** Least Squares fit of the flux emission for the third source of "ghost lines" in the echelle orders. The prediction for the ghost line at  $\lambda = 4089.07$  (in the order 11) is marked with a cross.

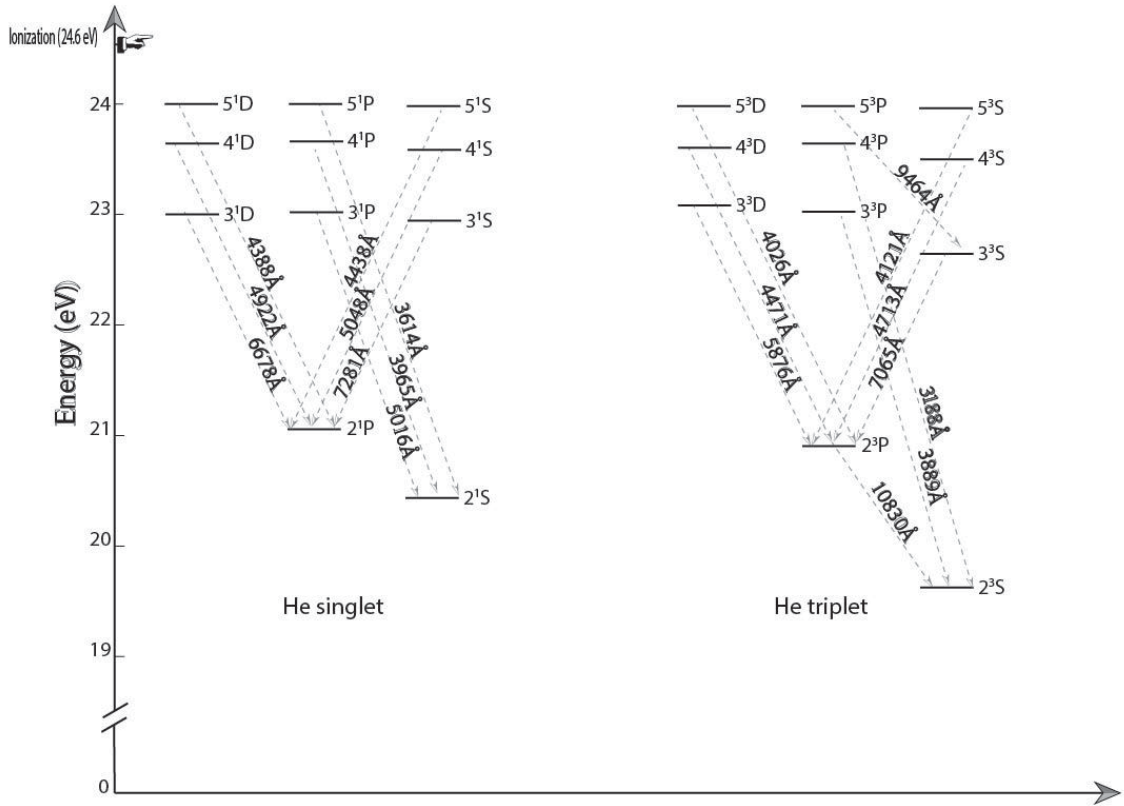
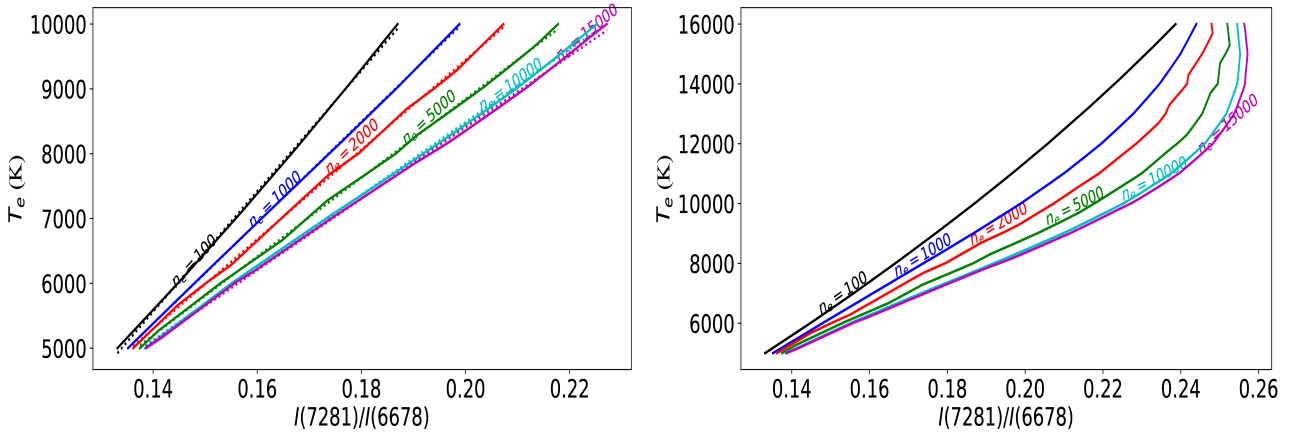


**Figure A4.** Grotrian diagram of He I for both configurations: triplet and singlet.

**Figure A5.** Dependence of  $I(\text{He I } \lambda 7281)/I(\text{He I } \lambda 6678)$  on the physical conditions.



(a) A linear fit is accurate for  $T_e \leq 10000$  K.

(b) A linear fit is not accurate for  $T_e > 10000$  K.